NTNU

Norwegian University of
Science and Technology

Design of a Light and Compact Antenna Element for Ultrawideband Digital Arrays

Gisle Hovland Stenseth

Master of Science in Electronics
Submission date: July 2018
Supervisor: Egil Eide, IES
Co-supervisor: Fredrik Gulbrandsen, Forsvarets Forskningsinstitutt

Norwegian University of Science and Technology
Department of Electronic Systems

Problem Description

Background

A digital array is a phased array antenna where each element is connected to its own analog-digital and digital-analog converter. This maximizes the utilization of the array, and allows the use of advanced beam forming techniques, multiple simultaneous main lobes and multi-function capabilities. Multi-function capabilities are here referred to as the ability to solve multiple problems at the same time e.g being used as both a radar antenna and communications antenna. A lot of research has been done in recent years on the subject of digital arrays. For instance, the Norwegian Defence Research Establishment (FFI) are developing a digital array for maritime radars. Right now there is a focus on wideband solutions. This is connected to the wish of adding more functionality to smaller platforms. In these smaller platforms multi-function capabilities is important.

Ultrawideband digital arrays is an extensive subject with many challenges and problems. Problems like: design of ultrawideband antenna elements, array architecture for ultrawideband arrays, design of the transmitter/receiver electronics and the development of beam forming algorithms. The project group for passive sensors at FFI has just started researching this subject. The goal for the future is to develop arrays with multi-function capabilities, and add them to platforms such as unmanned aerial vehicles (UAV) and satellites. Therefore, light and small antenna design solutions covering large frequency bands are desirable. Tightly coupled dipole arrays (TCDA) are one of these design solutions.

Task description

The goal of this project is to design an array based on TCDA technology covering the frequency band of 2-18 GHz. The student should use Ansys HFSS for the design, but other tools are also acceptable. If time allows, the array can be built and tested. Therefore, the antenna has to be producible. Alternative production methods such as printed circuit boards shall be considered. The student shall research existing solutions and in the end compare his/her own results against these.

- Research challenges and problems regarding ultra wideband (UWB) antenna elements and array architecture. Existing solutions shall be evaluated and compared.
- Design an ultrawideband array based on TCDAs. The goal is a frequency band of 2-18 GHz.
- Compare the design to existing solutions.
- Build and test the antenna if time allows.
- Show the need for further research and give advice on different solutions.

Abstract

This report contains the design of a tightly coupled dipole array (TCDA) ultrawideband (UWB) antenna element with an integrated Marchand balun made for digital phased arrays. The element is manufactured and measured as part of an 8x8 array. The project is done in cooperation with the research group for passive RF-sensors at the Norwegian Defence Research Establishment (FFI) who are in the beginning phases of researching UWB technology.

In an infinite array simulation, the element performs on par with existing designs made for the same frequency bands. At broadside it achieves a bandwidth of 1:5.35 (2.33-12.46 GHz) for a voltage standing wave ratio (VSWR) of < 2.5 and a radiation efficiency of $> 80\%$. The bandwidth for the same conditions at a scan angle of 70° in the E-plane is 1:4.26 (2.7-11.5) GHz. In the H-plane, the VSWR is slightly higher, and the array achieves a bandwidth of 2.35-12.2 GHz (1:5.2) for a VSWR of < 3 and a radiation efficiency of $> 80\%$ at a scan angle of 50°. The radiation efficiency at broadside is $> 90\%$ for a bandwidth of 2.3-11.8 GHz (1:5.13) which could be important if the antenna is to be used in radio detection and ranging (radar).

The manufactured prototype shows promising results, but needs more work in order to function on the same level as the simulated array. It suffers from peaks in the VSWR believed to be caused by ground loops and production inaccuracies. At broadside, the prototype achieves a bandwidth of 2.45-12.95 GHz (1:5.3) for a VSWR of < 4 (< 2.5 if the largest peak is ignored). It is likely that the VSWR can be reduced through better production.

Samandrag

Denne rapporten omhandlar designet av eit tettkopla-dipol ultrabreibands antenneelement med integrert Marchand-blaun for digitalt fasestyrte gruppeantenner. Antenneelementet er produsert og målt som del av ei 8x8 gruppeantenne. Prosjektet er gjort i samarbeid med prosjektgruppa for passive sensorar ved Forsvarets Forskningsinstitutt (FFI) som er i startfasen av si forsking på ultrabreibandsteknologi.

Simulert som ein del av ei uendeleg stor gruppeantenne, viser elementet ein ytelse på same nivå som andre tilsvarande design laga for same frekvensområde. Beint fram oppnår antenna ei bandbreidde på 1:5.35 (2.33-12.46 GHz) med eit standbølgjeforhold på < 2.5 og ein utstrålingseffektivitet på $> 80\%$. Med dei same krava til standbølgjeforhold og utstrålingseffektivitet, oppnår arrayet ei bandbreidde på 1:4.26 (2.7-11.5) GHz for ein 70° skannvinkel i E-planet. I H-planet er standbølgjeforholdet noko høgare, og antenna oppnår ei bandbreidde på 2.35-12.2 GHz (1:5.2) med eit standbølgjeforhold på < 3 og ein utstrålingseffektivitet på $> 80\%$. Beint fram held utstrålingseffektiviteten seg over 90% for ei bandbreidde på 2.3-11.8 GHz (1:5.13), noko som kan vere viktig dersom antenna skal brukast til dømes innan radar.

Den produserte prototypa viser lovande resultat, men må jobbast meir med for å få ytelsen på same nivå som den sett i simuleringane. Den har problemar med brå toppar i standbølgjeforholdet som ein trur skuldast jordsløyfer og produksjonsavvik. Beint fram oppnår prototypa ei bandbreidde på 2.45-12.95 GHz (1:5.3) med eit standbølgjeforhold på < 4 (< 2.5 dersom ein ser vekk frå den største toppen). Det er sannsynleg at standbølgjeforholdet kan reduserast ved betre produksjon av prototypa.

Acknowledgements

I would like to thank my supervisor at FFI, Fredrik Gulbrandsen, for always making time for me and giving me thorough supervision. I would also like to thank him for spending long days and evenings in the laboratory with me, handling the expensive measurement equipment. Thanks to FFI for allowing me to do this project, and to my supervisor at NTNU, Associate Professor Egil Eide for helping me with my report and giving valuable feedback.

Contents

Abbreviations

CPS	Coplanar stripline
CPW	Coplanar waveguide
FFI	The Norwegian Defence Research Establishment, Forsvarets Forskningsinstitutt
OFDM	Orthogonal frequency division multiplexing
PCB	Printed circuit board
RADAR	Radio detection and ranging
SMP	Subminiature version P
TCDA	Tightly coupled dipole array
UAV	Unmanned aerial vehicle
UiO	University of Oslo, Universitetet i Oslo
UWB	Ultrawideband

Nomenclature

β	Phase increment
δ	Used to denote Dirac delta pulses
ϵ	Permittivity of a material
ϵ_0	Permittivity of free space, $8.854187817 \cdot 10^{-12}$ F/m
ϵ_r	Relative permittivity of a material
ϵ_{eff}	Effective permittivity of a material
η_0	Intrinsic impedance of free space, 120 π
η_{sub}	Intrinsic impedance of substrate
η_{sup}	Intrinsic impedance of superstrate
Γ	Reflection coefficient
Γ_{dB}	Reflection coefficient in dB

λ	Wavelength
μ_0	Permeability of free space, $4\pi \cdot 10^{-7}$ H/m
μ_r	Relative permeability of a material
Ω	Impedance in Ohm
ϕ	Used to denote the angle of the direction of propagation relative to the x-axis in the x-y plane
θ	Used to denote the angle of the direction of propagation relative to the z-axis
ξ_r	Radiation efficiency
c_0	The velocity of light in free space
d_x	Length of a unit cell in the x-direction (antenna element spacing)
d_y	Length of a unit cell in the y-direction (antenna element spacing)
k_0	Propagation constant of free space
T_{dB}	Transmission coefficient in dB
v	Velocity
Z_0	Source impedance
Z_{in}	Input impedance
A	Area
Ansys HFSS	A 3D electromagnetic field simulator for RF and wireless design by Ansys
Boresight	θ=0
Broadside	θ=0
C	Capacitance
D	Directivity
d	Distance
dB	Decibel
f	Frequency
G	Used for both conductance and gain
k	Propagation constant
L	Inductance
R	Resistance
T	Transmission coefficient

TE	Transverse electric. Plane wave where the electric field vector is perpendicular to the propagation vector
TEM	Transverse magnetic. Plane wave where the magnetic and electric field vectors are perpendicular to the propagation vector
TM	Transverse magnetic. Plane wave where the magnetic field vector is perpendicular to the propagation vector
V	Voltage
via	Pin connecting different copper layers on a PCB
VSWR	Voltage standing wave ratio, Ratio between the maxima and minima of a standing wave on a transmission line
Z	Impedance

Chapter 1

Introduction

Ultrawideband (UWB) digital arrays offer great opportunities in both radar and telecommunications systems, as they increase both performance and flexibility. The Norwegian Defence Research Establishment (FFI) are, amongst other projects, developing a digital array radar, and are interested in looking at UWB solutions. This project is done mainly as a research project to see what can be achieved using the tightly coupled dipole array technology (TCDA), and is therefore not made for a specific application, but is made to work with both radar, telecommunications and electronic warfare applications. There is also a desire to make a physically small antenna array which can be mounted on small platforms such as unmanned aerial vehicles (UAV) or small satellites. This project is a first step towards UWB digital arrays at FFI.

1.0.1 Digital phased arrays

In a digital phased array, each element has its own radio front end, analog to digital converter and digital to analog converter as opposed to standard phased arrays where one common signal is sent to all the elements through a feed network with attenuators and phase shifters. The electronics in the digital phased array allows the phase and amplitude of the input signal in each of the elements can be controlled separately. This gives very good control of the antenna's radiation pattern.

As opposed to arrays with analog phase controllers, a digital array can use one sample of the signal received from all the elements to produce simultaneous antenna pattern lobes. It can also be used for several different applications simultaneously by splitting the array into sub-arrays performing different tasks. An example being that the array can be used both as a radar and a telecommunication antenna at the same time. Doing these things, of course requires a lot of processing power. The extra electronics of the digital phased arrays significantly increase cost, size and power consumption [1] which is the main downside to the technology.

1.0.2 Ultrawideband antennas

Doing telecommunications and radar simultaneously requires a large spacing in frequency to avoid interference. This is one of the reasons why UWB arrays are needed.

In radar, the range resolution is proportional to the bandwidth. Therefore a UWB radar can separate targets in range better than normal radars. A small enough range resolution also makes it possible to distinguish separate elements of the target. In addition to this, a UWB radar reduces the effects of passive interference like metal strips and rain, improves the stability at lower elevation angles and increases the probability of detection as a larger frequency band will limit the cancelling of waves due to destructive interference. In a military situation, UWB makes the system more robust against noise and jamming and makes it harder to detect [2]. For an antenna to work well in a radar, the efficiency should be high due to the high output power in radar systems. Most of the power not radiated from the antenna due to low efficiency is transformed into heat. Low efficiency and high power could break the antenna.

In telecommunications, wideband technology can be used to spread the energy over a wide frequency band during communication, making it harder to detect. Modulation types like orthogonal frequency division multiplexing (OFDM) use frequency diversity (spreading the signal over several different carriers) to avoid loss of data due to frequency selective fading. A wideband digital array can be used to transmit on several different channels simultaneously, eliminating the need for several separate antennas.

The type of antenna array requested by FFI, TCDA, has been known to reach very large bandwidths. TCDAs use the capacitance created between tightly spaced elements to counter the inductive effects of a nearby ground plane. The first TCDA was realized by Ben Munk who placed Wheeler's current sheet [3] over a ground plane, and put finger capacitors at the ends of the dipoles to increase the capacitive coupling between elements [4]. The past ∼10 years, a lot of the research in this subject has been done at The Ohio State University under the supervision of Prof. John L. Volakis.

Fig. 1.1 shows the concept of the TCDA, while Fig. 1.2 shows a common implementation where the arms of the dipoles overlap. The dipoles are not in contact with each other, but are separated by a dielectric material, creating a parallel plate capacitor.

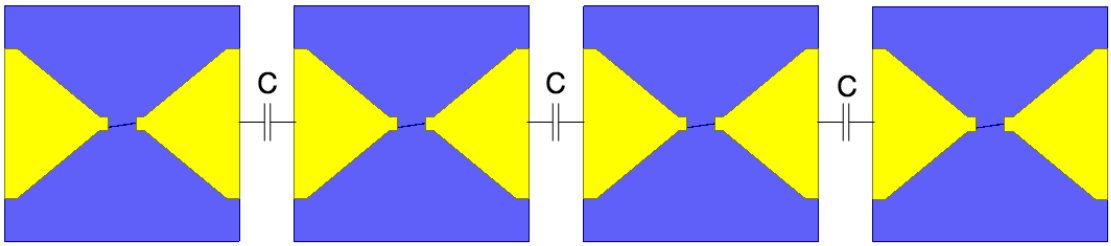

Figure 1.1: TCDA concept shown in a 1x4 array configuration

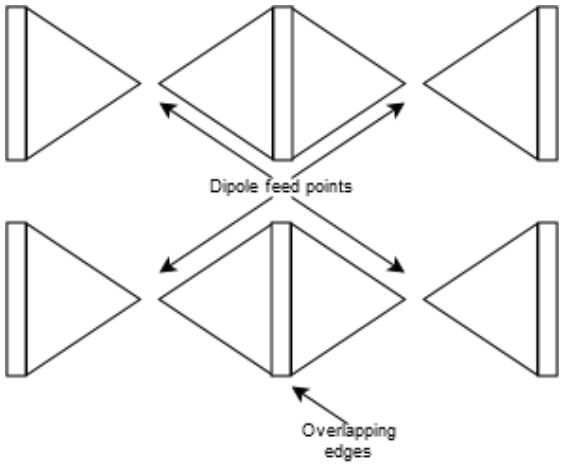

Figure 1.2: A common implementation of TCDA using overlapping edges

Depending on the desired scan capabilities and efficiency, TCDAs with integrated feed systems have shown bandwidth ratios up to 1:13.5 [5] for a VSWR of < 2.5 (1:13.5 is the ratio between the highest and lowest frequency in the bandwidth). In addition to reaching great bandwidths, they have good scanning capabilities with some designs reaching scan angles of $\pm 70°$ for a voltage standing wave ratio (VSWR) of < 3.2 [6]. They can also conform to different shapes like aircraft hulls [7]. There are not a lot of TCDAs made for the frequency band specified for this project (2-18 GHz). The most notable is Novak's TCDA with integrated balun, which covers a frequency band of 3-18.5 GHz for a VSWR of < 2 [8]. Designing arrays for higher frequencies introduces challenges in terms of the physical space available for feed systems.

There is a constant trade-off between VSWR, efficiency, bandwidth and scan performance when designing TCDAs. As an example, Papantonis' array in [5] uses increased resistive loss to achieve a very large bandwidth, limiting both efficiency and scan performance. Yetisir [6] allows a higher VSWR in his array to achieve larger scan angles while Novak achieves a limited bandwidth and scan performance with a lower VSWR.

1.0.3 Requirements from FFI

The only specification in the problem description was that the goal bandwidth for the array should be 2-18 GHz. Some minimum requirements to justify production along with some additional goals were stated later. These are summarized in Table 1.1

Table 1.1: Array Specifications

Parameter	Goal	Requirement
Frequency band	2-18 GHz	3-12 GHz
Bandwidth ratio	1:9	1:4
Scan area	-60 ° to 60 °	-40 ° to 40 °
VSWR	< 2	< 3
Radiation efficiency	>95%	>70%
Polarization		Single, linear
Mechanical requirements		Realizable, movable

The reason for the requirements stated in the problem description being somewhat slack, is that this is a research project looking into what is possible to achieve using TCDA technology and the challenges surrounding the feed systems and production limitations at these frequencies.

1.0.4 Prework

During the fall of 2017, a specialization project was done in preparation for this project. Here, a TCDA antenna element without a feed system was designed. The element used overlapping edges at the ends of the dipoles as seen in Fig. 1.2. What is meant by the element not having a feed system is that the dipoles were fed directly by a point source of 150 Ω at the dipole feed points (see Fig. 1.2). Whereas it is desirable that the dipoles are terminated in a connector with the commonly used impedance of 50 Ω. It is also desirable to have the connectors on the back side of the ground plane to avoid interfering with the dipole. This is where the main design challenge in this project lies: Implementing a feed system which is both small enough to fit in the antenna element, and wideband enough to match the dipoles.

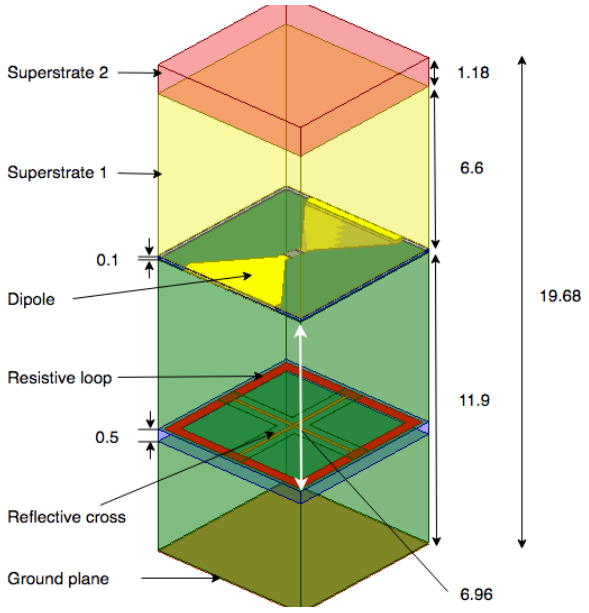

Figure 1.3: Antenna element from the previous project. All dimensions in mm

The antenna element from the previous project, seen in Fig. 1.3, utilized a resistive frequency selective surface (FSS) to reach an impedance bandwidth of 1.64-16.78 GHz (1:10.2) for a VSWR of <2 and a radiation efficiency of >70%. The results and dimensions of the design are discussed further in section 3.1. Extensive changes had to be made to this design in order to make it producible with an integrated feed system. The dipole from this project, however is used to explain some of the phenomena discussed in the background theory chapter.

1.0.5 Report outline

The rest of the report is set up as follows: First some background theory covering most of the phenomena regarding array and feed system design used in later parts is presented. The next chapter starts at the design from the previous report seen in Fig. 1.3 and covers all the design decisions and changes necessary to make it a working design terminated in 50 Ω connectors. This chapter also contains the simulation results for the infinite design, the simulation setup for an 8x8 array and ends in a section describing the finished physical prototype. Before the results and discussion chapter, the measurement setups and methods are described. In the results and discussion chapter, the results from the measurements are discussed, before the design is compared to other existing designs.

Chapter 2

Theoretical background

2.1 Basic relations

The following section contains some general relations used in the text regarding the propagation of electromagnetic waves in dielectric materials.

When two electric conductors are placed close to each other, they form a parallel plate capacitor. This is what happens between the arms of the dipoles in TCDAs. The capacitance of such a parallel plate capacitor can be calculated as [9]

$$C = \epsilon \frac{A}{d}, \tag{2.1}$$

where A is the area of the overlapping between the plates, ϵ is the permittivity of the dielectric material and d is the distance between the plates. The permittivity ϵ is a result of the factorization of the permittivity of free space $\epsilon_0 = 8.854187817 \cdot 10^{-12}$ F/m and the permittivity of the material relative to the permittivity of free space ϵ_r:

$$\epsilon = \epsilon_r \epsilon_0 \tag{2.2}$$

The permittivity of a material changes the properties of the wave travelling along or inside it. Often it is interesting to know the effective permittivity on the border between two materials with different permittivities. The effective relative permittivity at the border of two equally sized non-magnetic (relative permeability $\mu_r = 1$) dielectric materials with different permittivities as seen Fig. 2.1,

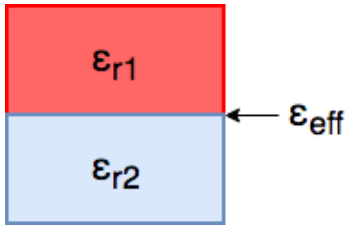

Figure 2.1: Border between two dielectric materials

can be found by using the relations from [10] as

$$\epsilon_{eff} = \frac{\epsilon_{r1} + \epsilon_{r2}}{2}, \tag{2.3}$$

where ϵ_{r1} and ϵ_{r2} are the relative permittivities of the materials. For propagation on substrates bordering to air (e.g. along the surface of a printed circuit board (PCB), one of the permittivities is equal to one. The electrical length of a wave travelling in such a medium is dependent on the propagation velocity v, which can be found from the formula

$$v = \frac{c_0}{\sqrt{\epsilon_{eff}}} \tag{2.4}$$

where c_0 is the velocity of light in free space. The wavelength λ of a wave propagating in a medium is calculated as

$$\lambda = \frac{v}{f} \tag{2.5}$$

where f is the frequency of the wave. Using this length, the propagation constant k of the wave can be found [9]

$$k = \frac{2\pi}{\lambda} \tag{2.6}$$

The intrinsic impedance, or the impedance a wave sees in a dielectric material can be expressed as

$$\eta = \sqrt{\frac{\mu_r \mu_0}{\epsilon_r \epsilon_0}} \tag{2.7}$$

where $\mu_0 = 4\pi \cdot 10^{-7}$ H/m is the permeability of free space. The intrinsic impedance of free space is found by setting $\mu_r = \epsilon_r = 1$ as

$$\eta_0 = \sqrt{\frac{\mu_0}{\epsilon_0}} = 120\pi. \tag{2.8}$$

2.2 Transmission lines

As frequency increases, and the wavelength approaches the length of physical guiding structures (wires, copper tracks etc.) and components in a circuit, normal circuit theory can no longer be used to describe circuits as the current flowing through or along them varies with length. As an example, a 10 GHz signal travelling along a 30 mm line would have one maximum, one minimum and three zeros in its current distribution along the line, while a 100 Hz signal travelling on the same line would have an almost stationary current distribution. Therefore, transmission line theory is needed. In transmission line theory, a two-wire line is used as a model to the find basic transmission equations. This can be seen in Fig. 2.2. The physical properties of this line are represented as lumped components dependent on the length of the line in the z-direction.

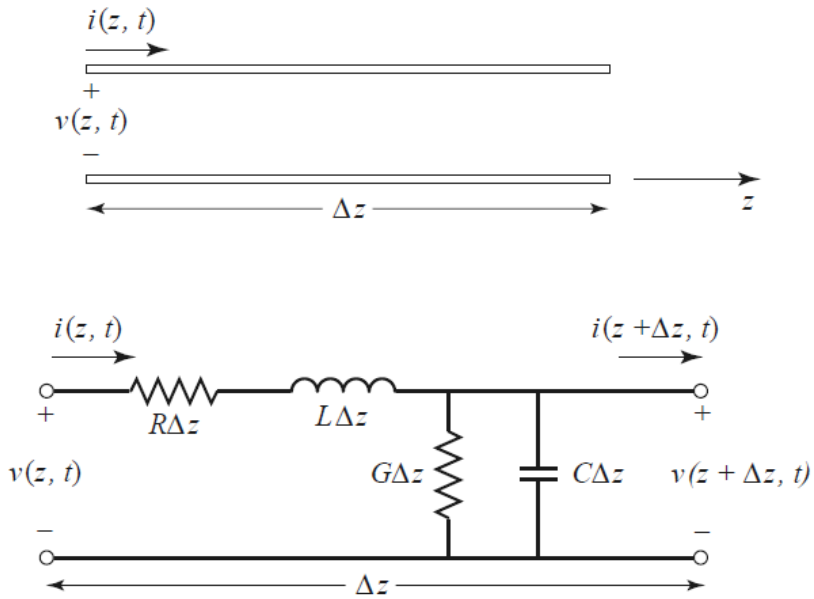

Figure 2.2: Two-line transmission line represented as lumped components [11]

In Fig. 2.2, R represents resistive loss due to imperfect conductors, L is the self inductance, C is the capacitance created by the wires being in close proximity of each other (see Eq. 2.1) and G is the conductance in the dielectric material which creates dielectric loss. Dividing the forward voltage by the forward current for the line as the length Δz approaches 0 gives [11]

$$\frac{V^+}{I^+} = Z_0 = \sqrt{\frac{R + j2\pi fL}{G + j2\pi fC}} \tag{2.9}$$

which is known as the characteristic impedance of the transmission line. If the line is made lossless, i.e. R=G=0, the characteristic impedance is [11]

$$Z_0 = \sqrt{\frac{L}{C}}. \tag{2.10}$$

If a source of impedance Z_0 is terminated in a load Z_{in} as seen in fig 2.3,

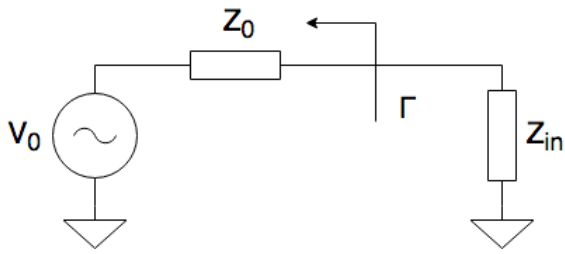

Figure 2.3: Reflection between source and load

and Z_0 and Z_{in} differ, part of the wave will be reflected back to the source. The voltage ratio between the reflected and incident waves is called the voltage reflection coefficient and can be calculated as [12]

$$\Gamma = \frac{Z_{in} - Z_0}{Z_{in} + Z_0}. \tag{2.11}$$

This value squared is the power reflection coefficient, and tells us how much of the input power is reflected back to the source. In addition to the reflected power being "lost", a high reflection coefficient could lead to the electronics driving the load being destroyed. The power reflection coefficient in dB is given by [12]

$$\Gamma_{dB} = 20log_{10}|\Gamma|. \tag{2.12}$$

The reflection coefficient can also be used to calculate the power transmission coefficient [12]

$$|T|^2 = 1 - |\Gamma|^2. \tag{2.13}$$

This is the amount of power transferred to the load from the source. In dB this is [12]

$$T_{dB} = 10log|T|^2. \tag{2.14}$$

In this text, the reflection is often referred to in terms of the voltage standing wave ratio or the standing wave ratio. This is the ratio between the maximum and minimum voltage of a standing wave on the line. The VSWR can be found using the reflection coefficient [9]:

$$VSWR = \frac{1 + |\Gamma|}{1 - |\Gamma|}. \tag{2.15}$$

2.2.1 Mictrostrip lines

One of the most used transmission line types is the microstrip line. This line consists of a copper strip of width w suspended over a ground plane on a layer of dielectric material of thickness h as seen in Fig. 2.4.

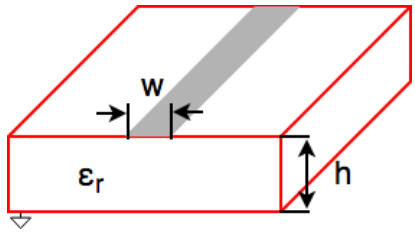

Figure 2.4: Microstrip transmission line geometry

The characteristic impedance of a microstrip can be calculated from [11]

$$Z_0 = \frac{60}{\sqrt{\epsilon_{eff}^m}} ln\left(\frac{8h}{w} + \frac{w}{4h}\right), \quad w/h \leq 1 \tag{2.16a}$$

$$Z_0 = \frac{120\pi}{\sqrt{\epsilon_{eff}^m}(w/h + 1.393 + 0.667\ ln(w/h + 1.444)}, \quad w/h \geq 1 \tag{2.16b}$$

where ϵ_{eff}^m is the effective permittivity of the line, and can be approximated as [11]

$$\epsilon_{eff}^m = \frac{\epsilon_r + 1}{2} + \frac{\epsilon_r - 1}{2} \frac{1}{\sqrt{1 + 12h/w}} \tag{2.17}$$

2.2.2 Striplines

The stripline is similar to the microstrip line, but here the line is placed in a dielectric material of thickness h between two ground planes as seen in Fig. 2.5

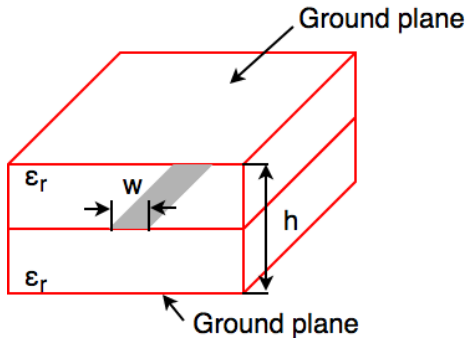

Figure 2.5: Stripline geometry

The characteristic impedance of the line can be approximated as [11]

$$Z_0 = \frac{30\pi}{\sqrt{\epsilon_r}} \frac{h}{w_e + 0.441h}. \tag{2.18}$$

Here, w_e is the effective width of the strip given by

$$\frac{w_e}{h} = \frac{w}{h} - (0.35 - w/h)^2, \quad \frac{w}{h} < 0.35 \tag{2.19a}$$

$$\frac{w_e}{h} = \frac{w}{h}, \quad \frac{w}{h} > 0.35 \tag{2.19b}$$

2.2.3 Coplanar waveguides and coplanar striplines

The geometries of coplanar waveguides (CPW) and coplanar striplines (CPS) can be seen in Fig. 2.6.

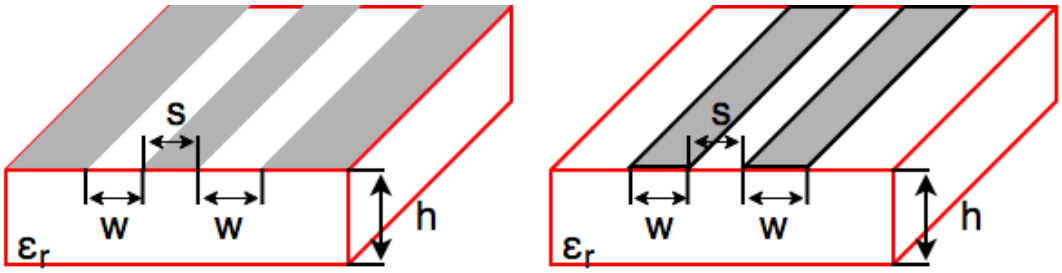

(a) (b)

Figure 2.6: Geometry of coplanar waveguide (a) and coplanar stripline (b)

CPWs and CPSs are complementary structures, meaning that when they are combined, they form a solid conductor surface without overlapping. By assuming the effective permittivities of the CPW and CPS (ϵ_{eff}^{CPW} and ϵ_{eff}^{CPS})are the same [13], the product of the characteristic impedances of the two lines is approximately a constant given by [14]

$$Z_0^{CPS} Z_0^{CPW} = \frac{\eta_0^2}{4\epsilon_{eff}^{CPS}} = \frac{\eta_0^2}{4\epsilon_{eff}^{CPW}}. \tag{2.20}$$

The effective permittivity of a coplanar waveguide can be found as [14]

$$\epsilon_{eff}^{CPW} = 1 + \frac{\epsilon_r - 1}{2} \frac{K(k_1)}{K(k_1')} \frac{K(k_0')}{K(k_0)}, \tag{2.21}$$

where K is the complete elliptical integral of the first kind and

$$k_1 = \frac{sinh(\pi s/4h)}{sinh\{[\pi(s+2w)]/4h\}}, \tag{2.22}$$

$$k_1' = \sqrt{1 - k_1^2}, \tag{2.23}$$

$$k_0 = \frac{s}{s + 2w}, \tag{2.24}$$

$$k_0^{'} = \sqrt{1 - k_0^2}. \tag{2.25}$$

2.2.4 Comparison of characteristic impedances in different line types

In this project, being able to create a large variety of impedances on relatively thin dielectric substrates is important. Therefore, a few examples of characteristic impedances for the different lines will be calculated. For these examples, the substrate is a dielectric material with $\epsilon_r = 3.66$ and thickness $h = 0.5$ mm.

Using the formulae from sections 2.2.1 and 2.2.2 for microstrip and striplines, one gets the impedance in Fig. 2.7.

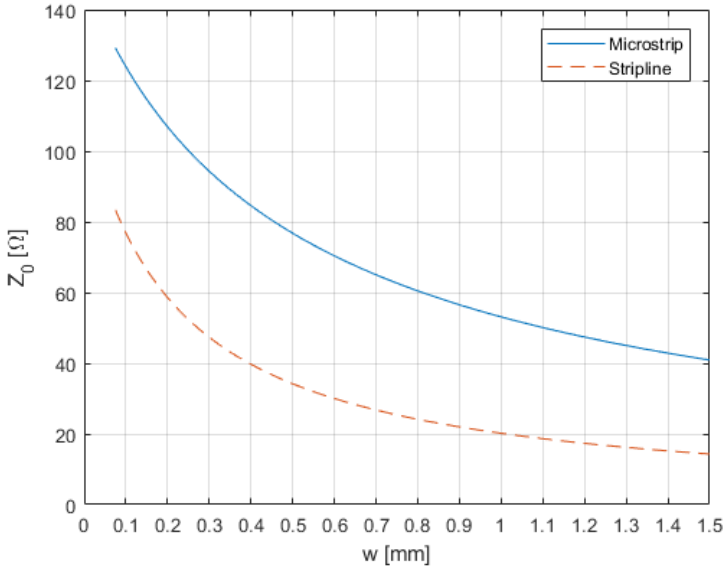

Figure 2.7: Characteristic impedance of microstrip and striplines versus line width w

From Fig. 2.7 one can see that the stripline has a significantly lower characteristic impedance than the microstrip line for any given width. This is expected as transmission lines follow Eq. 2.10, and the stripline will have a higher capacitance compared to the microstrip line. The capacitance follows Eq. 2.1. As the stripline is closer to the ground planes than the microstrip line, the capacitance will be larger, making the characteristic impedance lower (following from the basic transmission theory seen at the start of this section).

Using the formulae in section 2.2.3 for coplanar waveguides and coplanar striplines with a constant $w = 0.2$ mm and variable s, one gets

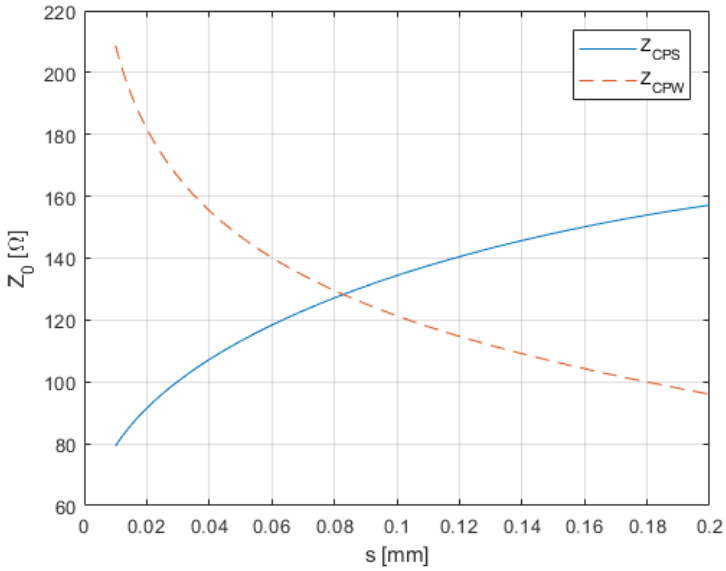

Figure 2.8: Characteristic impedance of coplanar waveguide and coplanar stripline with variable dimansion s.

From Fig. 2.8 it can be seen that with these lines, one has the possibility of creating large characteristic impedances in small spaces. However, realizing coplanar waveguides with the same impedance as coplanar striplines on the same substrate can be a challenge. At the crossing point of the two lines, $s = 0.08$ mm which is on the border of what can possibly be produced on a PCB.

2.3 Antenna arrays

Arranging antenna elements in arrays is a way of increasing the number of design possibilities of the antenna. When arranged in an array, the antenna parameters are no longer only dependent on the antenna element's geometry, but on the overall configuration of the array, distance between the elements, the amplitude and phase of the signal fed to each element in addition to the geometry of the single elements [15]. Arranging elements in arrays makes it possible to steer the main lobe of the antenna pattern, and it increases the overall gain of the antenna.

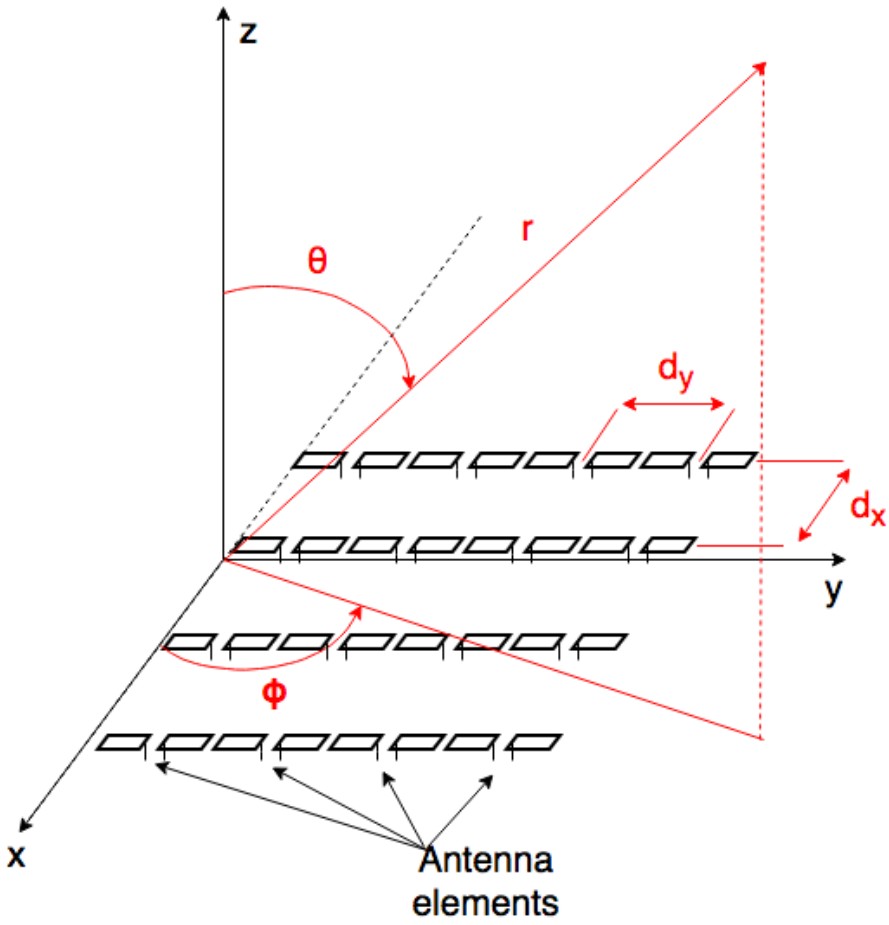

Figure 2.9: Antenna array geometry

Fig. 2.9 shows the geometry of a rectangular antenna array of dipoles where r shows the direction of radiation. The total radiated field of the array is a sum of the fields of all the elements in the array:

$$E_t = E_1 + E_2 + ... + E_m. \tag{2.26}$$

If all the elements in the array are identical, this can be reduced to a factorization of the field of a single element and the array factor:

$$E_t = E_{element} AF, \tag{2.27}$$

where the array factor is a sum of the phase fed to each element and the element's coordinates effect on the field. For a one dimensional array of size M (one column of elements in Fig. 2.9) with isotropic sources, the array factor is [15]

$$AF = 1 + e^{j(kd_x cos\theta + \beta_x)} + e^{j2(kd_x cos\theta + \beta_x)} + ... + e^{j(M-1)(kd_x cos\theta + \beta_x)} \tag{2.28}$$

which can be written as

$$AF = \sum_{m=1}^{M} e^{j(m-1)\Psi} \tag{2.29}$$

where

$$\Psi = kd_x cos\theta + \beta_x. \tag{2.30}$$

Here, k is the propagation constant, d_x the spacing between elements and β_x is the increment in the phase fed to each element in the array. Setting $\Psi = 0$ we see that changing the phase increment β_x alters the scan angle θ. Arrays where β_x is steered electronically are called phased arrays. When the scan angle θ is zero, and the direction of propagation is strictly in the z-direction, this is referred to as boresight or broadside.

Expanding the array to two dimensions as seen in Fig. 2.9, the array factor for the same column of elements becomes [15]

$$AF_x = \sum_{m=1}^{M} I_{xm} e^{j(m-1)\Psi_x}. \tag{2.31}$$

For the rows along the y-axis, one gets

$$AF_y = \sum_{n=1}^{N} I_{yn} e^{j(n-1)\Psi_y} \tag{2.32}$$

where I_{xm} and I_{yn} are the amplitudes of the currents fed to the elements and

$$\Psi_x = kd_x sin\theta cos\phi + \beta_x \tag{2.33}$$

and

$$\Psi_y = kd_y sin\theta sin\phi + \beta_y. \tag{2.34}$$

The total array factor is simply a multiplication of these two factors

$$AF = AF_x AF_y. \tag{2.35}$$

As with the one dimensional case, the scan angle (θ, ϕ) is altered by changing the input phase of the elements (β_x, β_y).

The directivity of the array along the two axes can be approximated as [15]

$$D_x \approx 2M\left(\frac{d_x}{\lambda}\right), D_y \approx 2N\left(\frac{d_y}{\lambda}\right). \tag{2.36}$$

Using this one can make a rough estimate for the directivity of the total array from [15].

$$D_a = \pi cos\theta D_x D_y. \tag{2.37}$$

The cosθ factor is added to account for the loss in illumination of the array due to the scan angle [15]. D_a is the directivity based on the array factor only. To have the directivity of the full array, it must be multiplied by the directivity of a single element:

$$D = D_a D_e \tag{2.38}$$

where D_e is the gain of a single element. For $\theta = 0$ this reduces to

$$D = \frac{4\pi A}{\lambda^2} \tag{2.39}$$

where A is the physical area of the array. Later in the report, this is referred to as the aperture limit. In order to find the gain of the array, the directivity is multiplied by the antenna's radiation efficiency as [15]

$$G = \xi_r D. \tag{2.40}$$

The radiation efficiency is a measure of how well the antenna radiates the power it is excited by and can be calculated as [15]

$$\xi_r = \frac{P_r}{P_a}, \tag{2.41}$$

where P_r is the radiated power, and P_a is the accepted power, or the power which is not reflected back to the source. In some cases it might be interesting to look at an alternative gain definition known as absolute gain or realized gain. This includes the mismatch losses and is calculated as

$$G_{tot} = \xi_r D(1 - |\Gamma|^2) \tag{2.42}$$

2.3.1 Infinite arrays and Fourier series

A way to simplify the analysis of an antenna array is to ignore the edge effects and view the array as infinitely large. Ignoring the edge effects is justified by the center elements in electrically large arrays showing approximately the same characteristics as elements in an infinite array [16] and a large reduction in simulation time. Since an infinitely large array can be seen as an infinite series of periodic sources, the current distribution can be expressed as a Fourier series. First, let us consider a one dimensional array scanning broadside where the surface current excitation can be seen as an infinite periodic function $i(x)$ in which the magnitude has periodicity d (the distance between antenna elements)[16]:

$$i(x) = \sum_{n=-\infty}^{\infty} f(x - nd) \tag{2.43}$$

The function f represents the current distribution of each antenna element, and can be seen as the distance between the elements. The Fourier transform of $i(x)$ is [16]

$$I(k_x) = \frac{1}{2\pi} \int_{-\infty}^{\infty} i(x) e^{jk_x x} dx, \tag{2.44}$$

where k_x is the spectral frequency. By inserting $i(x)$ from (2.43) into (2.44), one gets [16]

$$I(k_x) = \frac{1}{2\pi} \sum_{n=-\infty}^{\infty} \int_{-\infty}^{\infty} f(x - nd) e^{jk_x x} dx. \tag{2.45}$$

By applying the shift theorem [17] to (2.45), the transform is simplified to [16]

$$I(k_x) = F(k_x) \sum_{n=-\infty}^{\infty} e^{jnk_x d}, \tag{2.46}$$

where $F(k_x)$ is the Fourier transform of $f(x)$. The infinite series of exponential functions in (2.46) can be written as an infinite series of Dirac delta distributions, or a Dirac comb by applying Poisson's summation formula [16].

$$\sum_{n=-\infty}^{\infty} e^{jnk_x d} = \frac{2\pi}{a} \sum_{n=-\infty}^{\infty} \delta\left(k_x - \frac{2n\pi}{d}\right). \tag{2.47}$$

Inserting (2.47) into (2.46) one gets [16]

$$I(k_x) = \frac{2\pi}{d} F(k_x) \sum_{n=-\infty}^{\infty} \delta\left(k_x - \frac{2n\pi}{d}\right). \tag{2.48}$$

Taking the inverse Fourier transform yields [16]

$$i(x) = \frac{2\pi}{d} \sum_{n=-\infty}^{\infty} F\left(\frac{2n\pi}{d}\right) e^{-\frac{j2n\pi x}{d}} \tag{2.49}$$

This representation of the current distribution helps finding a solution to the vector potential when finding the radiated fields of the array.

2.3.2 Floquet series

The Fourier series representation seen in the previous section works well for an array scanning broadside (magnitude and phase have the same periodicity). In a scanning array, however, the phase and magnitude of the current distribution can have different periodicities and we need a more general representation. One possibility is to use Floquet series. The current distribution of a scanning array can be expressed [16]

$$i(x) = \sum_{n=-\infty}^{\infty} f(x - nd) e^{-jn\beta}. \tag{2.50}$$

Here, β is added as a constant phase increment similar to what would be seen in a scanning array. The magnitude still has periodicity a. The Floquet series expansion is done by following the same procedure as with the Fourier series. Using the same procedure as in the previous section, we obtain [16]

$$i(x) = \frac{2\pi}{d} \sum_{-\infty}^{\infty} F\left(\frac{2n\pi + \beta}{d}\right) e^{\frac{-j(2n\pi+\beta)x}{d}} \tag{2.51}$$

This is the Floquet series expansion of the current distribution, and is used to obtain the electromagnetic fields radiated by the array in the next section. The difference between this series and the Fourier series in the previous section is the added phase term β. If the phase term is set to 0, one obtains the Fourier series.

2.3.3 Floquet modes and field calculations

The current distribution found in Eq. 2.51 gives rise to modal field solutions. I.e. the field equations have discrete solutions to the wave equation.

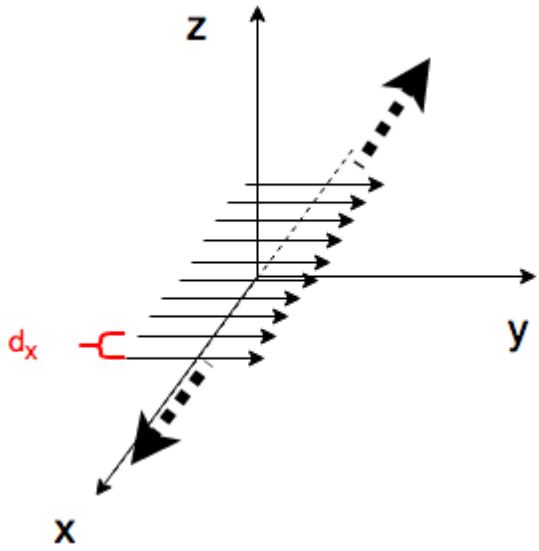

Figure 2.10: infinite array of current sources

In the one dimensional case seen in Fig. 2.10, which is an infinite linear array with element spacing d_x, a transverse magnetic field will be produced. With only one component ($E_z = E_x = 0$). This field can be expressed [16]

$$E_y(x,y,z,t) = -\frac{\pi\omega\mu_0}{d_x}\sum_{n=-\infty}^{\infty}\frac{F(k_{xn})}{k_{zn}}e^{j\omega t - jk_{xn}x - jk_{zn}z}, z > 0 \tag{2.52}$$

for an array where the space in the region $z > 0$ is free space. The exponential term inside the summation sign expresses the different Floquet modes, and the propagation direction of the n'th transverse magnetic (TM) Floquet mode can be found as

$$\theta_n = arctan\frac{k_{xn}}{k_{zn}}. \tag{2.53}$$

Where

$$k_{xn} = \frac{2\pi n + \beta}{d_x} \tag{2.54a}$$

$$k_{zn}^2 = k_0^2 - k_{xn}^2 \tag{2.54b}$$

$$k_0 = \omega\sqrt{\mu_0\epsilon_0} \tag{2.54c}$$

The phase increment, β, needed to achieve a certain scan angle can be found from [16]

$$\beta = k_0 d_x sin\theta. \tag{2.55}$$

For an infinite two dimensional array, the TM field can be expressed as [16]

$$E_x = \frac{2\pi^2}{d_x d_y \omega \epsilon_0} \sum_m \sum_n \frac{k_{xmn} k_{ymn}}{k_{zmn}} F(k_{xmn}, k_{ymn}) e^{j(-k_{xmn}x - k_{ymn}y - k_{zmn}z)} \tag{2.56a}$$

$$E_y = \frac{2\pi^2}{d_x d_y \omega \epsilon_0} \sum_m \sum_n \frac{k_0^2 - k_{ymn}^2}{k_{zmn}} F(k_{xmn}, k_{ymn}) e^{j(-k_{xmn}x - k_{ymn}y - k_{zmn}z)} \tag{2.56b}$$

$$E_z = \frac{2\pi^2}{d_x d_y \omega \epsilon_0} \sum_m \sum_n k_{ymn} F(k_{xmn}, k_{ymn}) e^{j(-k_{xmn}x - k_{ymn}y - k_{zmn}z)}. \tag{2.56c}$$

where the propagation constants for the (m, n) modes are [18][16]

$$k_{xmn} = k_0 sin\theta_{mn} cos\phi_{mn} = k_{x0} + \frac{2m\pi}{d_x} \tag{2.57a}$$

$$k_{ymn} = k_0 sin\theta_{mn} sin\phi_{mn} = k_{y0} + \frac{2n\pi}{d_y} \tag{2.57b}$$

$$k_{zmn} = k_0 cos\theta_{mn} = \sqrt{k_0^2 - k_{xmn}^2 - k_{ymn}^2} \tag{2.57c}$$

and k_{x0} and k_{y0} are the propagation constants for the dominant mode $(m, n) = (0, 0)$. This represents the main lobe. The relations in Eq. 2.57 are only valid for a rectangular grid, such as the one seen in Fig. 2.9. As can be seen from Eq. 2.52 and Eq. 2.56, an infinitely large array supports an infinite number of modes. However, for practical purposes, most of these modes remain evanescent modes decaying along the z-axis [16].

2.3.4 Unit cell representation

A way to simplify the understanding and design of infinite arrays is to use the unit cell model. Here, each element of the array is surrounded by a cell. For broadside radiation, the cell walls parallel to the electric field direction are perfect magnetic conductors, and the walls parallel to the magnetic field are perfect electric conductors as seen in Fig. 2.11.

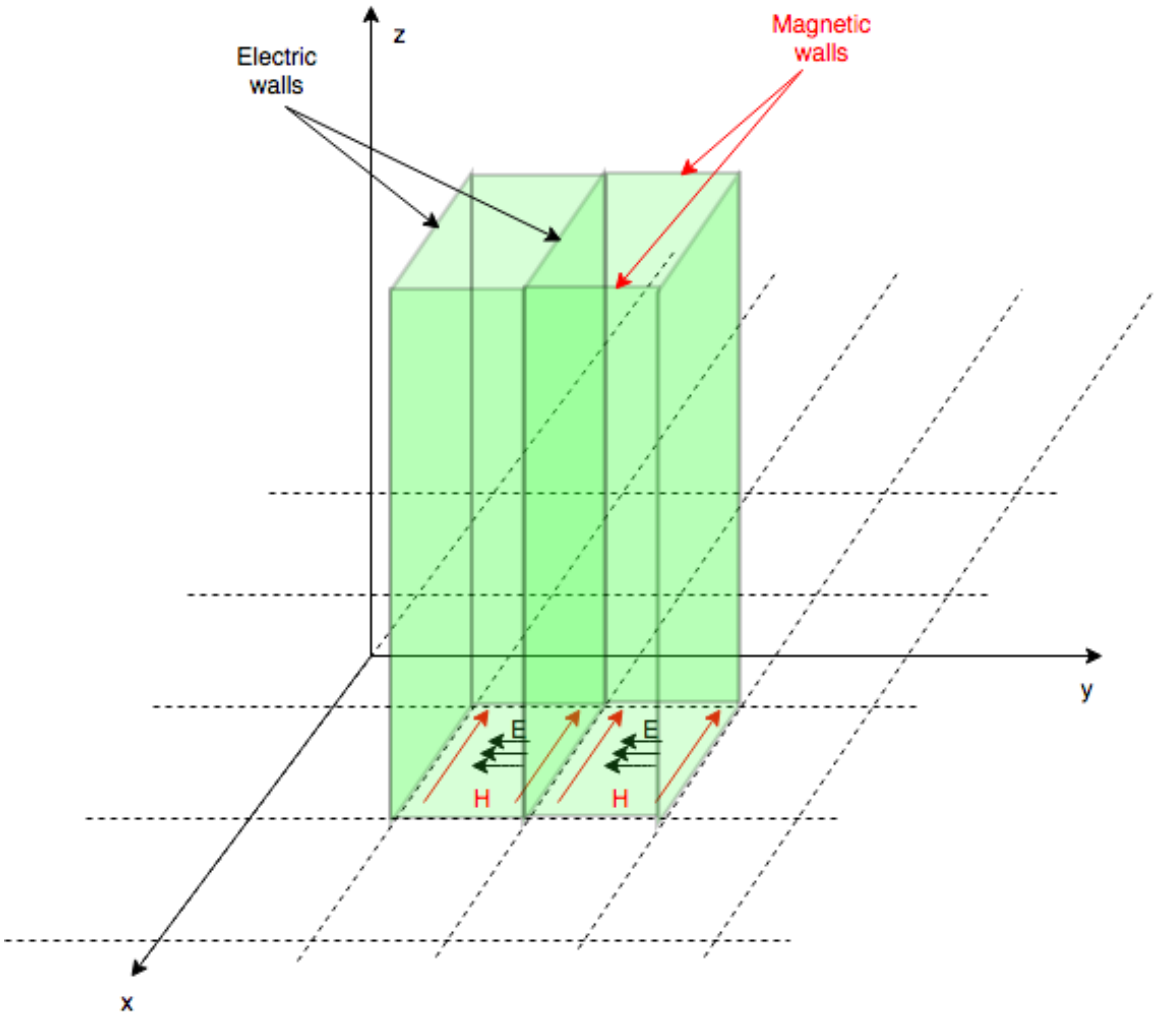

Figure 2.11: Unit cells with electric and magnetic walls

The main mode propagating in the cell is transverse electric and magnetic (TEM). When the array scans, however, this changes. As seen from Eq. (2.50) and Eq. (2.51), the cells of a scanning array differ from each other by a phase shift. In order to keep purely magnetic and electric walls, the unit cell would have to be tilted according to the scan angle, and an extra unit cell would have to be added for each propagating Floquet mode. To avoid tilting the cell and adding extra unit cells for each mode, the walls are made to support fields which differ by the Floquet phase shift β and the fields inside the cell are no longer TEM, but transverse electric (TE) and TM. Following Fig. 2.11: When scanning in the y-z plane ($\phi = 90°$), the walls laying in the y-z plane remain magnetic walls. Since the H-field is normal to the y-z plane, and this polarization is independent of the scan angle, the main mode becomes a TM mode. The E-field vector follows the scan angle. Similarly, when scanning in the x-z plane ($\phi = 0°$), the H-field follows the scan angle, and the main mode is TE . Further on in this report, the y-z plane is referred to as the E-plane and the x-z plane is referred to as the H-plane.[18][19]

Each lobe in the antenna pattern is represented by a propagating mode in the unit cell. The two main Floquet modes (TE_{00} and TM_{00}) represent the main lobe. Grating lobes appear as propagating higher order Floquet modes.

2.3.5 Scanning limitations

One of the requirements to the antenna array in this report is that it shall be able to scan to angles of at least $\pm 40°$ in both the H and E-planes. Unfortunately the scan capabilities of an array are not unlimited. There are limiting factors which will be discussed in this section.

A simple way to study the effects of scan angle on impedance, is to look at the impedance of an infinite resistive surface. By choosing the resistivity of the surface to be η_0, the reflection seen by a normally incident wave is 0. Using this model, the change in impedance due to the antenna element's radiation pattern and change in illuminated area at a certain scan angle can be expressed as [20] [15]

$$\frac{Z(\theta)}{Z_{\theta=0}} = \frac{1}{cos\theta}, \text{ (H-plane)} \tag{2.58a}$$

$$\frac{Z(\theta)}{Z_{\theta=0}} = cos\theta, \text{ (E-plane).} \tag{2.58b}$$

From this, we see that the impedance of an antenna element reaches infinity in the H-plane and zero in the E-plane for a scan angle of $\theta = 90$. This in itself causes major impedance mismatch in high scan angles.

Mutual coupling

In an array, the antenna parameters of a single element are not decided by the element itself, but is a sum of the element's characteristics, and the effects due to coupling with neighbouring elements. what is meant by coupling is the transfer of energy between the elements [15]. In general, one tries to limit the coupling between elements in an antenna array, as the effects are hard to predict analytically.

If the coupling between elements is known, the active reflection coefficient of a single element for a scan angle (θ_s, ϕ_s) can be calculated as [12][21]

$$\Gamma_0(\theta_s, \phi_s) = \sum_n S_{on} e^{-jk_0 sin(\theta_s)(x_n cos(\phi_s) + y_n sin(\phi_s))}, \tag{2.59}$$

where S_{on} is the coupling between the element in question, and the n'th array element and (x_n, y_n) are the coordinates of the element relative to the element in question in the x-y plane. This calculation is only valid if all elements in the array except the two being measured are match terminated as seen in Fig. 2.12. The measured reflection coefficient of a single element with all the other elements terminated is referred to as the passive reflection coefficient in this report.

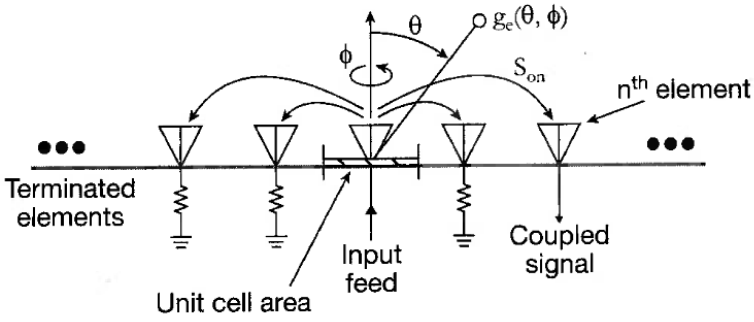

Figure 2.12: Sketch of mutual coupling in antenna arrays arrays [12]. $g(\theta, \phi)$ denotes the direction of propagation

From Eq. 2.59, it is clear that the active reflection coefficient of an antenna array is heavily dependent on scan angle, and that in standard narrowband arrays it is desirable to limit mutual coupling between the elements to reduce this dependence.

Grating lobes

Grating lobes are maxima in the antenna radiation pattern pointing in other directions than the main lobe. As mentioned in section 2.3.4, They appear when a higher order Floquet mode starts propagating. We can estimate when this starts happening using the equations 2.54. For a Floquet mode to propagate, the following condition has to be fulfilled [16]:

$$\left|\frac{k_{xn}}{k_0}\right| \leq 1 \tag{2.60}$$

equivalently, for a two dimensional array [18],

$$k_{zmn} \geq 0. \tag{2.61}$$

As an example, one can assume a one dimensional array with $d_x = 0.583\lambda$ and scan angle $\theta = 45°$. According to the formula from standard phased array theory [12]:

$$\lambda = d_x(1 + sin(\theta)), \tag{2.62}$$

the first grating lobe should appear at this scan angle. The normalized propagation constant k_{xn}/k_0 of the 7 first Floquet modes can be seen in Fig. 2.13

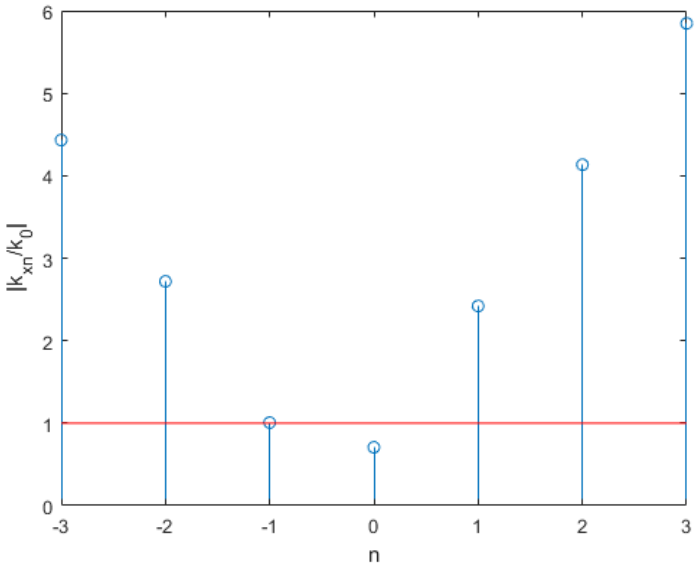

Figure 2.13: Normalized propagation constant of the 7 first Floquet modes of a one dimensional array with element spacing $d_x = 0.583\lambda$ at scan angle $\theta = 45°$

It can be seen that indeed, one of the higher order modes (n=-1) will start propagating and become a grating lobe at this scan angle. This means some of the energy fed to the array will be lost (or radiated in a different direction). As the scan angle is increased, the magnitude of the grating lobe will increase. If the distance between elements is increased, more modes can start propagating.

The experiment above shows that the simple formula seen in Eq. 2.62 works well in finding the first Floquet mode which would appear as a grating lobe.

Scan blindness due to surface waves

Surface waves can form on the borders between the array and the dielectric materials surrounding it. If one of the Floquet modes in the array has a propagation constant which coincides with the propagation constant of a surface wave, they will couple. If this happens, most of the energy delivered to the dipoles will propagate along the array's surface instead of radiating out into free space. It can also lead to the reflection coefficient becoming very large.

The condition for scan blindness in an infinite two dimensional array is [22]

$$k_{sw} = \sqrt{k_{xmn}^2 + k_{ymn}^2}. \tag{2.63}$$

Because the propagation constant of the surface wave modes (k_{sw}) is dependent on both the thickness and dielectric constant of the dielectric material surrounding the array [22][9], care must be taken to avoid coupling of the modes when adding materials.

Surface wave experiment

The array in made in the previous project was found to have a scan blindness occurring at a scan angle of ≈50 ° when scanning in the E-plane at a frequency of 18 GHz. It was believed that this blindness occurred due to coupling with a surface wave on the interface between the dielectric material placed on top of the dipoles and the dipoles themselves. To determine if this is the case, and to see the effect of changing the dielectric constant/thickness of the dielectric material, an experiment is carried out.

In this experiment, the antenna array is simulated at scan angles from 30-90° in the E-plane at 18 GHz for different thicknesses/dielectric constants of the dielectric material. As it is believed that this scan blindness happens at the interface between the material on top of the array, and the array itself, only the dipoles and dielectric material are simulated in the experiment. The propagation constants in Eq. 2.63 should be unaffected by other parts of this antenna element (i.e ground plane and FSS) according to [16]. The setup can be seen in Fig. 2.14a and the dimensions of the dipole in Fig. 2.14b.

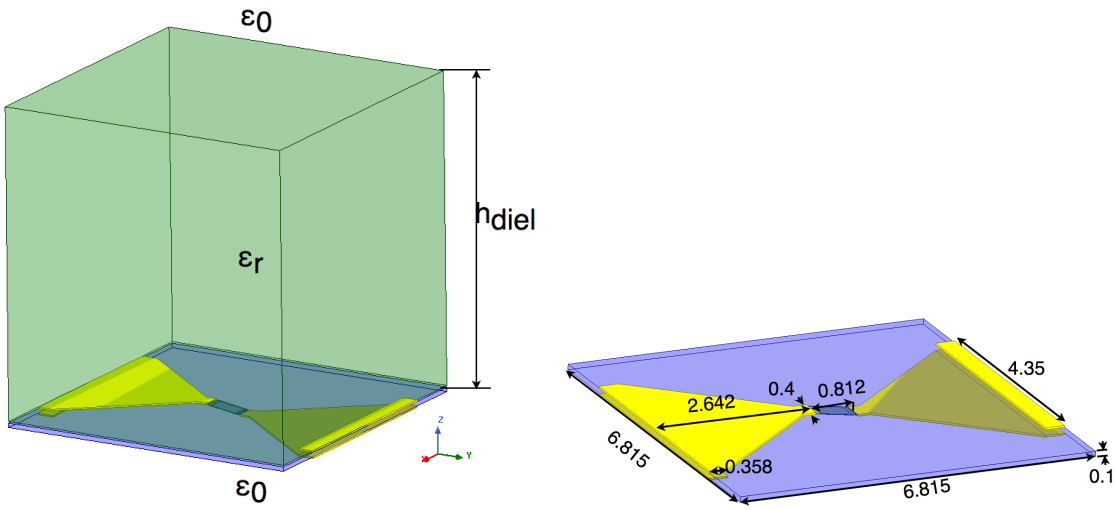

(a) (b)

Figure 2.14: Geometry of the experiment (a) and the dimensions of the dipole in mm (b)

The results of the simulations can be seen in Fig. 2.15.

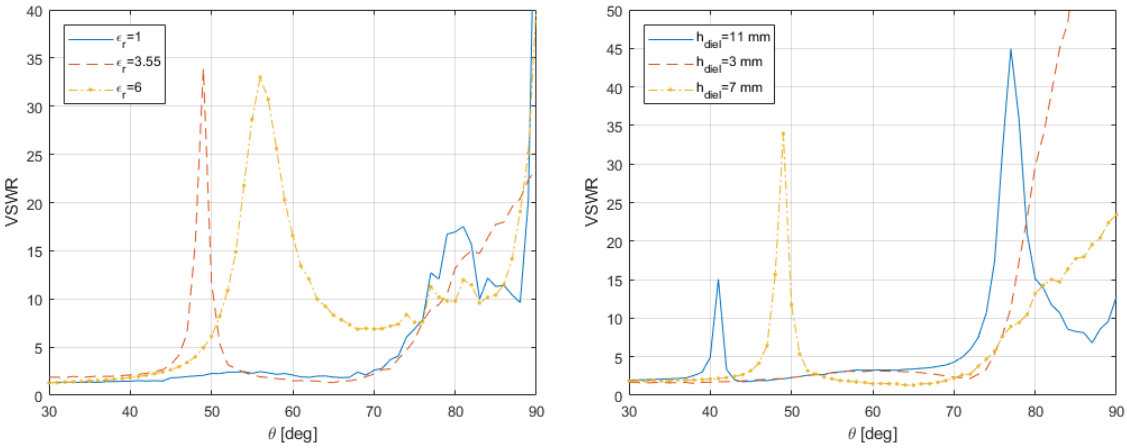

(a) (b)

Figure 2.15: VSWR vs scan angle. Plotted for different values of ϵ_r. $h_{diel} = 7$ mm (a). VSWR vs scan angle plotted for different values of h_{diel}. $\epsilon_r = 3.55$ (b)

From Fig. 2.15 we see that the VSWR has a peak at approximately 50 ° indicating that there exists a scan blindness at this angle even though the ground plane and FSS are removed. There is also a clear indication that both ϵ_r and h_{diel} make an impact with regards to when the scan blindness appears. When h_{diel} is increased from 7 mm to 11 mm, the blind spot is moved from 48° to 41°. When ϵ_r is increased from 3.55 to 6, the blind spot is shifted from 48° to 56°.

To see if these blind spots are caused by coupling to surface waves, the electric fields on the interface are plotted for scan angles $\theta = 48°$ and $\theta = 30°$ with h_{diel}=7 mm and $\epsilon_r = 3.55$. The results can be seen in figures 2.16 and 2.17.

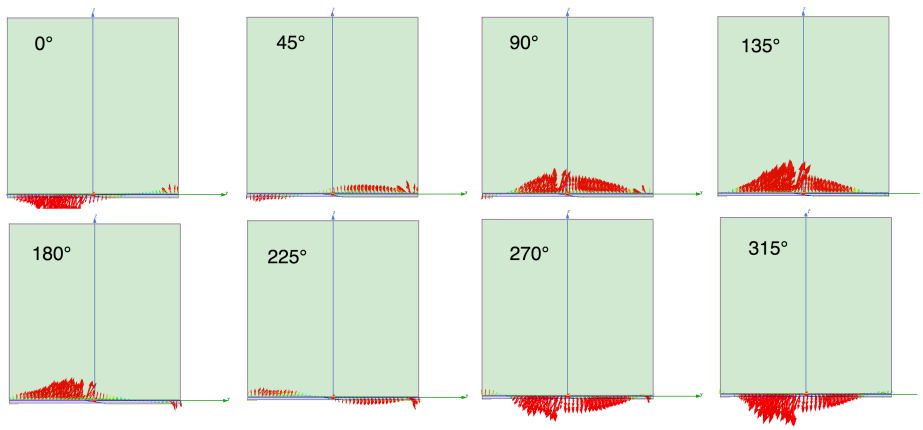

Figure 2.16: Vector representation of the electric field in the y-z plane at the interface between the dipole in Fig. 2.14b and a dielectric material for a scan angle of $\theta = 48°$. The dielectric constant of the dielectric material is $\epsilon_r = 3.55$ and the thickness of the dielectric material is $h_{diel} = 7mm$. Left-right, the phase of the field is shifted 45° per plot

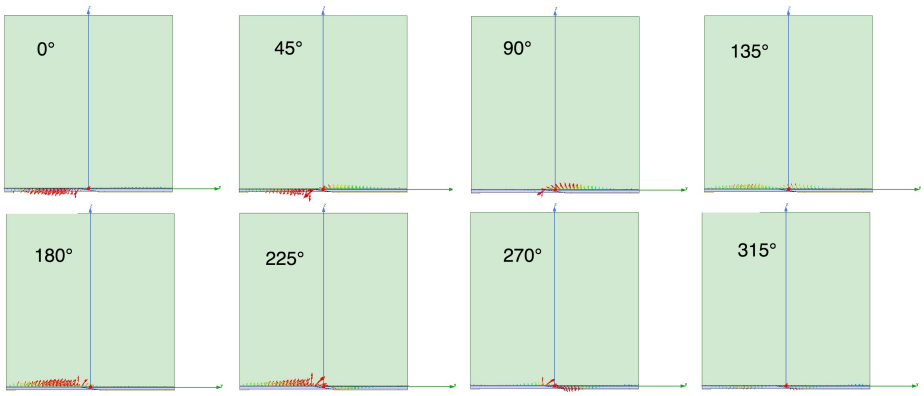

Figure 2.17: Vector representation of the electric fieldin the y-z plane at the interface between the dipole in Fig. 2.14b and a dielectric material for a scan angle of $\theta = 30°$. The dielectric constant of the dielectric material is $\epsilon_r = 3.55$ and the thickness of the dielectric material is $h_{diel} = 7mm$. Left-right, the phase of the field is shifted 45° per plot

There is a significant difference in the fields between Fig. 2.16 and Fig. 2.17. The plot in Fig. 2.16 shows a wave of significant amplitude propagating along the interface, while in Fig. 2.17 there is no significant surface wave propagating, as the amplitude is an order of magnitude lower. This shows that the scan blindness is indeed caused by a surface wave.

The experiment tells us that it is important to pay attention to the VSWR at various scan angles when designing an antenna array. Especially if the array borders with a dielectric material.

2.4 Ground plane effects on bandwidth

In a symmetrical antenna array without a ground plane, the energy will be radiated equally in both positive and negative z-direction. In applications where radiation in only one direction is wanted such as in this project, this means a half the energy is lost to radiation in the wrong direction. By adding a ground plane at a certain distance h from the array, all the energy will be radiated in one direction.

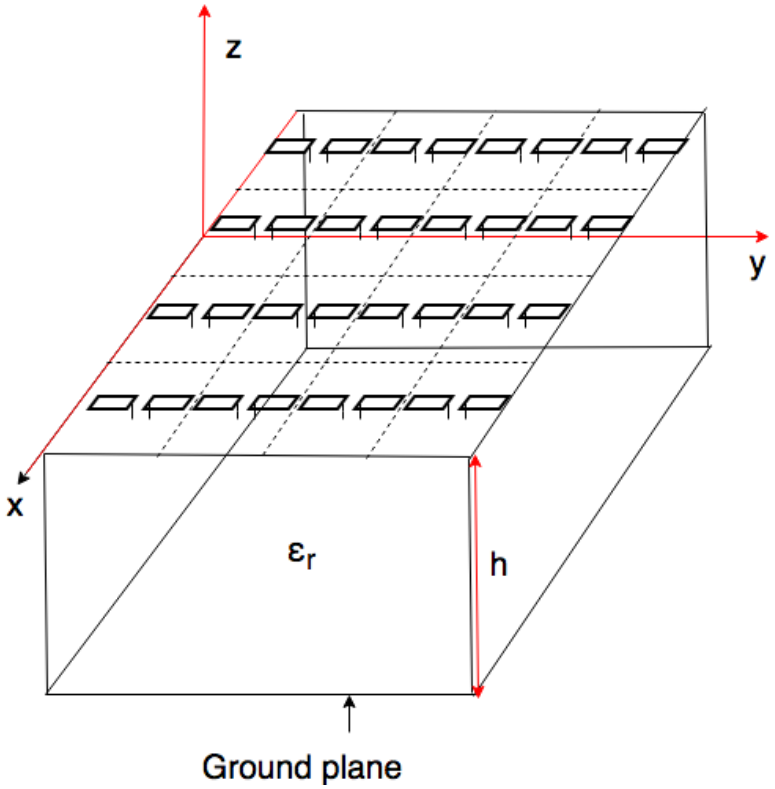

Figure 2.18: Antenna array with ground plane

Adding a ground plane as seen in Fig. 2.18 does however change the input impedance of the antenna. Most notably this is present where $h = \lambda/2$ which equals an electrical length of 180°. As the ground plane is a good conductor, the phase of a wave reflected off it is 180° out of phase with the incident wave [15]. When $h = \lambda/2$, the total distance travelled by a wave from the array to the ground plane and back is 360 °. With the 180 ° phase shift added, the reflected wave is 180 ° out of phase with the wave leaving the array as illustrated in Fig. 2.19.

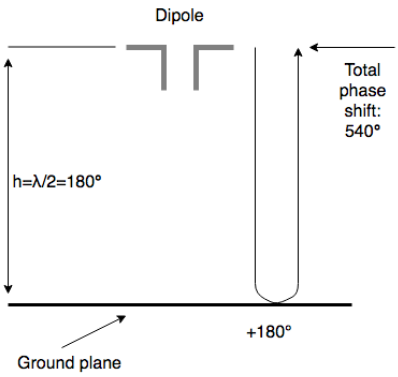

Figure 2.19: Illustration of the electrical distance travelled between the ground plane and antenna

This phase shift causes total destructive interference. Making the input impedance of the array increase towards ∞.

In addition to the problems when $h = \lambda/2$, the ground plane has a large impact on the input impedance of the array in the lower end of the frequency band. Here the imaginary part of the input impedance becomes positive (inductive).

These effects can be shown by simulating the dipole from the previous project as seen in Fig. 2.20 in an infinite array configuration using the unit cell setup seen in Section 2.3.4 with and without a ground plane.

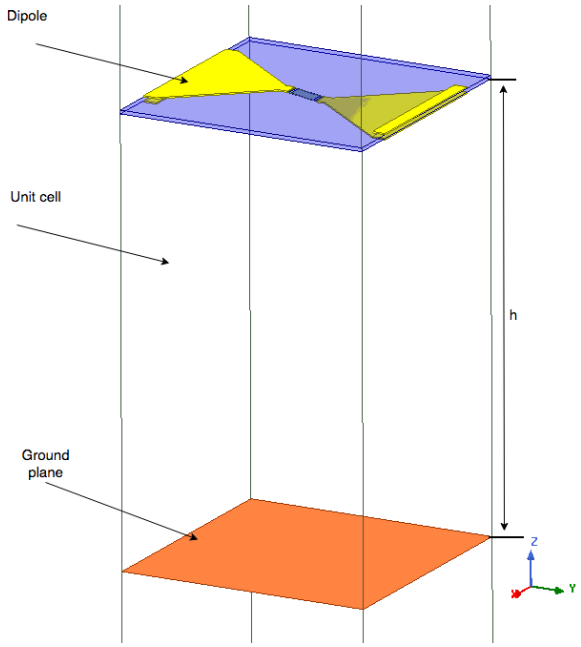

Figure 2.20: Dipole over ground plane. $h = 12$ mm. Other dimensions can be found in Fig. 2.14

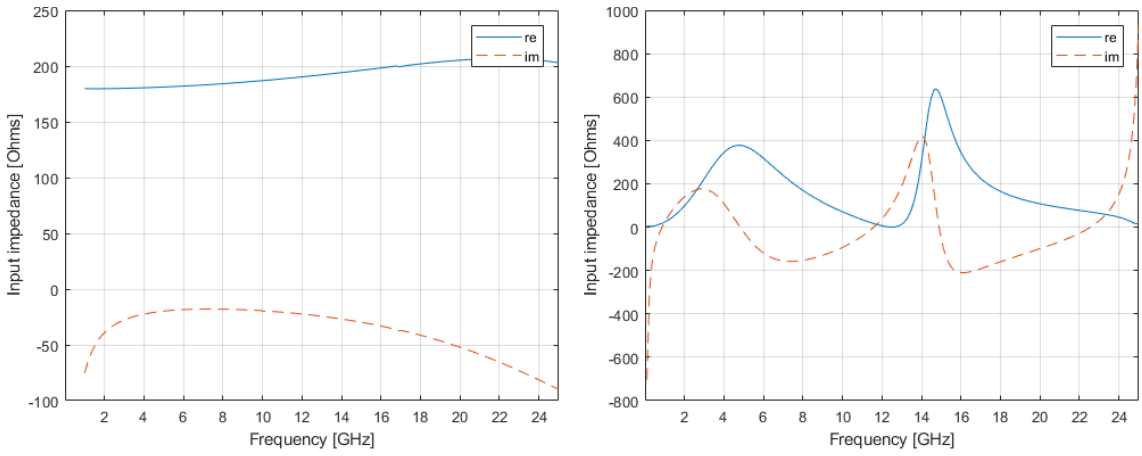

(a) (b)

Figure 2.21: Input impedance of an antenna element in an infinite array configuration with (b) and without (a) a ground plane. $Z_0 = 150\Omega$

The changes seen in the input impedance due to the ground plane largely affects the amount of energy reflected back to the source by the antenna array, as it is no longer matched to 150 Ω.

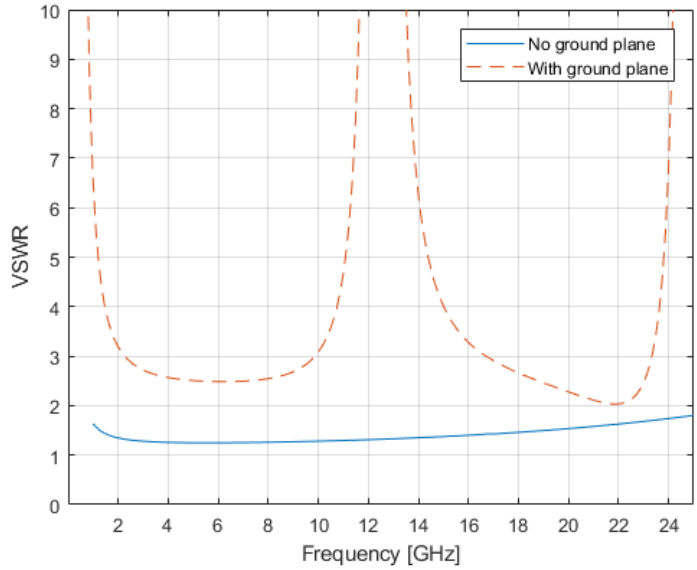

Figure 2.22: VSWR of antenna element in an infinite array configuration with (b) and without (a) a ground plane

Fig. 2.22 shows the VSWR of the antenna element . One can see a clear peak at 12.5 GHz where $\lambda/2 = 12$ mm. In addition, the changes in impedance at the low end of the frequency band has reduced the bandwidth.

2.5 Circuit representation of an antenna element in an infinite array

Representing antenna arrays as circuits provides a simple way of studying and understanding the effects of using different materials and design features. An example of such a model is seen in Fig. 2.23.

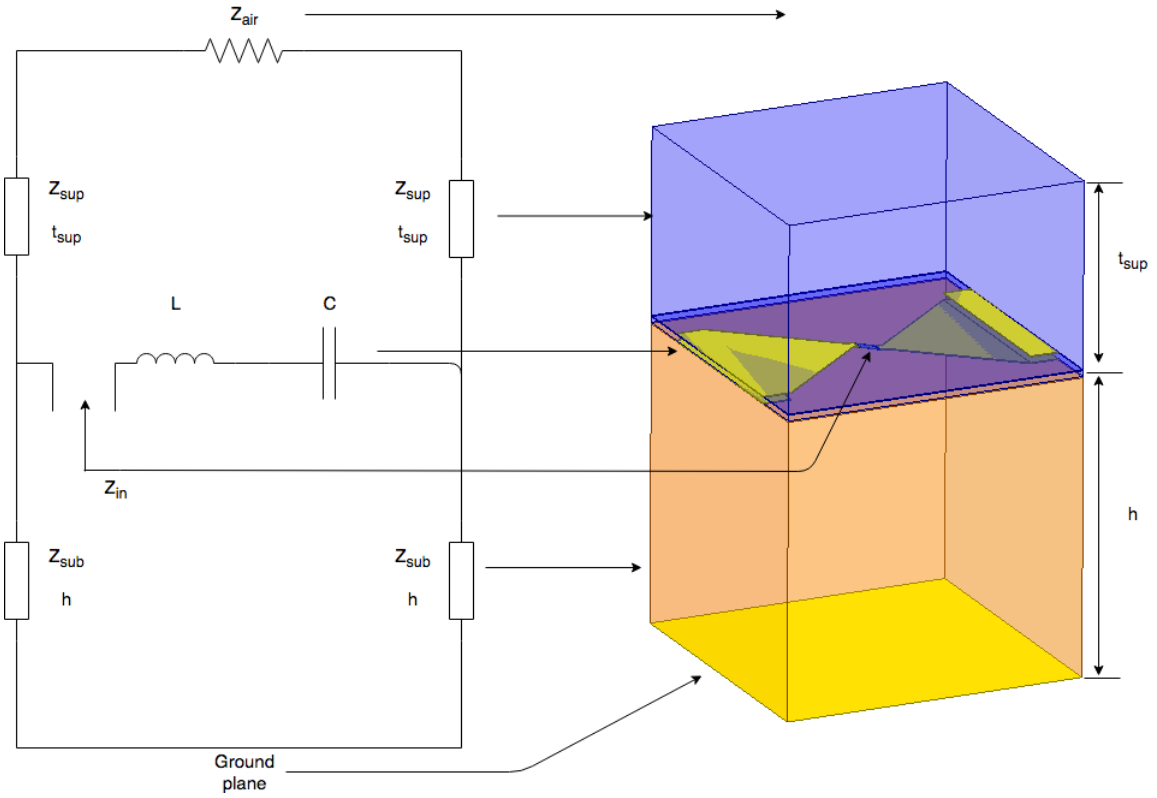

Figure 2.23: Circuit representation of an antenna element in an infinite array with the element in an unit cell configuration

This model is based on Alwan's (et. al.) model found in [23]. The superstrate (dielectric material above the dipole) and substrate (dielectric material below the dipole) are modelled as transmission lines with an impedance of half the intrinsic impedance of the material (i.e. $Z_{sup} = \eta_{sup}/2$ and $Z_{sub} = \eta_{sub}/2$). t_{sup} and h are the electrical thicknesses of the superstrate and substrate respectively. Z_{air} is the free space impedance ($120\pi\ \Omega$). This is modelled as a resistor. It can also be modelled as an infinitely long transmission line of the same impedance [23]. The dipole itself is modelled as an LC-network where L is the dipole's self inductance, and C is the capacitive coupling to nearby antenna elements. The ground plane is modelled as a short circuit of the substrate transmission lines.

2.5.1 Matching bandwidth limits for arrays over ground planes

In [24] a theoretical matching bandwidth limit of an array over a ground plane has been found using circuit models such as the one in Fig. 2.23. It is dependent on the complexity, or order of the circuit, and more complex circuits have higher potential bandwidths.

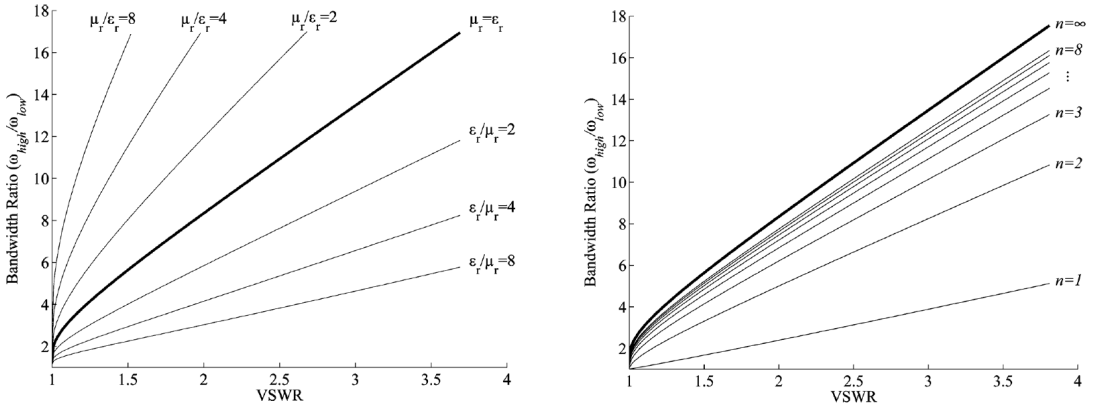

(a) (b)

Figure 2.24: Theoretical bandwidth limit of an array of infinite order plotted versus maximum allowable VSWR over a substrate with variable permeability and permittivity (a). Theoretical bandwidth of an array of order n plotted versus maximum allowable VSWR over an air substrate ($\mu_r = \epsilon_r = 1$) (b). Both figures assume the ground plane is placed at a distance of $\lambda/4$ away from the array at mid band [24]

An array such as the one in Fig. 2.23 with Z_{sup} short circuited (no superstrate), is considered a second order system [24]. From Fig. 2.24b we find that a second order system has a theoretical maximum bandwidth ratio of approximately 1:6.5 for a VSWR of 2.5. Fig. 2.24a shows the maximum bandwidth ratio for an array of infinite complexity over substrates of different permittivities and permeabilities. From this, one can see that a substrate of low permittivity/permeability ratio is preferred. Another important point which can be read from these plots is that allowing a higher VSWR can lead to a larger bandwidth.

2.6 Tightly coupled dipole arrays (TCDA)

As seen in section 2.4, the bandwidth of a normal array is severely limited by the introduction of a ground plane. In the lower end of the frequency band, this is caused by the input impedance of the antenna elements becoming inductive as seen around 2-4 GHz in Fig. 2.21b. A way to counter this effect, and bring the array closer to the theoretical bandwidth limit, is to increase the capacitance seen at the input of the antenna elements. In TCDAs this is done by moving the elements close to each other, or creating overlapping elements. Doing this increases the capacitive coupling, C seen in Fig. 2.23.

The effect this has on bandwidth can be demonstrated using the circuit model. By setting $L = 1.4$ nH, $h = \lambda/2$ for 12.5 GHz, $Z_{sub} = Z_{air}/2$ and feeding the input with a 150 Ω source, one

gets the result in Fig. 2.25 for two different values of C.

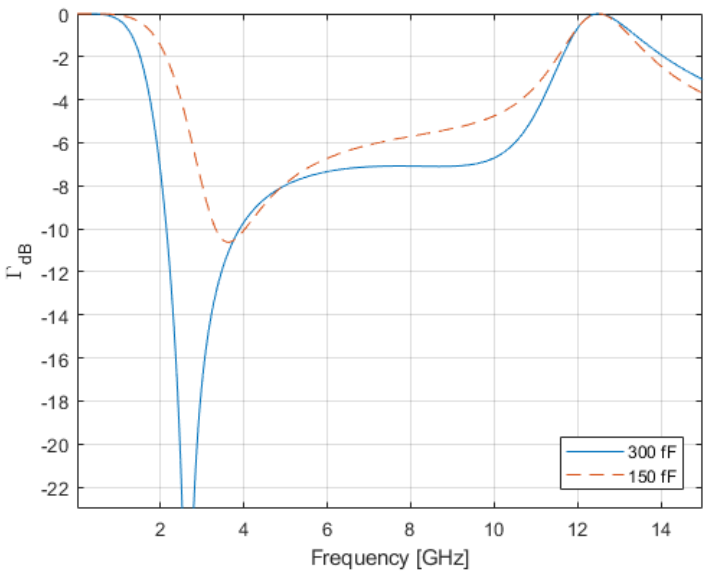

Figure 2.25: Reflection coefficient of the circuit model in Fig. 2.23 for C=150 fF and C=300 fF

Increasing C has a clear impact on the impedance bandwidth. For a VSWR of 2.5 (Γ_{dB}=-7.36 dB), the lower cutoff frequency is reduced from 2.9 GHz to 2 GHz. This improvement in lower frequencies makes it possible to place the ground plane closer to the antenna, moving the peak in reflection caused by the ground plane at $\lambda/2$ to a higher frequency.

The 150 Ω source impedance is chosen as input impedances around 150 to 200 Ω are normally seen in TCDAs [25][6][26] and it is the impedance of the antenna element from the previous project.

2.7 Superstrates

Adding a superstrate to the array as seen in Fig. 2.23 increases the order of the array, making larger bandwidths possible. In practice these materials are normally slabs of dielectric materials. The added material acts as an impedance transformer, improving the antenna's matching to free space. The effects of this can also be demonstrated using the circuit model in Fig. 2.23. Keeping the same values as used in section 2.6, with C= 300 fF, but adding a superstrate of electrical length $\lambda/4$ at 12.5 GHz and an intrinsic impedance of 250 Ω (Z_{sup} = 125 Ω), one gets the results seen in Fig. 2.26. In practical terms, the superstrate added to the antenna is roughly equal to a 4 mm thick layer of a dielectric material with $\epsilon_r = 2.25$.

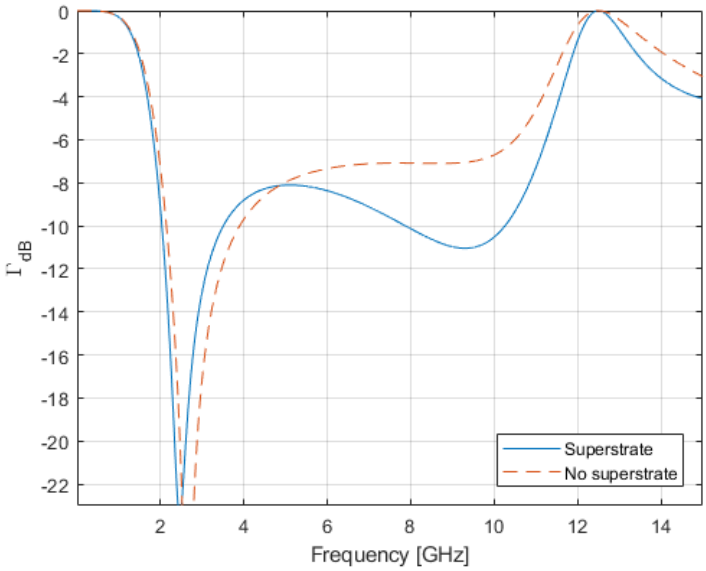

Figure 2.26: Reflection coefficient of the circuit model in Fig. 2.23 with and without a superstrate

Fig. 2.26 shows that adding a superstrate can improve the input matching, and to some degree the bandwidth of the array. In this experiment, the reflection coefficient is reduced from -7 dB to -11 dB in 9.3 GHz, while the cutoff frequency for a reflection coefficient of -7 dB in the high end of the frequency band is increased from 9.3 GHz to 11 GHz.

Increasing the number of superstrates with different ϵ_r can help increase the bandwidth of the system as seen in [4]. In terms of potential bandwidth, each superstrate adds to the order of the system [24].

With reference to section 2.3.5, it is important to note that adding a superstrate will increase the possibility of scan blindness [27].

2.8 Frequency selective surfaces

Frequency selective surfaces are, like arrays, periodic structures. They can be seen as arrays of passive antenna elements. The purpose of these surfaces is to act as filters reflecting, passing or absorbing signals of certain frequencies [27]. As FSSs are periodic spatial structures, their frequency response changes with the scan angle, and depend both on the type of element used, and the size and shape of the unit cell each element is placed in.

In UWB antenna arrays, FSSs are used both as performance enhancing superstrates and substrates. In the previous project, [25] and [5], a resistive loop FFS is placed between the dipoles and the ground plane to absorb the frequency where the distance from the dipole to the ground plane is $\lambda/2$.

Replacing the dielectric slab superstrate used in most arrays with an FSS has been shown to increase scanning performance in arrays. In [6], an FSS superstrate is used to reach scan angles of up to 75 ° In the E-plane and 60 ° in the H-plane.

2.9 Feed systems

Arrays are normally fed by a single power source through a series or corporate feed network. In a series network, the antenna elements are connected in series and the scanning can be done by varying the frequency. In a corporate network, the elements are connected through a series of power splitters and impedance transformers. The phase of each element can be controlled using phase shifters [15].

In digital arrays, however, each element has its own front end electronics. Meaning the phase and amplitude of each element is much more easily controlled. This gives extra flexibility regarding the control of the main beam but increases cost.

The use of dipoles in TCDA introduces a different problem. Dipoles require balanced feeds. Meaning the dipole arms are fed by currents equal in magnitude but 180° out of phase. In an unbalanced feed, the magnitude of the current in one of the lines is larger than the other. Feeding the dipoles with an unbalanced line limits the bandwidth due to common mode resonances appearing in mid band [28]. A typical balanced line is the coplanar strip line and typical unbalanced lines are coaxial cables and microstrip lines. As the input for this antenna will come through a coaxial cable, a transition from a balanced line to an unbalanced line (balun) is needed. While it is possible to buy ultrawideband baluns, these are costly and bulky. Therefore, to avoid increasing the size and cost of the array, the baluns should be made using PCB technology.

2.9.1 Marchand baluns

A Marchand balun is a very simple design which consists of one half-wavelength stub capacitively coupled to two short circuited quarter wavelength lines as seen in Fig. 2.27.

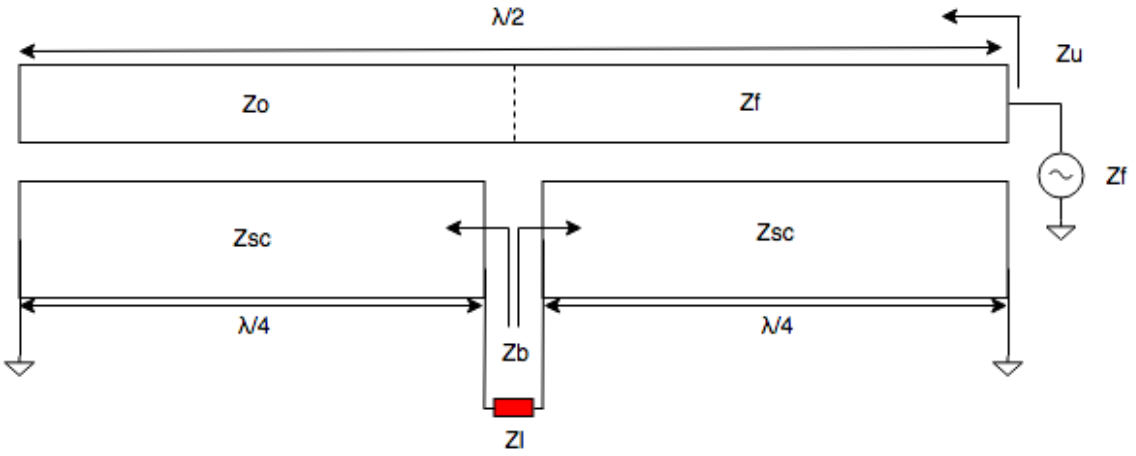

Figure 2.27: Marchand balun

The upper cutoff frequency is found where the long stub (with impedances Z_o and Z_f) is half a wavelength. Large bandwidths are achieved by adjusting the different characteristic impedances. In Fig. 2.27, the source is set to have the same impedance as the first quarter wavelength of the long stub (Z_f). The impedance of the load, or antenna element is denoted as Z_l. In general, to achieve large bandwidths, Z_{sc} needs to be very large compared to Z_o. Different optimum designs have been proposed, but the most promising, and most used is found in [29]. By setting $Z_l = Z_f$ and

$$Zo = \frac{{Z_f}^2}{2Z_{sc}}, \tag{2.64}$$

the bandwidth is in practice only limited by how high the impedance of Z_{sc} can be made while still maintaining a very low Z_o. The impedance looking into the balanced part of the balun (Z_b) and the impedance looking into the unbalanced part of the balun (Z_u) can be calculated using the formulae [29]

$$Z_u = \frac{4Z_l Z_{sc}^2 tan^2\theta + j(2Z_l^2 tan\theta - 4Z_o Z_{sc}^2 tan\theta - Z_l^2 Z_o cot\theta)}{4Z_{sc}^2 tan^2\theta + Z_l^2}, \tag{2.65}$$

$$Z_b = \frac{2Z_{sc}(2Z_f Z_{sc} tan^2\theta + j(Z_o^2 cot\theta - 2Z_o Z_{sc} tan\theta + Z_f^2 tan\theta))}{4Z_{sc}^2 tan^2\theta + Z_f^2 + Z_o^2 cot^2\theta - 4Z_o Z_{sc}} \tag{2.66}$$

where θ is the electrical length of the short circuited stubs. With these equations in combination with Eq. 2.11 and Eq. 2.15, the VSWR and bandwidth of a Marchand balun with given impedances can be calculated. As an example, we can let Z_l and Z_f have an impedance equal to that of the TCDA in the previous project, 150 Ω and plot the VSWR for different values of Z_{sc}.

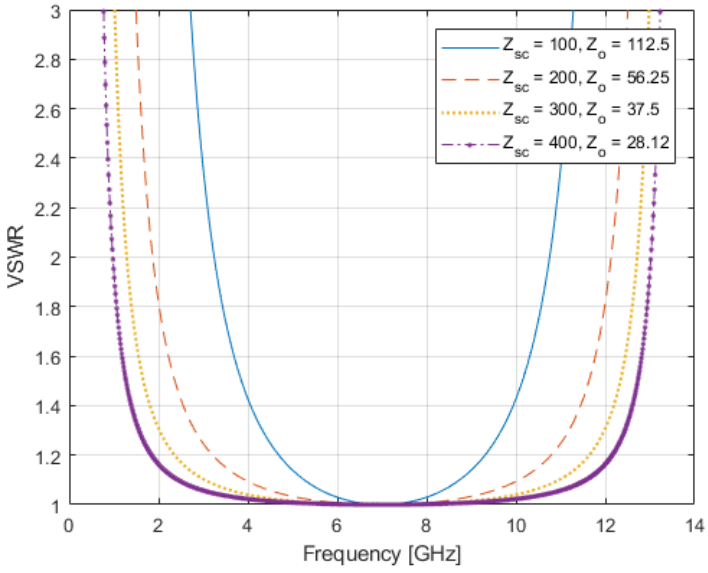

Figure 2.28: VSWR of a optimum Marchand balun with center frequency at 7 GHz

As expected, the bandwidth increases with Z_{sc}, and is in theory infinite for an infinitely large Z_{sc}. Realistically, a bandwidth ratio of more than 1:10 for a VSWR of 2 ($Z_{sc} = 300\Omega$ gives a bandwidth of 1:9.86) could be realized depending on the materials and dimension of the balun. This is also limited by the matching network needed to match the 150 Ω input impedance of the balun (Z_f) to the 50 Ω impedance of the source.

With its simple design, the Marchand balun has clear advantages in terms of design and production. It is capable of achieving very large bandwidths, and has no inherent problems with resonant frequencies within the operational frequency band. It is, however dependent on having a large variance in impedances, and on a taper or other matching networks at the input.

2.9.2 Double-y baluns

A double-y balun is a transition between an unbalanced coplanar waveguide and a balanced coplanar stripline. At the transition, each line divides into two stubs. One short circuited and one open as can be seen in Fig. 2.29.

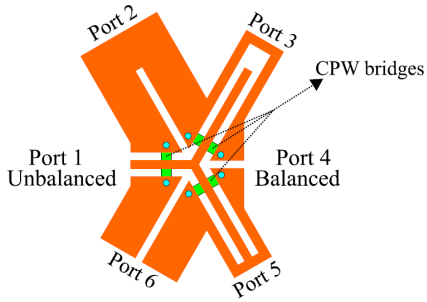

Figure 2.29: Double-y balun geometry [30]

In Fig. 2.29, port 1 and port 4 represent the CPW and CPS lines respectively. Port 2 and port 5 are the short circuited stubs and port 3 and port 6 are the open stubs. The network is all-pass up to the frequency where the length of the stubs is equal to $\lambda/8$. It does, however require the CPW and CPS lines to have equal impedance.

The double-y balun has been show to support a bandwidth of 300 kHz to 4 GHz (1:13333) for a VSWR of 1.3 [31]. This, however is achieved using very narrow spacing (50 μm) in the CPW lines. A downside to this balun is that it supports common mode resonances where the lines feeding the balun itself are equal to odd multiples of $\lambda/2$ [32][7].

2.10 Simulation setups

2.10.1 3D simulations

Ansys HFSS is used for all simulations of 3D-models in this project. For antenna designs, a unit cell approach is used. In this setup, the top of the unit cell is terminated in a Floquet port, which excites a certain number of Floquet modes. The cell walls are set up as master and slave boundaries, where

the fields seen at the master border are copied to the slave border. This means the antenna element acts as if it is in an infinite array. The main reason for using this type of setup is that is saves an enormous amount of processing time. The processing time for an antenna element in an array is roughly the same as for a single stand-alone antenna element depending on the amount of Floquet modes excited by the Floquet port, while simulating an NxM array roughly takes the same amount of time as a single element multiplied by the number of elements in the array. This setup does not account for edge effects, but if the array is sufficiently large, these are negligible for the center elements.

When edge effects need to be simulated, the chosen method is the unit cell domain decomposition method. Here the mesh from a single unit cell is repeated to make up the entirety of the array. This method requires less memory than the alternative method of doing a full finite element domain decomposition as the the individual cells do not have to be solved in parallel. Extra efficiency is gained by exploiting the repetitive nature of elements in similar environments [33].

2.10.2 Circuit simulations

The circuit simulations in this project are done using Agilent Advanced Design System

Chapter 3

Design and production

This chapter contains the design of the antenna element and array. It starts off at the antenna element design from the previous project, and explains the design choices which have to be made in order for the design to be realizable with an integrated balun. These changes include turning the dipole into a vertical position, moving both arms of the dipole to the same side of the PCB to simplify feeding of the dipole and removing the FSS. With the balun and antenna element ready, they are combined to form a TCDA with integrated balun. Here, some simulation results are presented, and a section explaining the production of the array is added.

3.1 Antenna element design

In the previous project, an UWB antenna array without a feed network similar to the one in [25] was designed. The element was to be used in this project. The dipole with dimensions was presented in Section 2.3.5, and can also be seen again in Fig. 3.1. The unit cell size of this element is 6.815x6.815 mm or approximately $\lambda/2$ at 22 GHz to avoid grating lobes inside the impedance bandwidth.

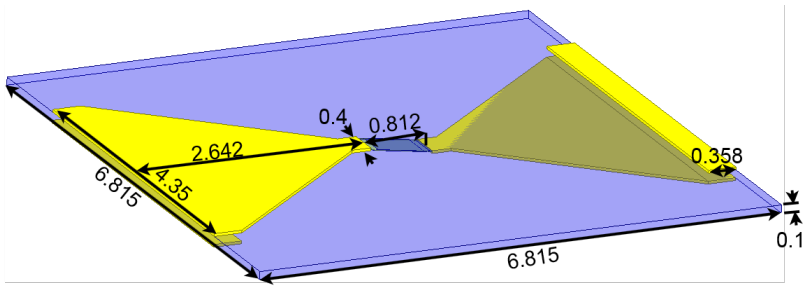

Figure 3.1: Dipole dimensions

The dipole is placed horizontally on a 100 μm layer of polyimide ($\epsilon_r = 3.5$), and the arms of the dipole are placed on opposite sides of the polyimide layer to create the overlapping sections or parallel plate capacitors.

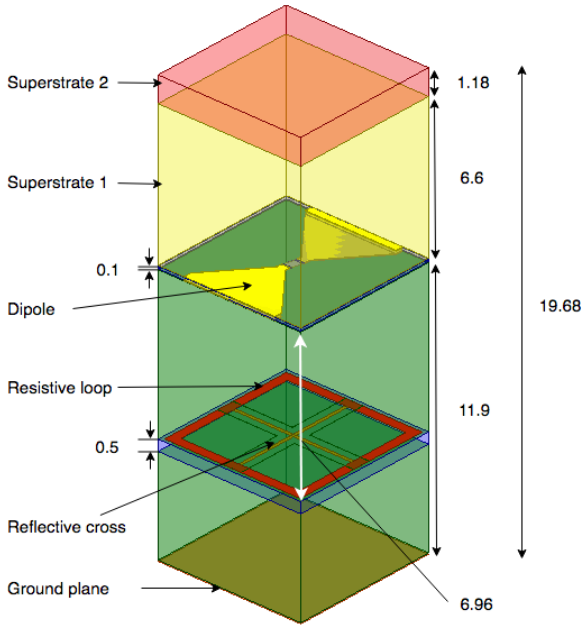

Figure 3.2: Antenna element from the previous project. All dimensions in mm

Fig 3.2 shows the antenna element. The dipole is suspended above a resistive (50 Ω/sq) loop FFS placed on a layer of Rogers RT/duroid 5880 ($\epsilon_r = 2.2$) whose dimensions can be seen in Fig. 3.3. The layers between the dipole and FSS and between the FSS and ground plane are filled with a low permittivity material like divynicel ($\epsilon_r = 1.05$).

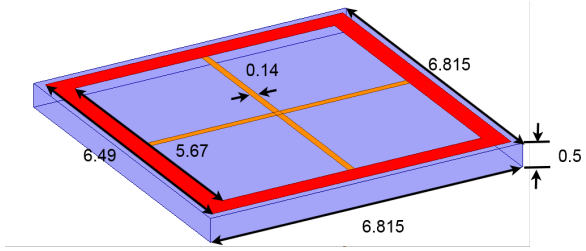

Figure 3.3: Frequency selective surface from previous design. All dimensions in mm

The purpose of this FSS is to mitigate the destructive interference caused by the ground plane at the middle of the frequency band by burning away some of the power. While this reduces the efficiency of the antenna, it nearly doubles the impedance bandwidth. The tall superstrate made from a thick layer of Rogers RO4350B ($\epsilon_r = 3.66$) and a thin layer of RT/duroid 5880 on top of the dipole improves the radiation efficiency and matching by acting as an impedance taper. In addition to this, a reflective cross is added in the center of the resistive loop to reflect some of the energy before it is burned in the loop, giving a slight increase in efficiency.

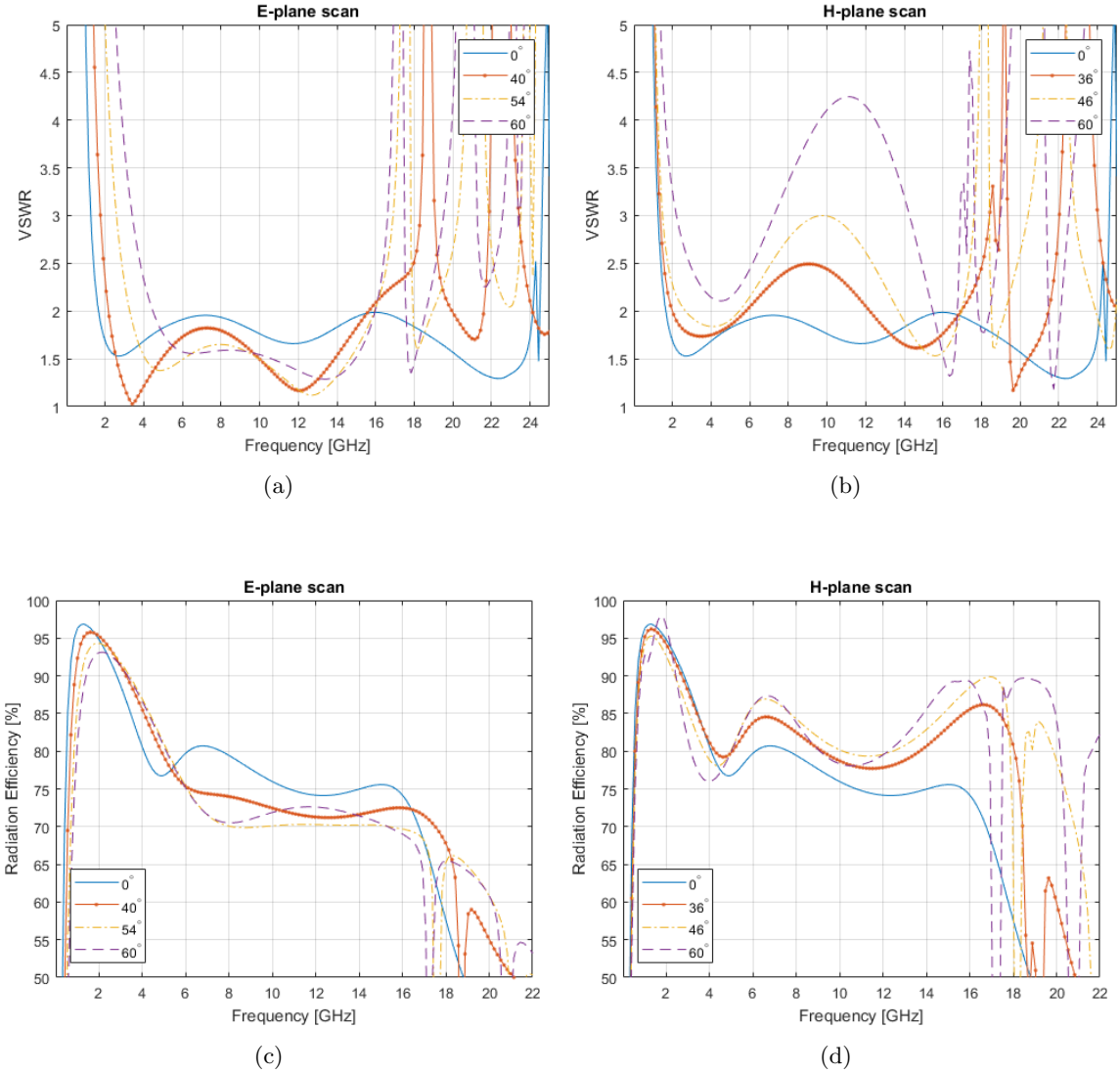

Figure 3.4: Simulated VSWR and radiation efficiency at different scan angles in the H-and E planes

Fig 3.4 shows the VSWR and radiation efficiency of this array in different scan angles. With an efficiency of 70 % and a VSWR of 2 as the limit, the array achieves an impressive bandwidth of 1.64-16.78 GHz (1:10.2) broadside. The rise in reflection during H-plane scanning around 10 GHz was originally believed to be a result of the FSS not affecting the TE Floquet mode in the same way as the TM Floquet mode, however, the problem was found to be a result of the superstrate being too thick. Reducing the thickness of superstrate 1 from 6.6 mm to 3 mm improves the VSWR during H-plane scanning.

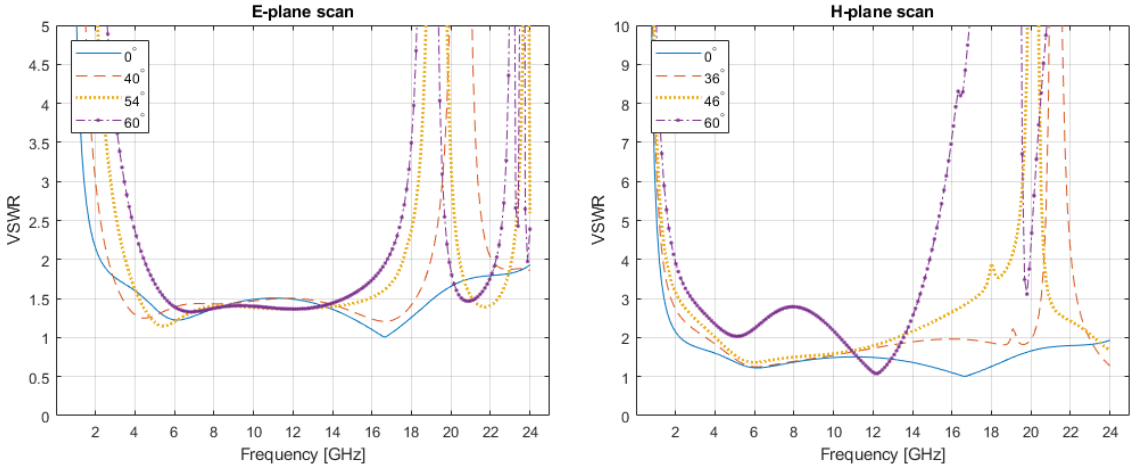

(a) (b)

Figure 3.5: Simulated VSWR during scanning with superstrate 1 reduced to 3 mm

Fig. 3.5 shows the VSWR with the thickness of superstrate 1 reduced. While reducing the thickness will change the efficiency of the antenna (it was optimized for maximum efficiency and VSWR at broadside), this result shows that a better optimization of the superstrate and FSS could produce better results.

3.1.1 Redesign for feed implementation

Implementing a feed system in this design proved difficult due to different factors. Firstly, a balun would have to pass through the reflective cross on its way to the dipole. Meaning this part of the FSS would have to be altered or removed. Connecting the balun to the dipole also poses a challenge, as the PCB would have to pass through the polyimide layer the dipole is printed on.

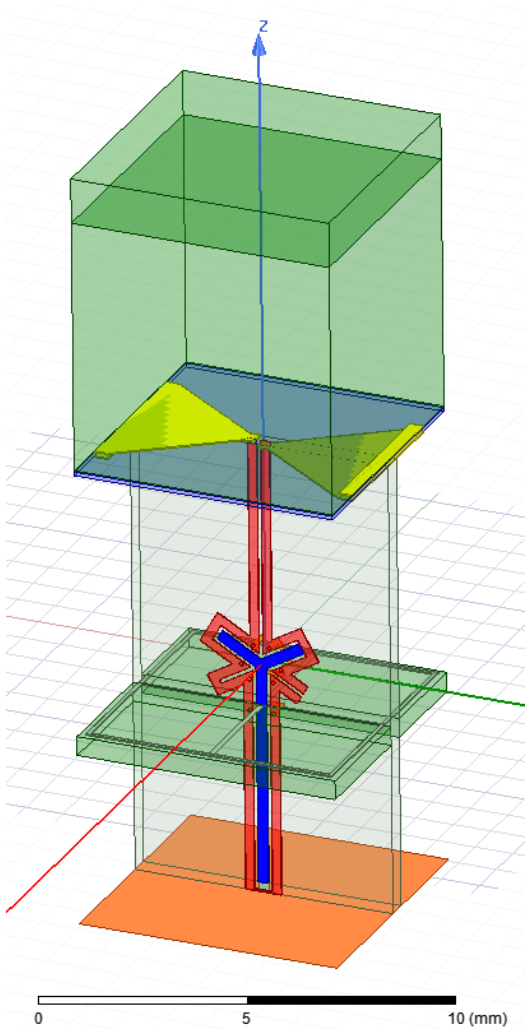

Figure 3.6: Sketch of dipole fed by double-y balun

Fig 3.6 shows what the antenna would look like fed by a double-y balun. Note how the PCB of the balun passes through the reflective cross. The most critical factor, however is the point where the balun connects to the dipole. In this design, the solder pads on the dipole are 0.4 mm wide as seen in Fig. 3.1. In order fit an entire PCB through the polyimide layer, the solder pads would have to be widened. In addition, moving both arms of the dipole to the same side of the substrate would ease soldering. Attempts to make a producible design with the dipole in this horizontal position without significant reduction in performance were not successful. For lower frequency designs, this method of feeding the dipoles is feasible as seen in [5] simply because the designs are physically larger.

The solution to this problem is to rotate the dipole into a vertical position as seen in Fig. 3.7.

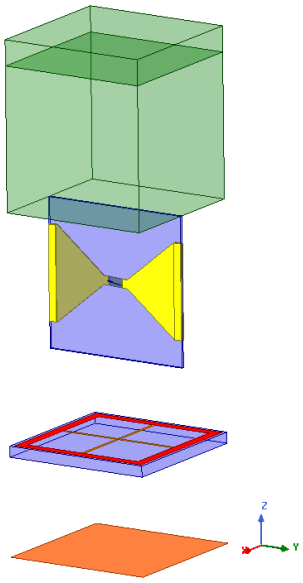

Figure 3.7: Vertically oriented dipole. With reference to Fig. 3.2, the difference is that the dipole has been rotated 90° around the y-axis, and the superstrates have been pushed 3.41 mm in the positive z-direction. The divinycel layer has been removed to reduce simulation time.

While this initially increases the VSWR significantly during an H-plane scan and at broadside, it also has a positive effect on VSWR in high scan angles in the E-plane. With a dipole in this position, scan blindness no longer appears at high frequencies (the scan blindness can be seen as high peaks in the VSWR around 17-18 GHz in Fig. 3.4a and is the same scan blindness as discussed in Section 2.3.5). Meaning the scan volume is greatly increased. The simulated results can be seen in Fig. 3.8. Further, the vertical orientation enables the dipole to be printed on the same PCB as the balun. This is a big plus with regards to manufacturing as it eliminates the need for soldering, and possibly the need for a material (like the divinycel in the previous project) placed between the different layers of the antenna. The divinycel layers and soldering would be potential factors for manufacturing error, as these would be harder to recreate accurately compared to a PCB.

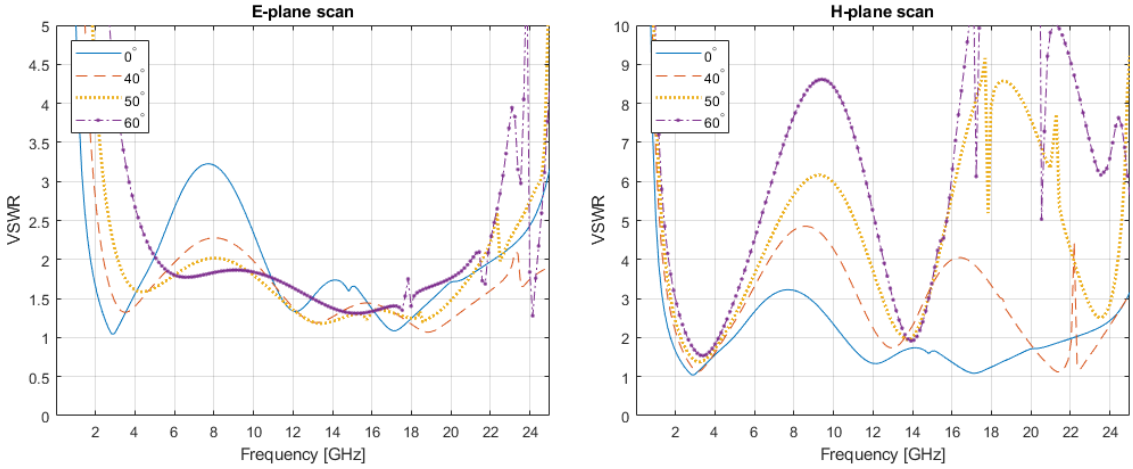

(a) (b)

Figure 3.8: Simulated VSWR during scanning with vertical dipole

Fig 3.8 shows the VSWR when scanning in the two planes. Note that this simulation was done using the full size superstrate seen in Fig. 3.2.

As mentioned earlier, both arms of the dipole are moved to the same side of the substrate. This time to ease the feeding a signal to the dipole as seen in Fig. 3.9.

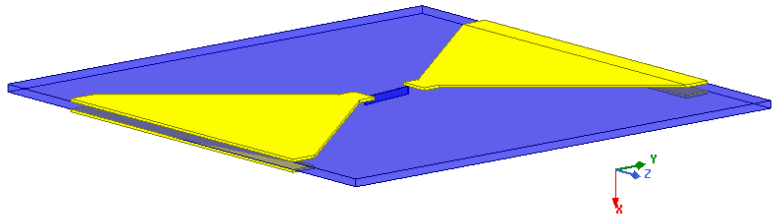

Figure 3.9: Dipole with arms on the same side of the substrate

This alters the overlapping structure, but enables the dipole to be fed by a balun without via holes.

3.1.2 Materials selection

The RT/duroid 5880 ($\epsilon_r = 2.2$) materials used in this design are dropped due to long lead times and price. Instead, the more readily available material Rogers RO4350B ($\epsilon_r = 3.66$) is used for the PCBs and cheap plastics like polyethylene or polypropylene are used for the superstrate. The flexible polyimide material used in the antenna element is not used as the PCB needs to be rigid for the new design.

3.1.3 Frequency selective surface

One of the most important features of the previous antenna element design, is the resistive FSS which gives the array its impressive impedance bandwidth. The impedance bandwidth of the array is 1.64-24.16 GHz (1:14.73) at broadside, while the theoretical maximum for an infinite order array without the FSS is approximately 1:12 [24]. A bandwidth of more than 1:12 is hard to achieve in a balun on a relatively thin RO4350B substrate as seen in section 2.9.1. The PCB of the FSS would have to intersect the PCBs of the baluns/dipoles. For a design of this size, this is a big manufacturing challenge. For each antenna element, a cut would have to be made in the PCBs. This would cause the PCBs to lose rigidity, and possibly limit performance. Due to these factors in combination with the added resistive loss, the FSS is removed. The immediate response of the antenna to removing the FSS is of course a drastic increase in VSWR as seen in Fig. 3.10a

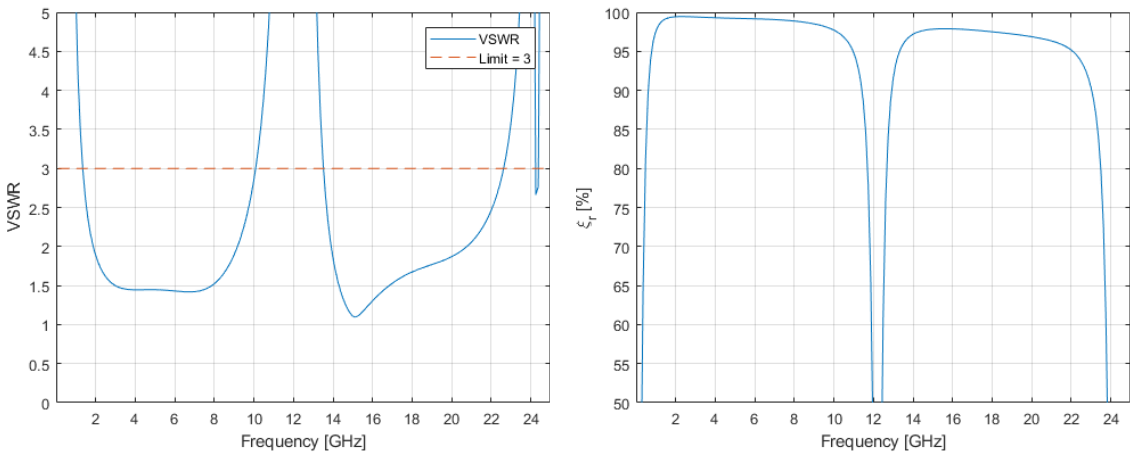

(a) (b)

Figure 3.10: VSWR (a) and radiation efficiency ξ_r (b) of antenna when FSS is removed

The bandwidth at this point is still reasonably good at approximately 1:6.5 for a VSWR of 2.5. However the spike in VSWR causing a cutoff at a too low frequency (9.7 GHz for a VSWR of 2.5). This can be solved by moving the ground plane closer to the dipoles. Removing the FSS brings the radiation efficiency up from a minimum of 70% to over 95 % for the entire bandwidth, making the antenna more suitable for radar applications.

3.1.4 Antenna element size

As the high end of the array's bandwidth now is limited by destructive interference from the ground plane, the small 6.815x6.815 mm ($\lambda/2$ for 22 GHz) size of the unit cell can be changed. Increasing the size of the unit cell leads to a larger gain, as per Eq. 2.40. It also makes designing the feed network easier. Simply because there is more space. With a size of of 6.815x6.815 mm, one can barely fit a standard sub-miniature version P (SMP) socket [34] within the unit cell. In addition, the baluns would be so closely spaced that they might interfere with each other. The size is increased to 10.707x10.707 mm ($\lambda/2$ for 14 GHz). From Eq. 2.62 the first grating lobe for a scan angle of 60° should appear at approximately 15 GHz with this unit cell size.

3.1.5 Antenna element performance after redesign

This section is added to show an example of what the antenna element looked like after the modifications described in the previous sections. This is not what the final dimensions of the design will look like, since its impedance has to be matched to the balun. The element is not perfectly optimized, but it does give an insight into what performance can be expected from the final design.

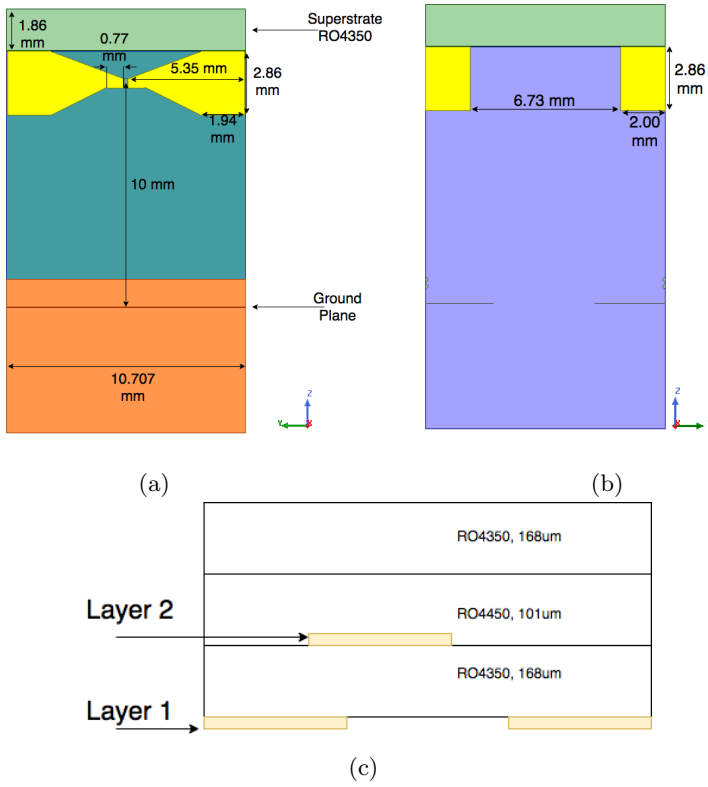

Figure 3.11: Dipole before integration. Copper layer 1(a), copper layer 2 (b), and stackup noted with type of material and thickness of the substrate layers in μm (c)

Fig. 3.11 shows the antenna element. Note that the width of the dipole ends is greatly reduced compared to the design in Fig. 3.1. This improves the matching when the dipole is placed in a vertical orientation over the ground plane. The stackup contains an extra substrate to accommodate a future balun (see section 3.3 for details). In addition, the center of the dipole is formed to allow feeding it from a coplanar strip. The RO4450 layer is a bonding layer used to "glue" the two RO4350B substrates together. The glue conforms to the shape of the copper tracks in the layer bordering it. The ground plane is moved closer to the antenna to move the frequency band to higher frequencies, and the superstrate is a single layer of RO4350B.

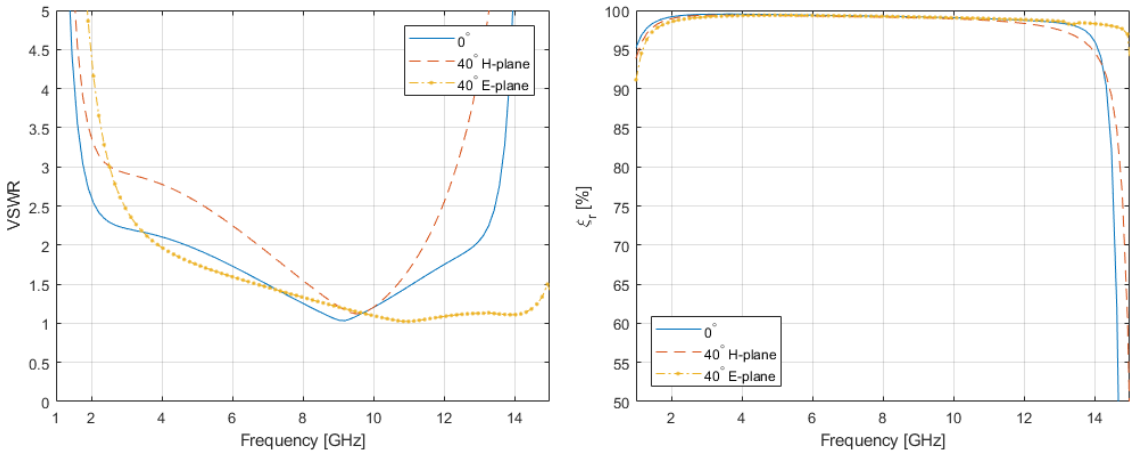

(a) (b)

Figure 3.12: Simulated scan performance of vertical design example. VSWR (a) and radiation efficiency ξ_r (b)

Fig. 3.12 shows the performance of the antenna element. It has a bandwidth of 2-13.5 GHz (1:6.75) for a VSWR of 2.5 at broadside ($\theta = 0$) and the radiation efficiency is $> 97\%$ for this entire band. Again, the increased scan performance due to turning the dipole vertically can be seen in the E-plane.

It has to be noted that at this stage in the design process, the antenna element is starting to resemble another TCDA design for a slightly higher frequency band (3-18.5 GHz), namely Novak's array in [8]. This has to be expected as they are both made using the same design processes and techniques. The main differences are the choice of materials and the frequency band.

3.2 Double-y balun

As the double-y balun is in theory an all-pass network with an extreme bandwidth potential as seen in Section 2.9.2, and designs for use in TCDAs have yielded good results [7] an attempt was made to design one for this project.

One of the main challenges in designing a double-y balun, is the impedance of the lines. For maximum bandwidth, the CPS and CPW lines need to have the same characteristic impedance.

While this implies an impedance transformer at one of the ports (In order to match the 150 Ω input impedance of the antenna), it also puts strict requirements on the choice of substrate and substrate thickness. As mentioned in section 3.1, the low permittivity material Rogers RT/duroid 5880 is dropped due to long lead times. In order to achieve an impedance of 150 Ω in both the CPW and CPS lines at the same time, the dielectric constant has to be low. As seen in Fig. 2.8, an impedance of 130 Ω is possible for a <0.5 mm thick RO4350B substrate. To reach 150 Ω, the dielectric constant has to be lower.

In addition to the problems regarding the characteristic impedances of the lines, the common mode resonance occurring when the length of the input lines equal $\lambda/2$ made the design difficult. In [7], the designers eliminated this common mode resonance by introducing resistively loaded shorting pins. This however, introduces loss. The design attempt can be seen in Fig. 3.6, however the results were never good enough to be added to this report.

Due to these problems, the double-y balun was dropped in favour of the simpler Marchand balun design seen in the next section.

3.3 Marchand Balun

As seen in section 2.9.1, in order for the Marchand balun to reach the large bandwidth required by this project, largely different characteristic impedances have to be realized within the balun. This means large variations in line widths. Using the variation with $Z_{sc} = 300$ and $Z_o = 37.5$ in a microstrip configuration as an example; the 300 Ω line would be a line of width 2 μm on a 0.6 mm RO4350B ($\epsilon_r = 3.66$) substrate, while the 37.5 Ω line would be approximately 2 mm. The 150 Ω lines would be around 0.1 mm. It is obvious that this is not producible. The 2 μm line is impossible to produce using normal PCB production techniques and the 2 mm line is very large relative to the unit cell of the antenna elements.

The solution to this problem is proposed in a range of articles [6][35][26][8][5]. Instead of placing all the lines on a single layer, the PCB is made of three layers as shown in Fig. 3.13. On the bottom layer, the high impedance line (Z_{sc}) is made as a coplanar stripline which allows far greater impedances than the microstrip line without a large increase in size. This line also works as an extension of the ground plane. Meaning the input (Z_f) can be made as a microstrip line on the top layer using the CPS as a ground plane. By extending one end of the high impedance line to cover both the top and bottom layer using vias, the low impedance line (Z_o) can be made as a stripline in the middle layer. Striplines can be made with very low impedances. Fig. 3.13 shows a sketch of this design solution.

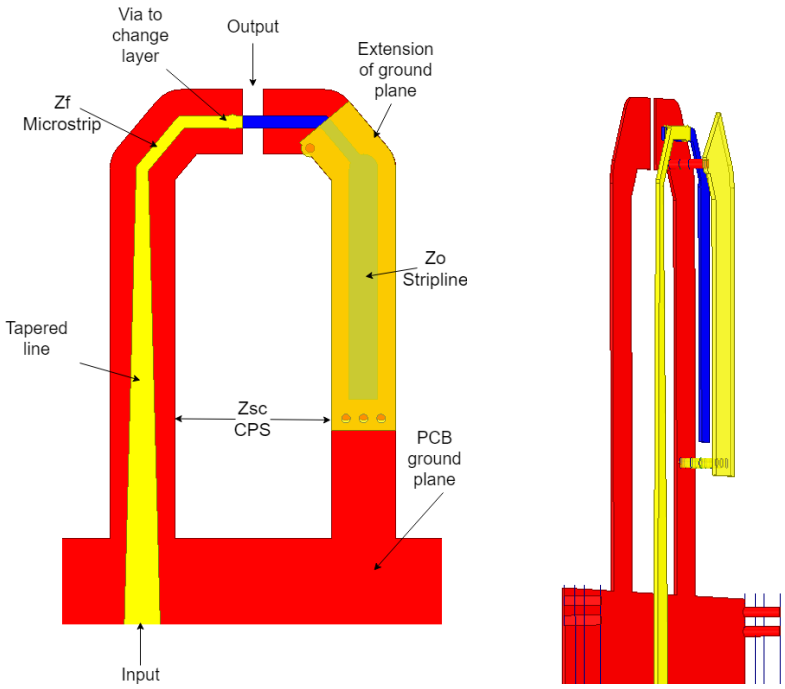

Figure 3.13: Balun design. Front view (a) and side view (b)

3.3.1 Matching to 50 ohm

Due to the high impedance seen at the unbalanced port (Z_f) of the balun (with reference to Section 2.9.1, this impedance should be the same as the dipole's impedance, i.e. 150 Ω), an impedance transformer is needed to match it to the 50 Ω impedance of the connector. There are different ways to solve this. Designs [5][26][35] propose putting two antenna elements in the same unit cell and feeding them with the same signal through a Wilkinson power divider. While designs [6] and [8] use tapered lines to transform the impedance.

Wilkinson power dividers or tapered line

A Wilkinson power divider is a network which splits the incident power between its output ports. It can be made to split the power equally or unequally between the ports. An example can be seen in Fig. 3.14.

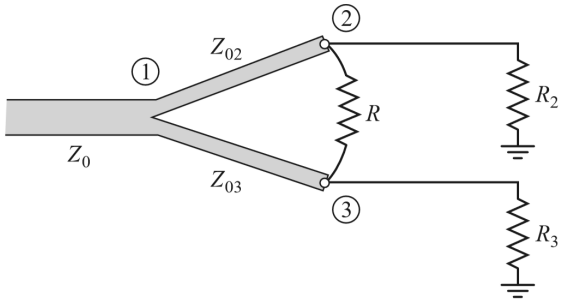

Figure 3.14: Two-way Wilkinson power divider [11]. Z denotes the characteristic impedances of the lines, R_2 and R_3 are the loads

For equal power division, the impedances Z_{02} and Z_{03} will be equal to each other and double that of the input line Z_0. The two output ports are isolated, as any mismatch between them is burned in the resistor R [11].

The idea behind using a Wilkinson power divider in the TCDA is that the impedance of the unit cell is proportional to the ratio d_y/d_x, and that by splitting d_x into two parts, each containing an antenna element with balun, the input impedance of the elements is approximately halved. In the case seen in [26] the impedance of the antenna element was 200 Ω before splitting the cell, and 100 Ω after. The 50 Ω input could then be split into two 100 Ω lines using a Wilkinson power divider, eliminating the need for an impedance transformer. Doing the same for this design, however would make the antenna elements very small ($d_x/2 = 5.3$ mm) , and the baluns would be very closely spaced, possibly interfering with each other (The impedance of the CPS is very dependent on the distance between the conductors. A unit cell size of 5.3 mm could lead to them actually being closer to the conductors from adjacent unit cells than the conductors in their own cell). It is important to note that the designs using this method have unit cells about triple in size compared to this design as they are made for lower frequencies (< 6 GHz). Increasing the size of the unit cell to accommodate two baluns would push the first grating lobe into the bandwidth. Inserting a Wilkinson power divider will also introduce a small loss when scanning due to the two elements receiving signals of slightly different phases. This phase difference will cause a current to pass through the resistor in the divider leading to ohmic losses.

The tapered line solution is seen as an easier alternative, which does not require splitting the unit cell. The designs in [6] and [8] use a meandered tapered line in order to increase its length without increasing the height of the array. For the design in this report, a shorter taper was used. This acts as a part of the overall matching network if optimized correctly.

3.3.2 Marchand balun design before integration with dipole

A Marchand balun was designed using the design solutions discussed above to study its performance before trying to integrate it in the antenna element. The design can be seen in Fig. 3.15.

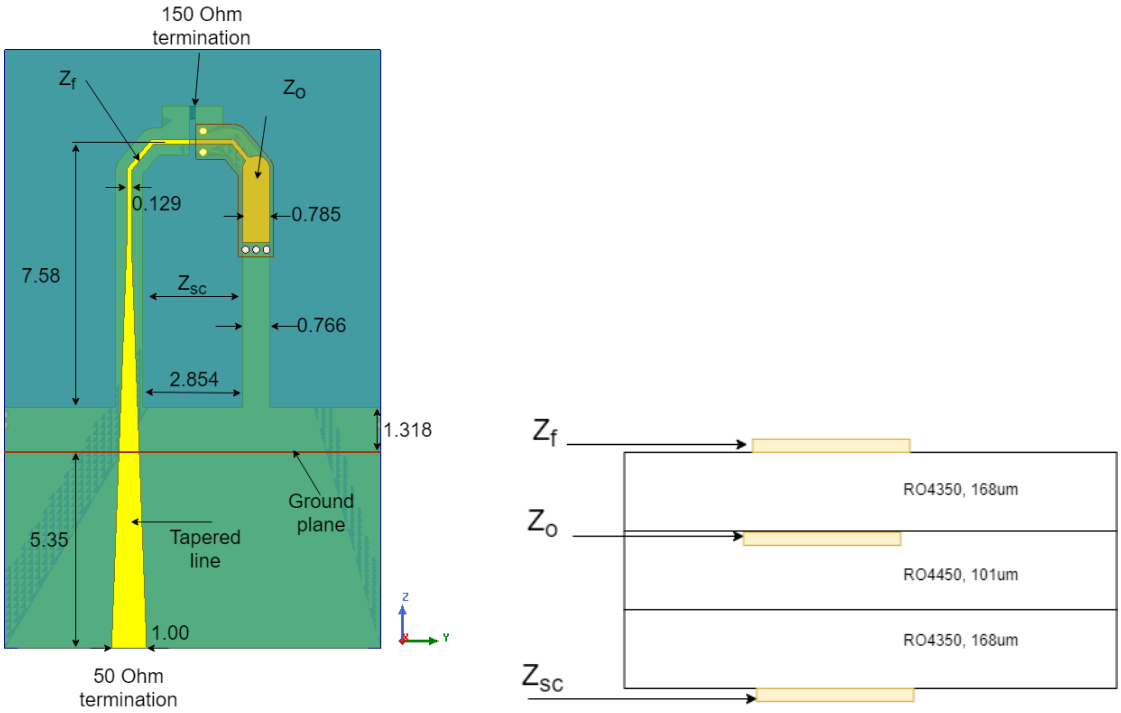

Figure 3.15: Balun example (a). Dimensions in mm unless otherwise specified. Stackup marked with type of material and layer thickness in μm (b)

As can be seen, the balun is placed above the ground plane with the taper going through to the bottom of the PCB. This is done to avoid building additional thickness in the array. Using the formulae in section 2.2.3, the dimensions in Fig. 3.15 should give approximately (Z_f,Z_o,Z_{sc})=(115 Ω, 22 Ω, 283 Ω). Which, in theory, following section 2.9.1 should produce a bandwidth of 1-13 GHz for a VSWR of 2.5. This is assuming the coplanar strip maintains a distance of 2.854 mm to maintain a Z_{sc} of 283 Ω until terminated. As seen in Fig. 3.15a, this is not the case, since the tracks meet at the 150 Ω termination. Adding in the short tapered line also reduces the bandwidth to some degree.

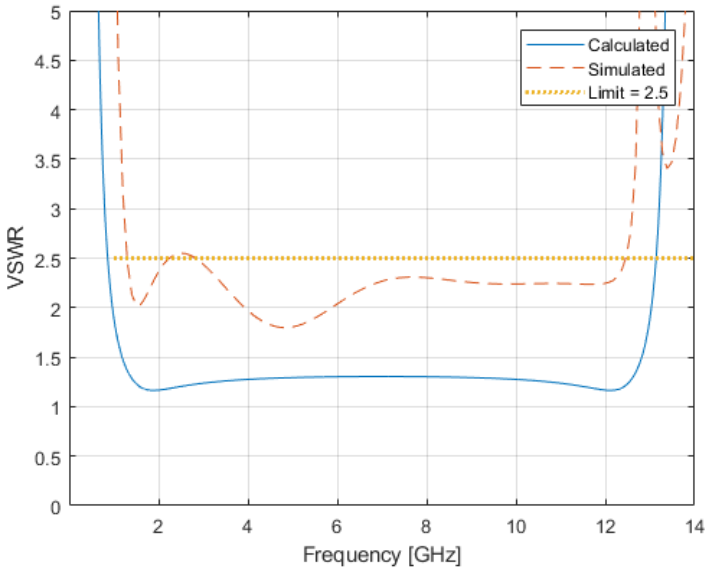

Figure 3.16: VSWR of the balun in Fig. 3.15

Fig. 3.16 shows the VSWR seen at the 50 Ω input port of the balun. As expected, the simulated bandwidth is reduced compared to the calculated bandwidth. In addition, the VSWR is generally higher. The bandwidth for a VSWR of 2.55 is 1.3-12.5 GHz (1:9.6).

3.4 Connector interface

The SMP connector from Molex [34] was modelled in HFSS to avoid any problems with mismatch at the interface between the connector itself and the 50 Ω input of the antenna element. The interface i.e. from where the connector is soldered to the PCB to the antenna element itself is a simple transition from a 50 Ω grounded coplanar waveguide to a 50 Ω microstrip line. An overview of the interface and model can be seen in Fig. 3.17. Dimensions and further details can be seen in Section 3.6.

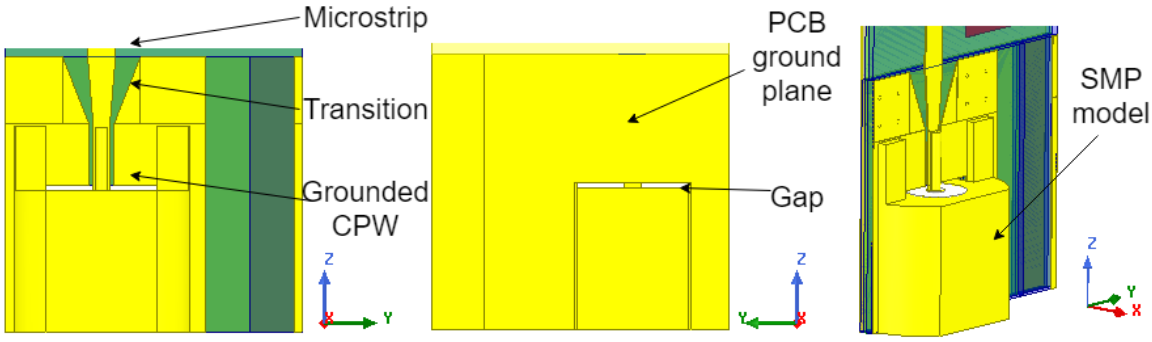

Figure 3.17: SMP interface and connector. Front view (left), back view (center), skewed view (right)

For the interface to make only a very small impact on performance, it is tuned together with the connector so that the reflection coefficient is less than -20 dB for the entire band when terminated in 50 Ω in both ends. A gap of 0.2 mm is added between the connector and the PCB in the simulation as it is expected that there might not be a perfect fit after manufacturing.

3.5 Antenna element with integrated balun

Even though the antenna element and balun are by themselves reasonably well matched to 150 Ω, when combined, differences in their impedances can cause rises in the reflection coefficient at certain frequencies. This means that the best match for each of them to a real 150 Ω not necessarily gives the best overall performance.

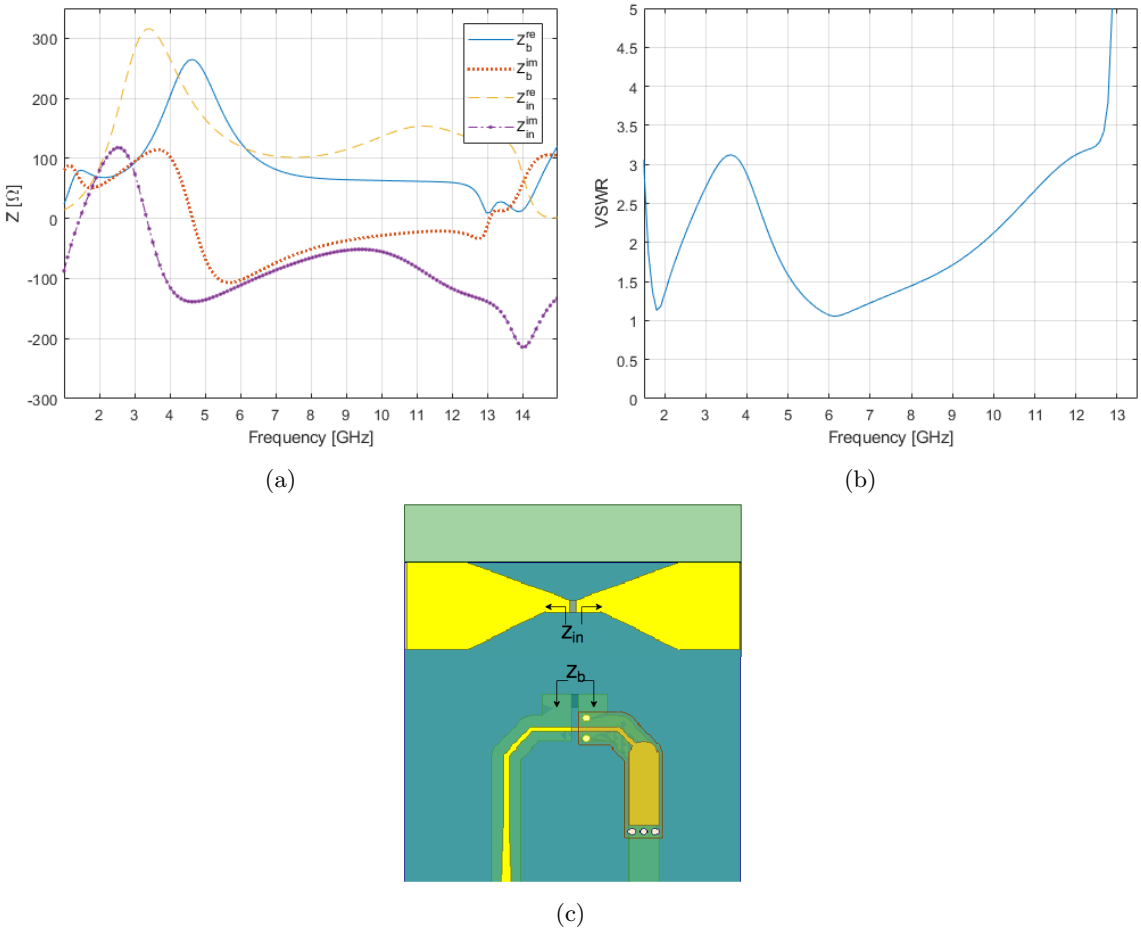

(a) (b)

(c)

Figure 3.18: Input impedances of the balun seen in Section 3.3.2 and dipole seen in Section 3.1.5 (a), and the corresponding VSWR calculated from the mismatch between the impedances (b). Z_b is the impedance looking into the balanced part of the balun, and Z_{in} is the impedance looking into the dipole (c)

Fig. 3.18 shows the imaginary and real parts of the impedances of the design examples from the previous sections. It also shows the VSWR in the balun due to the mismatch. As can be seen from Fig. 3.18a, both the impedances of both the dipole and the balun have reactive peaks in the lower frequencies. If these are matched, the reflection coefficient is reduced according to Eq. 2.11. In this way, the balun can actually be used to improve the antennas overall matching. From a circuit model perspective, the balun increases the order of the system and thereby the potential bandwidth. To account for this, the antenna element and balun are tuned manually as much as possible before integration so that $Z_b \approx Z_{in}$. The peaks in Z_b are higher in frequency than the peaks in Z_{in}. By introducing shorting pins between the ends of the dipole and ground (see Fig. 3.20b) and altering the length of the overlapping between the dipoles, the peak in Z_{in} is shifted slightly towards higher frequencies. The shorting pins are also added to prevent any resonances occurring between the unit cells by introducing a barrier between them [28]. Increasing the overall length of the balun and taper shifts the peak in Z_b towards lower frequencies. However, at this point there are too many variables to tune manually. Including the balun in the unit cell of the antenna element changes the responses of both the systems. The balun is affected by the radiation from the dipole etc. Therefore, the entire antenna element (with balun) is optimized by means of the genetic algorithm in Ansys HFSS. The connector interface is added in this optimization as it changes the overall electrical length of the system, and thereby can make a difference in the matching. In addition to this, the antenna is allowed to cut into the superstrate as seen in designs [26] and [8] to increase its effect on bandwidth. The random algorithm is set up to try different combinations of dimensions in the antenna. The variables added to the optimization include:

1. The thickness of the layers in the PCB.
2. The dielectric constant and dimensions of the superstrate.
3. The widths and lengths of the lines in the balun
4. The width of the dipole arms and the size of the overlapping patches
5. The height from the dipole to the ground plane
6. The dimensions of the shorting pins

The final result after optimization is seen in the next section.

3.6 Final antenna element dimensions and performance

This section contains the dimensions of the final antenna element design. Fig. 3.19 shows an overview of the complete design with dimensions of the superstrate, and total height. Fig. 3.20, Fig. 3.21 and table 3.1 show the dimensions of the copper layers. Fig. 3.22 shows the stackup of substrates and vias.

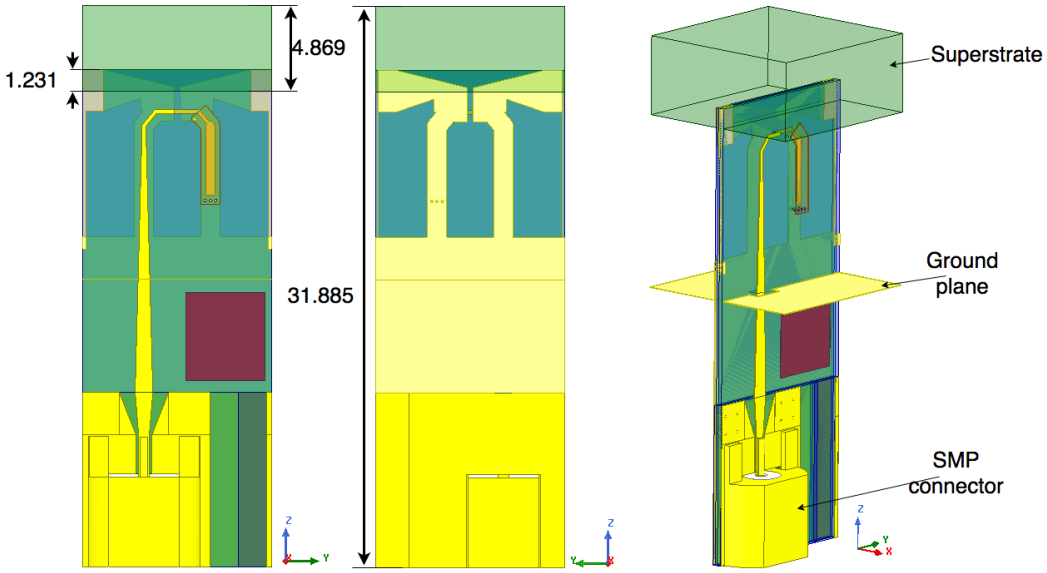

Figure 3.19: Overview of the finished antenna element design. Dimensions in mm.

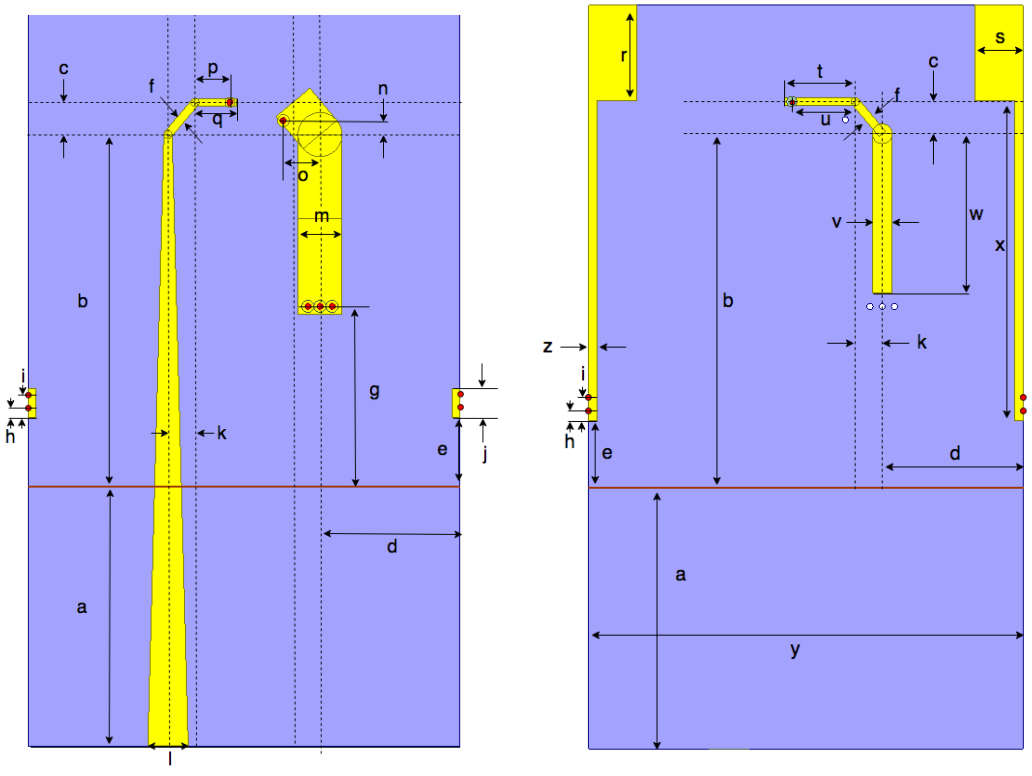

(a) (b)

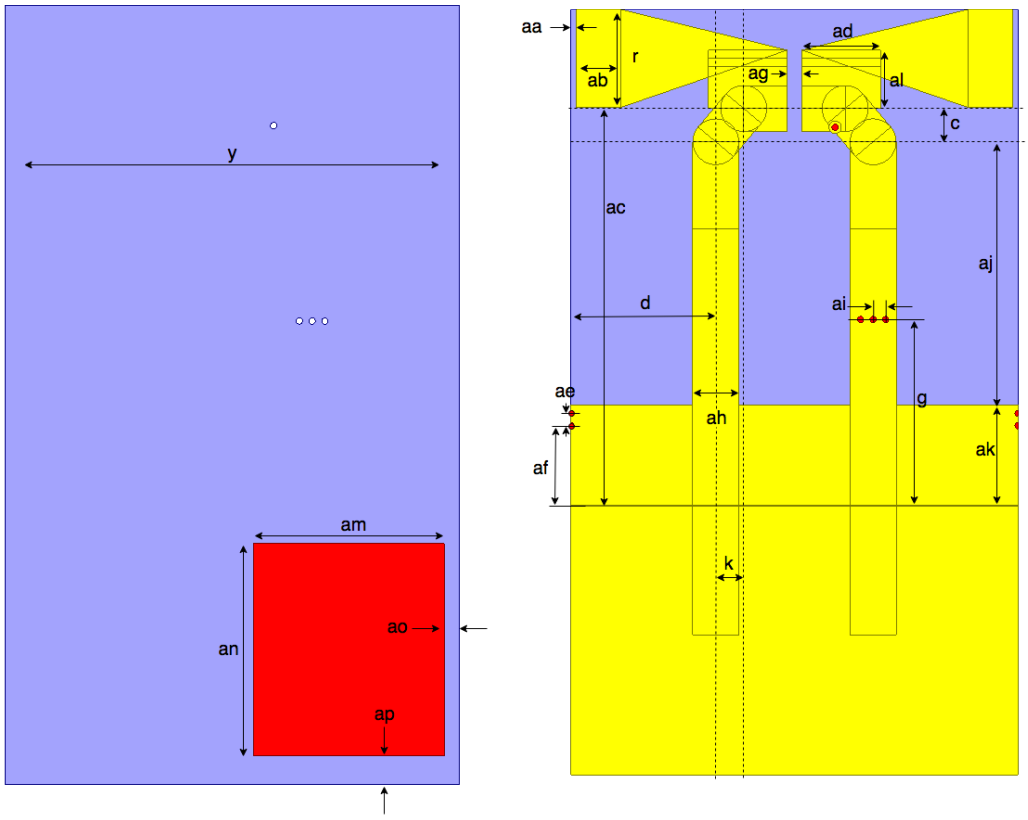

(c) (d)

Figure 3.20: Antenna element dimensions. Layer 1 (a), layer 2 (b), layer 3 (c), layer 4 (d). The horizontal line (between dimensions a and b) seen in all layers except layer 3 is the ground plane

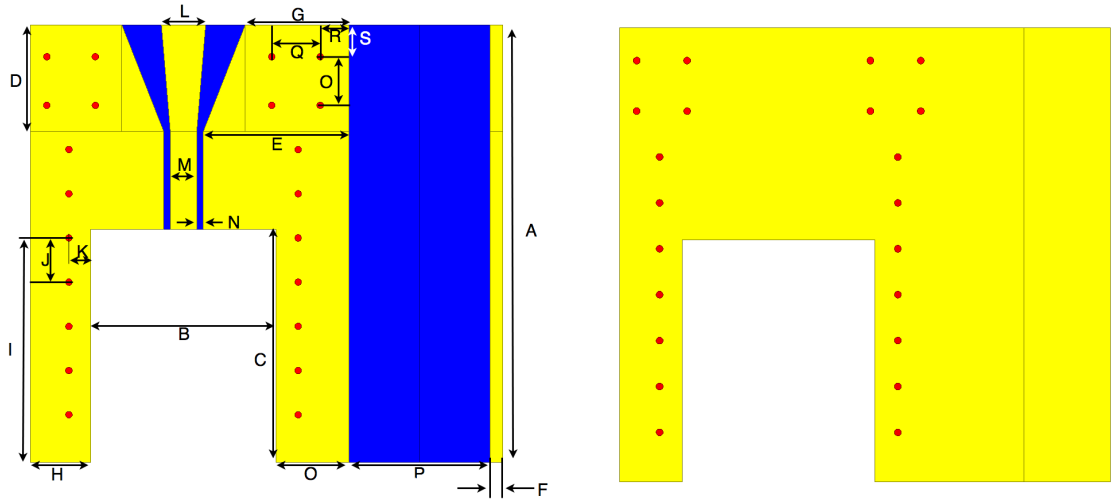

(a) (b)

Figure 3.21: Connector interface dimensions. Layer 1 (a) and layer 4 (b). Layers 3 and 2 are empty

Table 3.1: Antenna element dimensions

Parameter	value	Parameter	value	Parameter	value	Parameter	value
a	6.464	p	0.868	ae	0.300	D	2.410
b	8.707	q	1.041	af	1.902	E	3.300
c	0.797	r	2.355	ag	0.347	F	0.280
d	3.470	s	1.186	ah	1.102	G	2.350
e	1.702	t	1.734	ai	0.300	H	1.370
f	0.205	u	1.561	aj	6.305	I	5.080
g	4.448	v	0.478	ak	2.402	J	1.000
h	0.200	w	3.934	al	1.400	K	0.500
i	0.500	x	7.900	am	4.500	L	1.000
j	0.700	y	10.707	an	5.000	M	0.600
k	0.669	z	0.200	ao	0.353	N	0.150
l	1.000	aa	0.138	ap	0.669	O	1.650
m	1.090	ab	1.048	A	9.900	P	3.207
n	0.347	ac	9.528	B	4.200	Q	1.100
o	0.910	ad	1.886	C	5.280	R	1.508
						S	0.720

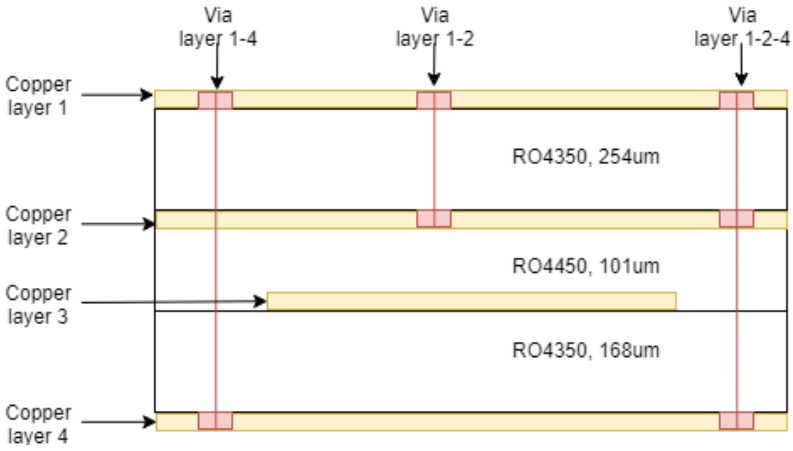

Figure 3.22: Stackup. The material type and thickness of the substrates are noted on the layers.

Layer 3 seen in Fig. 3.20c is a dummy layer added on request from the PCB manufacturer. The reason for this is to increase the adhesion between the layers and prevent delamination. As mentioned earlier, the copper layers displace the RO4450 material when the layers are glued together. The RO4350B superstrate has been replaced by a polypropylene (PP) layer with $\epsilon_r = 2.25$. The shorting pins discussed in Section 3.5 can be seen along the edges of the PCB in layer 2. For future reference, the entire layer 4 of the connector interface (Fig. 3.21b) up to where the CPS starts in layer 4 of the antenna element (Fig. 3.20d) is referred to as the PCB ground plane.

3.6.1 Simulation results for infinite array

Impedance bandwidth

After optimization, Z_{in} and Z_b were simulated separately again. This time, the connector is added as a part of the balun network. The results can be seen in Fig. 3.23.

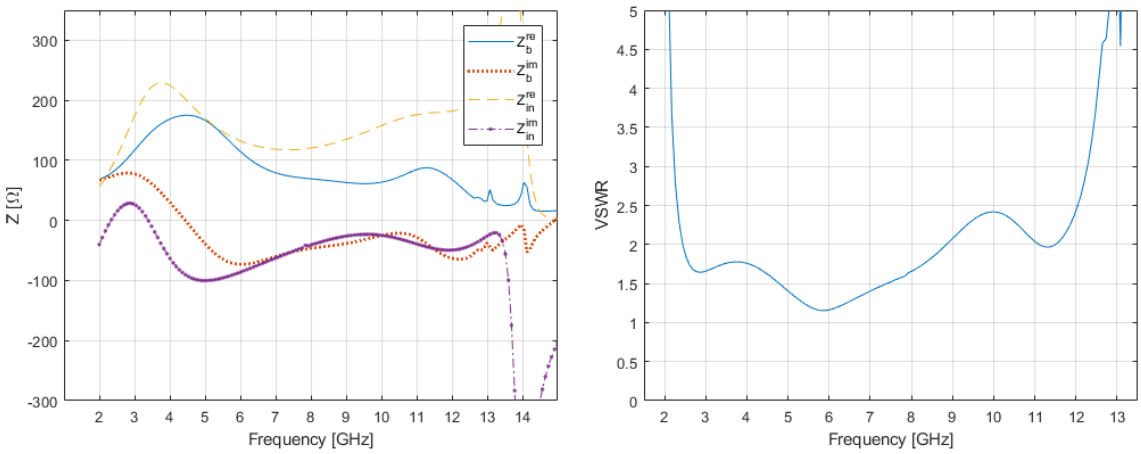

(a) (b)

Figure 3.23: Input impedances of the final design (a), and the corresponding VSWR in the balun (b). Z_b is the impedance looking into the balanced part of the balun, and Z_{in} is the impedance looking into the dipole

Now the peaks in the low end of the frequency band are lined up. Even though they are not perfectly matched, the VSWR is significantly reduced as can be seen in Fig. 3.23b. The VSWR seen from the 50 ohm SMP connector at different scan angles is plotted in Fig. 3.24.

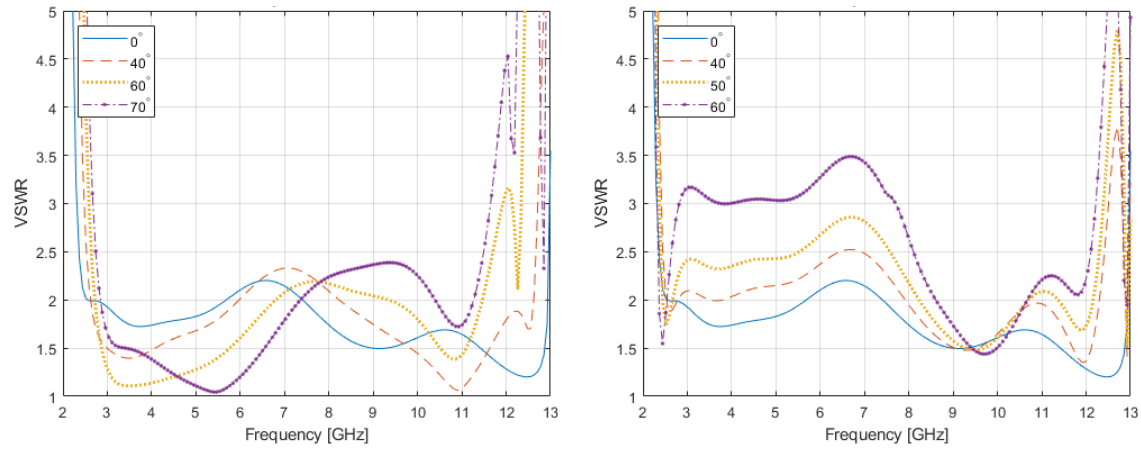

(a) (b)

Figure 3.24: VSWR for different scan angles (θ) in the E-plane (a) and the H-plane (b)

The results from Fig. 3.24 are summarized in table 3.2 and 3.3.

Table 3.2: E-plane scan bandwidth for a VSWR of < 2.5

Scan angle	Bandwidth	Bandwidth ratio
0°	2.33-12.95 GHz	1:5.56
40°	2.5-12.65 GHz	1:5.06
60°	2.6-11.7 GHz	1:4.50
70°	2.7-11.5 GHz	1:4.26

Table 3.3: H-plane scan bandwidth for a VSWR of < 2.5

Scan angle	Bandwidth	Bandwidth ratio
0°	2.33-12.95 GHz	1:5.56
40°	2.4-12.4 GHz	1:5.16
50° (VSWR<3)	2.35-12.35 GHz	1:5.25
60° (VSWR<3.5)	2.25-12.25 GHz	1:5.44

The results seen in table 3.2 and 3.3 are considered good enough for production since the minimum bandwidth required is 3-12 (1:4) GHz for a VSWR of 3 at a scan angle of 40 ° in both planes. As can be seen, the VSWR in the H-plane is generally higher, but the bandwidth for given standing wave ratios is larger.

Shorting pins effect on impedance bandwidth

The shorting pins seen in the antenna design in the previous sections (See Fig. 3.20b) were added to each antenna element before optimization to prevent common mode resonances appearing due to the coupling between the feeds of neighbouring cells [8][28][6]. They are placed on a different copper layer than the dipole, and are therefore only capacitively coupled to it. Instead of being a direct short circuit to ground.

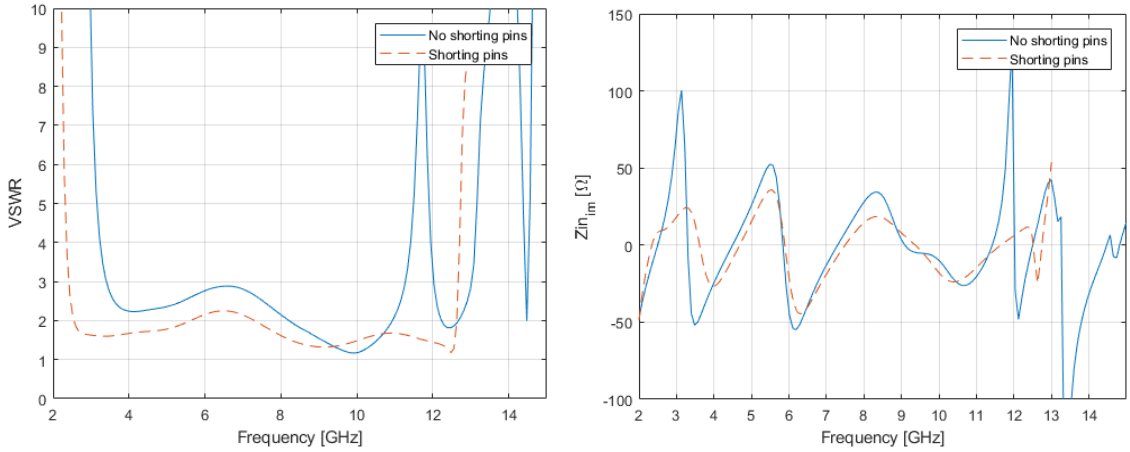

(a) (b)

Figure 3.25: VSWR (a) and imaginary part of Z_{in} (b) scanned to broadside, with and without shorting pins

Fig. 3.25a shows the VSWR with and without the shorting pins. In the plot without shorting pins, there is a clear peak in VSWR at about 12 GHz. This is pushed further up in the band when the shorting pins are added. The pins act as a part of the matching network. They significantly boost the performance in the lower end of the band. Fig. 3.25b shows that the pins dampen the peaks in the input reactance. By removing the peak in Z_{in} around 3 GHz, the lower cutoff frequency is reduced from 3.5 to 2.5 GHz.

Radiation efficiency and cross polarization

When closing in on 12 GHz, the radiated energy splits between the two main Floquet modes as seen in Fig. 3.26, since these modes are orthogonal, this translates into very poor cross polarization isolation above 12 GHz.

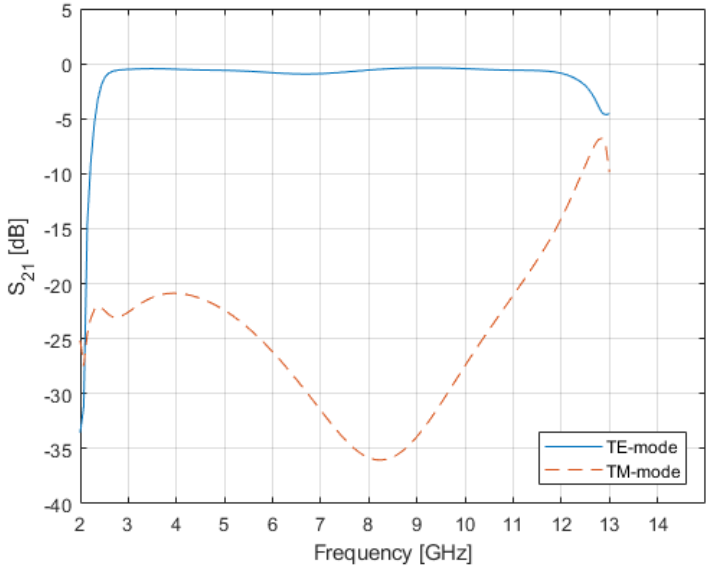

Figure 3.26: Transmission coefficients for the two main modes of the array in an infinite configuration

As can be seen from Fig. 3.26, for an H-plane simulation (where the TE-Floquet mode is the dominant mode), the TM-Floquet mode starts propagating significantly around 12 GHz. By 12.5 GHz, the ratio between the two modes is 7.5 dB. How this affects performance is dependent on the application of the antenna. If the signal is received by a dual-polarized antenna, the losses could be minimal, but it will cause a loss of power when used in a single-linear polarized configuration. If used in a radar configuration, an ambiguous polarity could cause problems in identifying target types. The requirements also specify a single-linear polarization, and normally a high cross polarization isolation is desired.

The radiation efficiency is calculated using Eq. 2.41, and is plotted in fig 3.27.

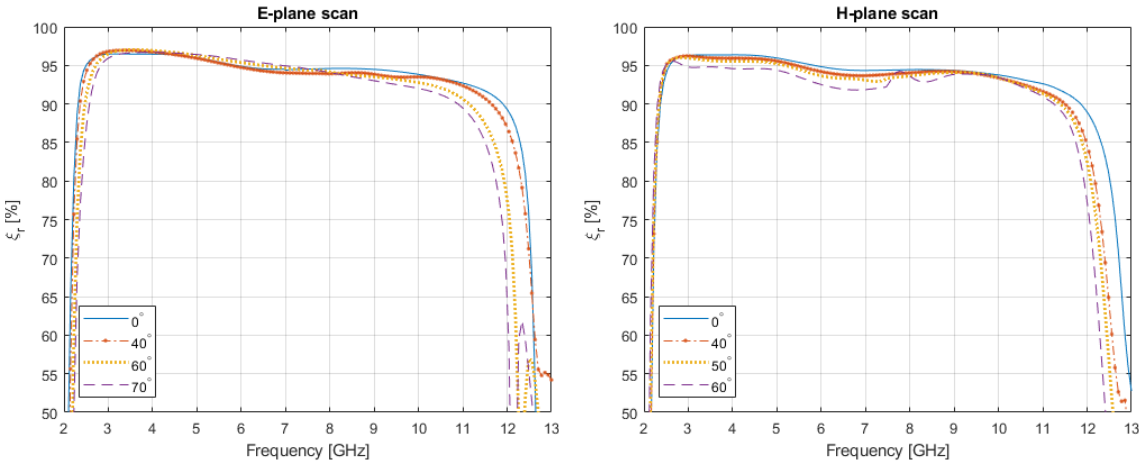

(a) (b)

Figure 3.27: Radiation efficiency for various scan angles in the E-plane (a) and H-plane (b) The small bump at 60 ° in the H-plane is believed to be a small error in the interpolating sweep used to calculate the reflection coefficient

The radiation efficiency is good for both the E and H-plane within most of the impedance bandwidth seen in Tables 3.2 and 3.3. A summary of the bandwidth for an efficiency above 80% is seen in Tables 3.4 and 3.5

Table 3.4: E-plane scan bandwidth for a radiation efficiency of >80%

Scan angle	Bandwidth
0°	2.2-12.46 GHz
40°	2.2-12.31 GHz
60°	2.2-11.9 GHz
70°	2.38-11.75 GHz

Table 3.5: H-plane scan bandwidth for a radiation efficiency of >80%

Scan angle	Bandwidth
0°	2.2-12.46 GHz
40°	2.2-12.2 GHz
50°	2.2-12.2 GHz
60°	2.18-12.05 GHz

It should be noted that the radiation efficiency stays above 90% for large parts of the bandwidth. At broadside, the bandwidth for a radiation efficiency of 90% is 2.3-11.8 GHz (1:5.13).

3.6.2 Simulation of 8x8 Array

To have a better estimate of the radiation patterns and active reflection coefficients of the antenna array before production, a simulation with a full 8x8 array as seen in Fig. 3.28 was done for frequency points 2.7, 7 and 12 GHz using the unit cell domain decomposition method. A full frequency sweep covering the bandwidth was started, but crashed when half-way done after approximately 14 days. The time consumption of a full array simulation underlines the importance of being able to use the Floquet theory based unit cell approach.

The reason for making an 8x8 array instead of a larger one is cost. The center element in an 8x8 array should give an approximate result for the elements in a larger array. The results are used as a comparison with measured values later in the report, and are not explicitly shown here.

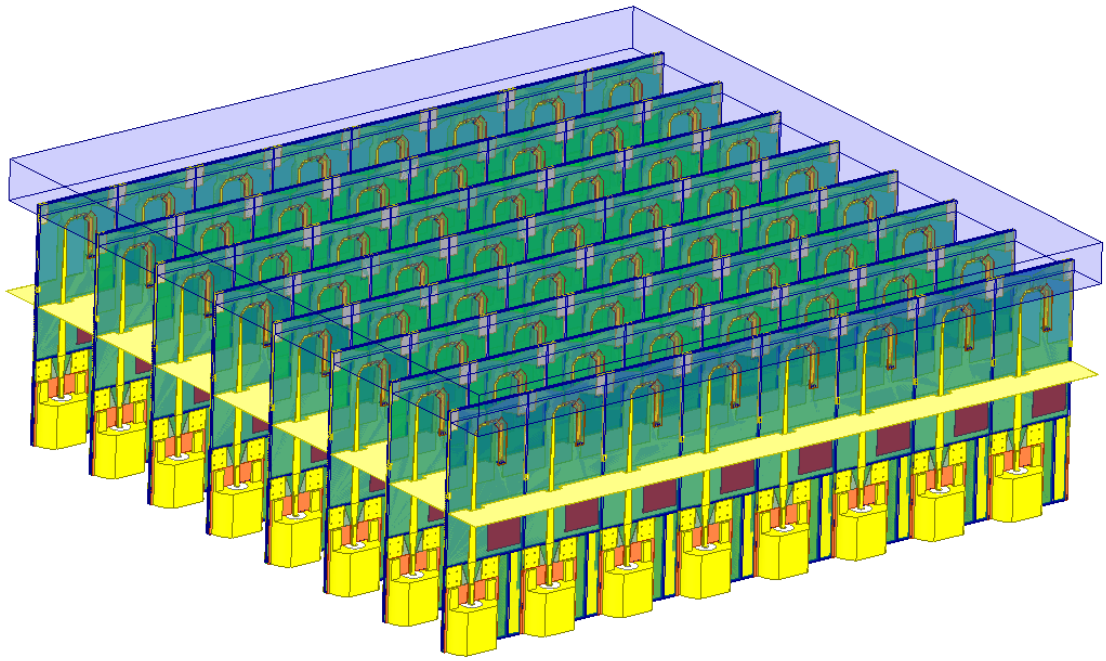

Figure 3.28: Model used in full 8x8 array simulation

3.7 Production of 8x8 array

The results seen in the previous sections are deemed good enough to warrant production of an 8x8 prototype of the antenna array. This section contains notes on the parts and assembly of the array.

3.7.1 Printed circuit boards

For the production, the PCBs layout is simply eight of the antenna elements seen in Fig. 3.20 and Fig. 3.21. At the edges, the substrate is extended 3 mm in each direction, in addition a 7 mm mounting structure is added to each edge. At the mounting structure, additional copper is added in the dummy layer (layer 3) to increase the adhesion between the layers as mentioned in Section 3.6.

The top edge of the of this structure is made so that a 1 mm ground plane resting on it will be in the right height with regards to the dipoles (dimensions b and a in Fig. 3.20). The outer dimensions of the PCB can be seen in Fig. 3.29, and the finished production is seen in Fig. 3.30.

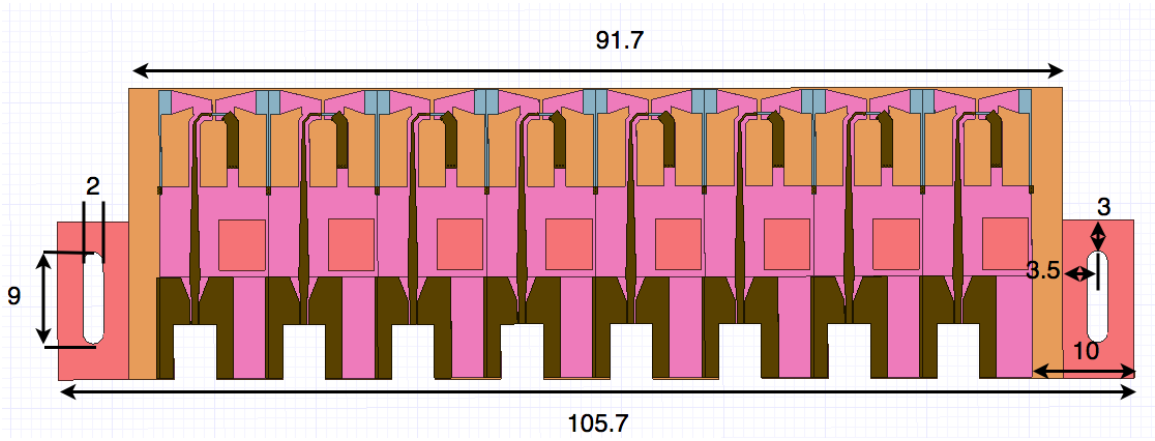

Figure 3.29: PCB dimensions in mm

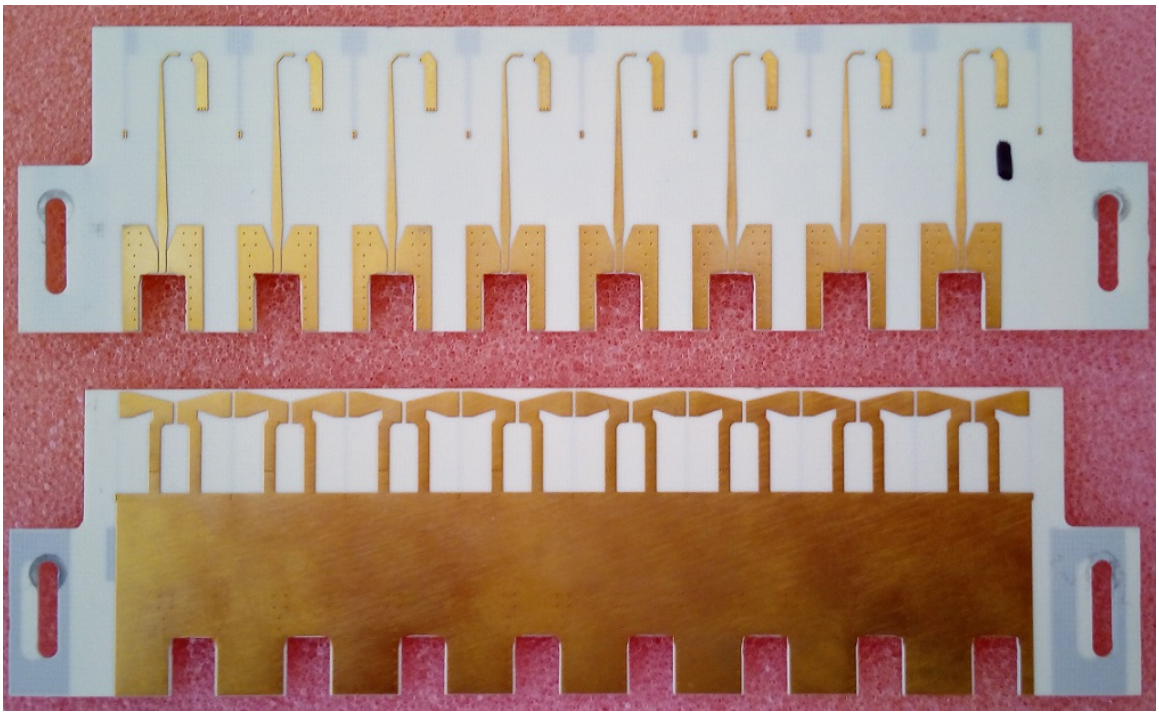

Figure 3.30: PCB finished product

Production errors

Unfortunately, the dummy layer (layer 3) added to the PCB in order for the adhesive to work has been displaced during production in most of the PCBs, meaning that the patches seen in Fig. 3.20c are displaced by a worst case distance of 1.7 mm. This distance varies from PCB to PCB. Simulations show that in an infinite array simulation, this only has a negligible effect on the performance. How it affects performance in a finite configuration is unknown. A closeup of the error is shown in Fig. 3.31

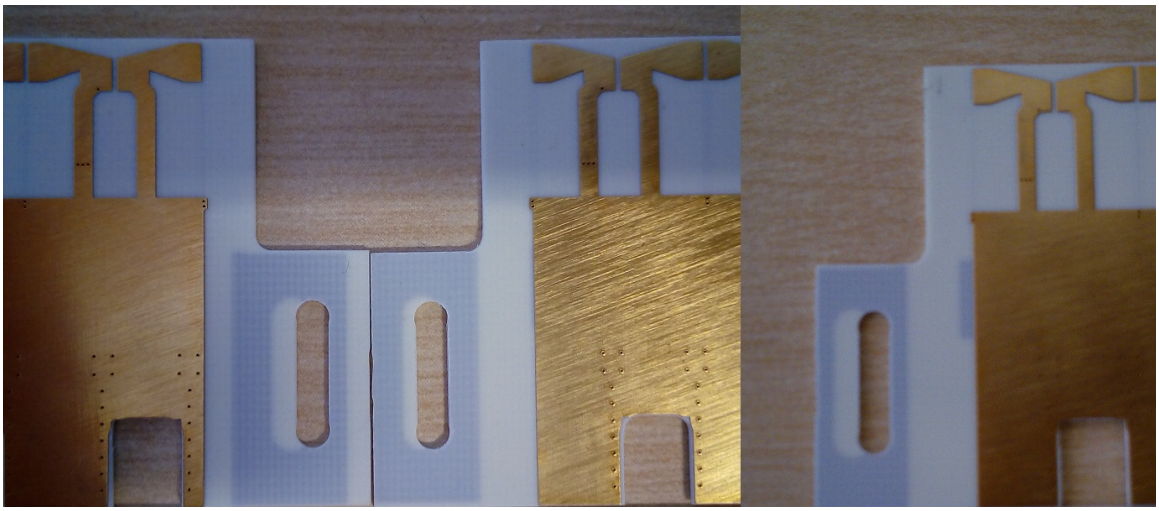

Figure 3.31: Picture of production error in layer 3 of the PCBs

From Fig. 3.31 it can be seen that the screw holes in the PCB do not line up with the cutout in the copper layer (seen as grey patches). In the rightmost part of the figure, one can also see the patch sticking out underneath the PCB ground plane. Due to time limitations, the PCB manufacturer was not asked to correct the error, and the design was built with the faulty PCBs.

3.7.2 Ground plane

The ground plane is a 1 mm thick 335x335 mm aluminium plate, a size chosen to be larger than twice the wavelength of the lowest frequency in the bandwidth. The center of the plate can be seen in fig 3.32.

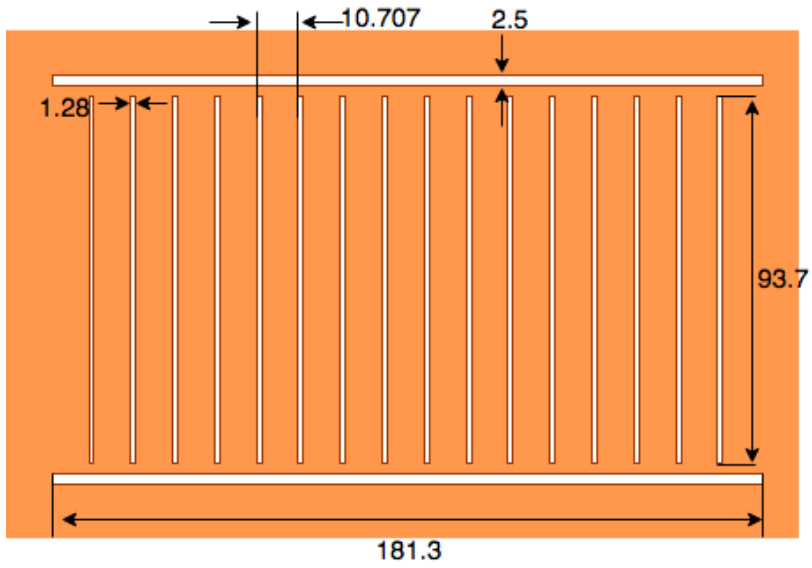

Figure 3.32: Center part of the ground plane containing the mounting slots for the PCBs. Dimensions in mm

The 93.7 mm long slots are where the PCBs are passed through, and the 181.3 mm slot is where they are fastened to the ground plane using aluminium brackets. There are 16 of the 93.7 mm slots to accommodate testing using extra PCBs in the future. Note that this differs from the simulated ground planes as the slots which the PCBs are passed through are closed at the ends, whereas in the simulations they are not.

3.7.3 Superstrate

The superstrate is made larger than the size of 64 of the unit cells seen in Fig. 3.19 to allow it to be fastened using nylon screws to the 181.3 mm track in the ground plane. To save production cost, and ease assembly, the tracks are made 1 mm wide as opposed to the size seen in Fig. 3.22. In the infinite simulation this only had a negligible effect on the performance. The dimensions of the superstrate are seen in Fig. 3.33

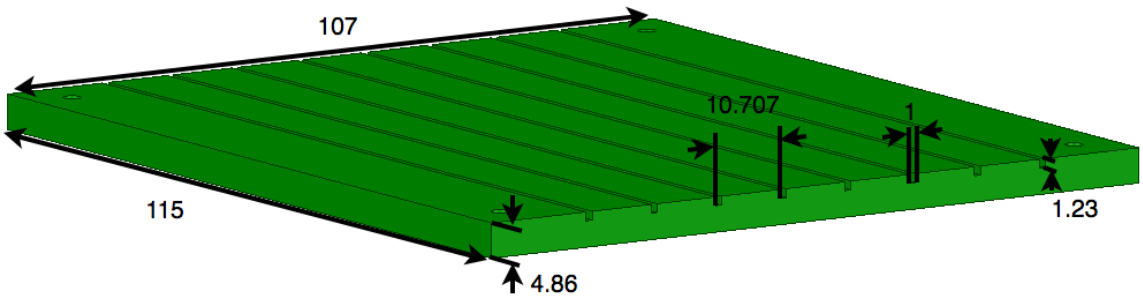

Figure 3.33: Superstrate dimensions in mm

3.7.4 Assembled array

The finished assembly without the superstrate can be seen in Fig. 3.34

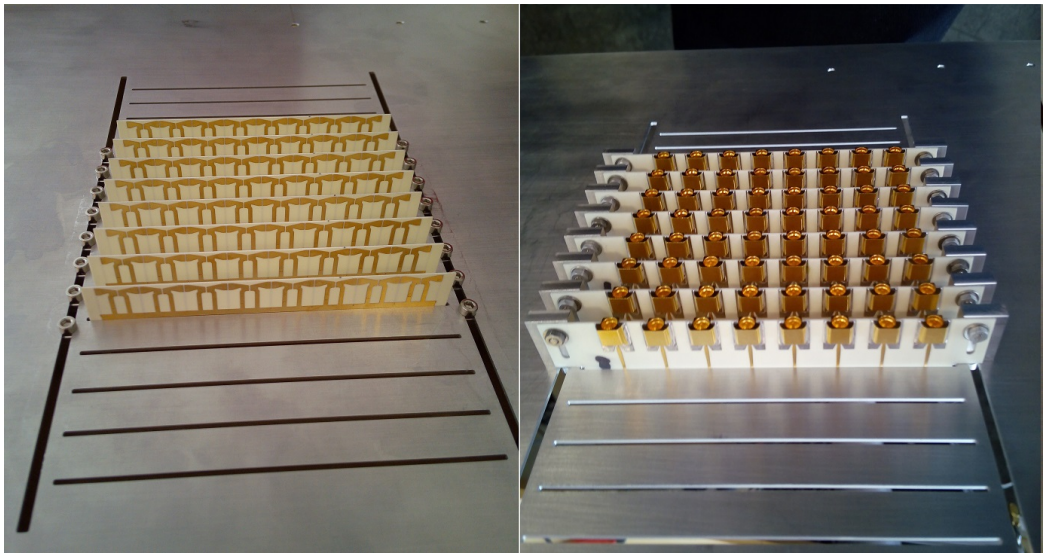

Figure 3.34: Front and back view of assembled array

The PCBs are pressed to the ground plane as tightly as possible to ensure a good connection between the ground planes on the PCB and the aluminium plate. Due to limited availability of nylon screws, the superstrate is held in place by rubber bands as seen in Fig. 3.35. The bands are placed as close to the edge of the superstrate as possible to avoid problems with increase in the dielectric constant.

Figure 3.35: Superstrate held in place by rubber bands

Chapter 4

Measurement setups

4.1 Radiation pattern and gain

The radiation pattern measurements were done at the antenna test facilities at the University of Oslo (UiO). At these facilities, the setup is very simple. It consists of an anechoic chamber, a network analyzer and a motor to rotate the antenna under test in both elevation and azimuth as seen in Fig. 4.1.

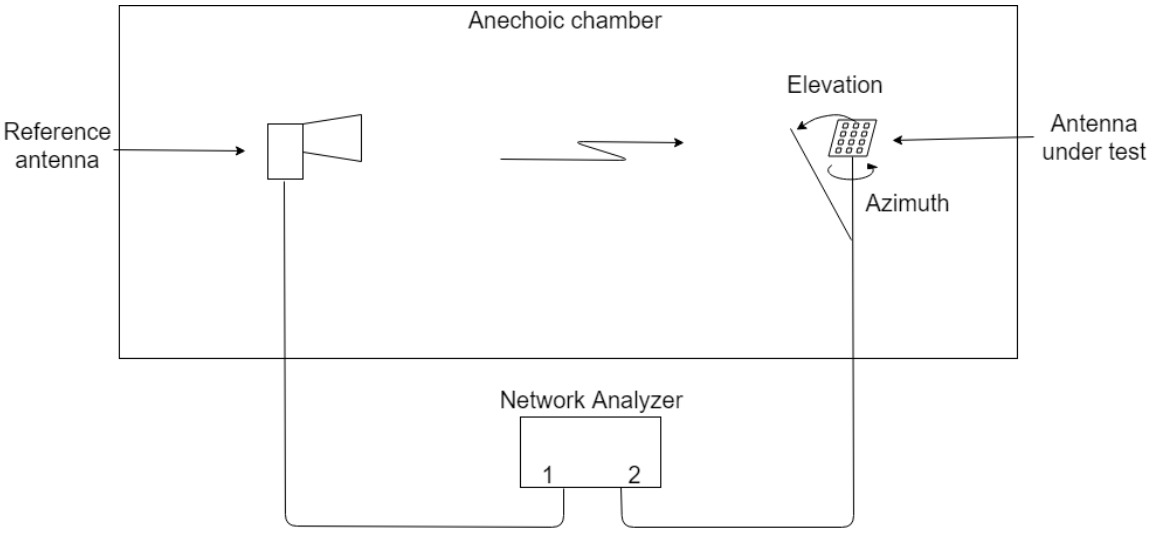

Figure 4.1: Test setup at UiO

The reference antenna is fed by a 10 dBm signal from port 1 of the network analyzer, and the power ratio between port 1 and port 2 is measured over the entire bandwidth of 1-14 GHz and for each azimuth angle (in this setup, azimuth = θ). The gain in dB of the antenna under test is calculated as

$$G_{AUT} = S_{21} + FSL - G_{ref} \tag{4.1}$$

where S_{21} is the power ratio between port 1 and 2 in dB, FSL is the free space path loss in dB [15] generated due to the distance between the two antennas and G_{ref} is the gain of the reference antenna in dB. Cable losses are removed by calibrating the network analyzer using the cables feeding the antennas. The measurements are done without using a power splitter to divide the power between antenna elements. This means the elements have to be measured one-by-one. Match-terminating all the non-excited elements while measuring one allows the pattern of the array to be computed as [21][16]

$$G_{array}(\theta,\phi) = \frac{|\sum_{n=1}^{N} A_n G_n(\theta,\phi) e^{jk_0(x_n\Psi_x + y_n\Psi_y)}|^2}{\sum_{n=1}^{N}|A_n|^2}, \tag{4.2}$$

where A_n is the normalized incident current or voltage of the antenna element and can be represented as

$$A_n = e^{j(x_n\beta_x + y_n\beta_y)} \tag{4.3}$$

G_n is the gain of the antenna element, x_n and y_n are the coordinates of the antenna element in the x-y plane and

$$\Psi_x = d_x sin(\theta)cos(\phi) \tag{4.4a}$$

$$\Psi_y = d_y sin(\theta)sin(\phi). \tag{4.4b}$$

The scan angle is controlled by β_x and β_y in the same way as in Section 2.3.

The setup inside the chamber at UiO can be seen in Fig. 4.2

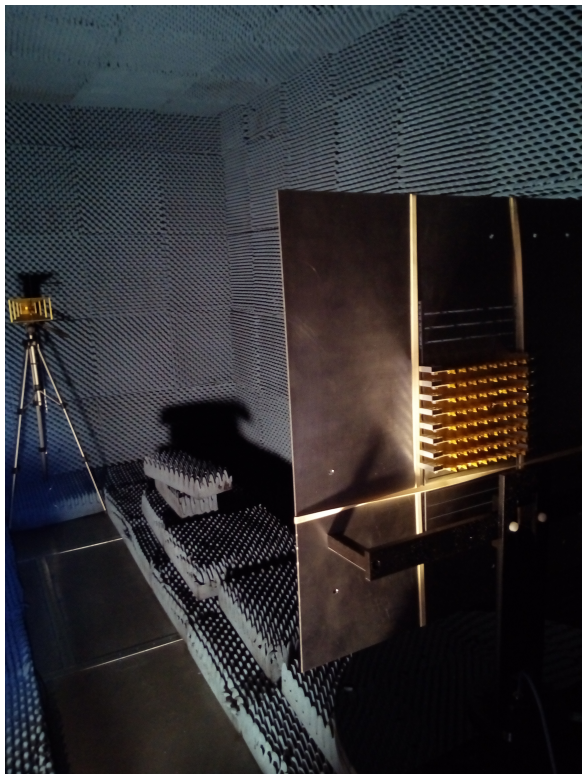

Figure 4.2: Antenna inside the chamber at UiO

Due to limited time in the test facilities, only one quarter of the array was measured. Assuming the array to be symmetrical, this quarter of the array was copied and mirrored in the calculations to simulate the full array as seen in Fig. 4.3, where the asterisk denotes a mirroring of the radiation pattern around $\theta = 0°$ as depicted in Fig. 4.4.

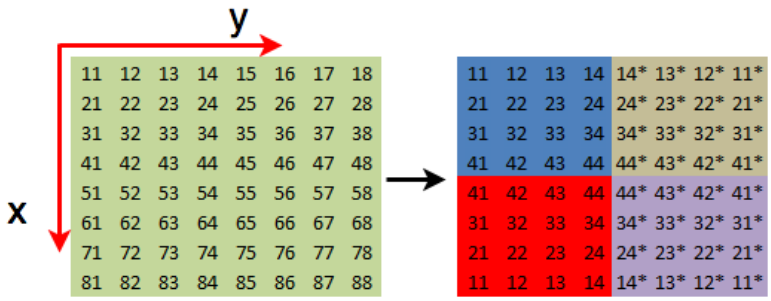

Figure 4.3: Image depicting the mirroring done during calculation of the antenna pattern

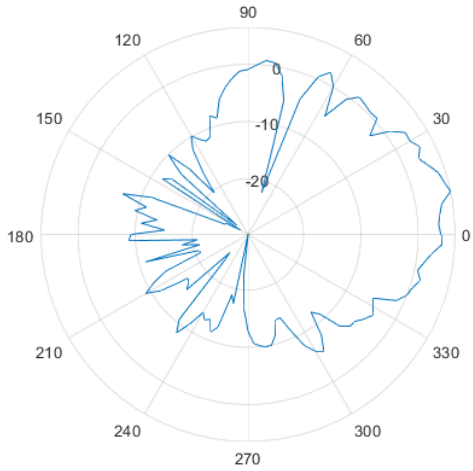

(a)

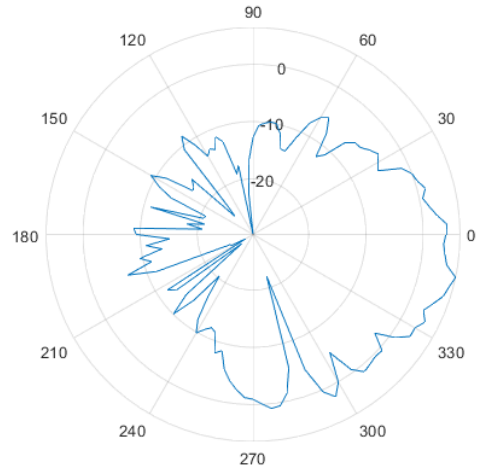

(b)

Figure 4.4: Figure illustrating the mirroring of a radiation pattern around θ=0

Measurements are limited to the E-plane only due to the limited time.

4.2 Active reflection coefficient

The active reflection coefficient is calculated according to Eq. 2.59, repeated here for convenience:

$$\Gamma_0(\theta_s, \phi_s) = \sum_n S_{on} e^{-jk_0 sin(\theta_s)(x_n cos(\phi_s) + y_n sin(\phi_s))}. \tag{4.5}$$

This means that in order to measure the whole array, the coupling between every element has to be measured which gives over 2000 separate measurements. Due to time limitations, the active reflection coefficient was only measured for one element. The element chosen is element 44 which is one of the four center elements in the array. This element is chosen as it is expected to be the one which most closely resembles an element in an infinite array.

Practically, the only equipment needed to do these measurements is a network analyzer. The measurements were done in a normal laboratory environment and not in an anechoic chamber. However, potential reflectors close to the antenna were removed, and simple tests were conducted to ensure no significant reflections were picked up from the room.

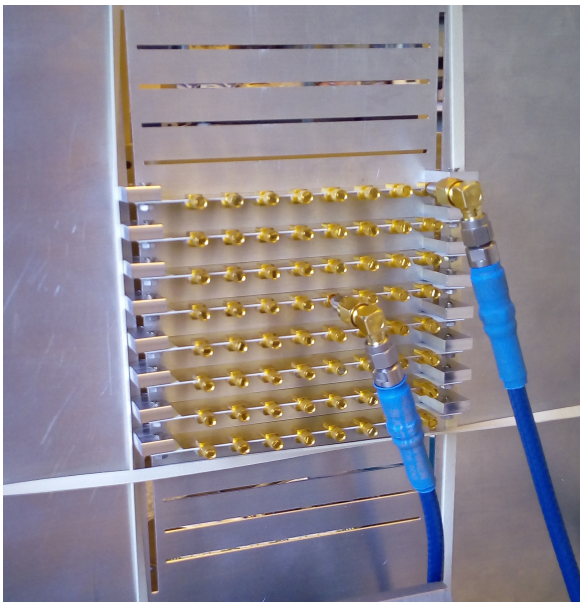

Figure 4.5: Coupling measurements

Fig. 4.5 shows the coupling between elements 11 and 44 being measured. As can be seen, all the elements not being measured are terminated in 50 Ω loads. It is important to note that this method of measuring the active reflection coefficient might not include all the phenomena that can be seen in an array where all the elements are excited at the same time. Surface waves etc. might not act in the same way when using this method. Using a 1:64 splitter and feeding all the elements at the same time would show these phenomena, but this type of equipment was not available at the time of the testing.

Chapter 5

Results and discussion

5.1 Measurements and experimentation

This section contains the measured results for the prototype. Due to delays from the PCB manufacturer's side, only a very limited time was available for assembly of the array, measurements and experimentation. As this is the first prototype manufactured, it was not expected to perform at a high level without a certain degree of experimentation and tuning. The results reflect this.

5.1.1 Active reflection coefficient

The first measurement of the active reflection coefficient was done using the method discussed in section 4.2 and with the array as seen in section 3.7.4. The results at broadside can be seen in Fig. 5.1.

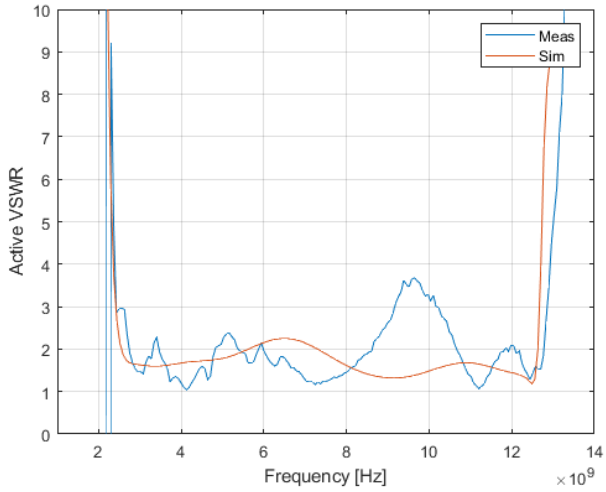

Figure 5.1: Active VSWR from first measurement together with VSWR from infinite simulation

As can be seen, the VSWR is generally very similar to that of the simulation. There is, however,

a range of peaks. The most significant at 9-10 GHz was addressed first. It was discovered that the superstrate had bent during production due to the polypropylene plate losing tension when the tracks were milled. The bend was quite significant, making the superstrate approximately 1.5 mm taller at the middle than at the edges, meaning the dipoles of the center PCBs were not covered by the superstrate. The magnitude of the bend can be seen in Fig. 5.2a. A simulation of the infinite array with the superstrate raised by 1.5 mm gives the result seen in Fig. 5.2b

(a)

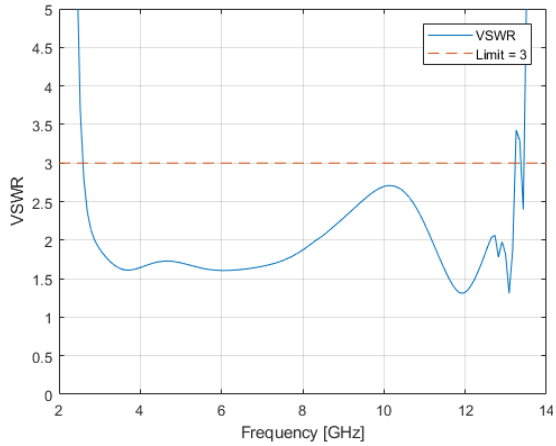

(b)

Figure 5.2: Picture of the bent superstrate (a). VSWR of antenna element in an infinite array configuration with the superstrate raised by 1.5 mm in the positive z-direction (b)

The results in Fig. 5.2b show a correlation between the superstrate's height above the dipoles and a rise in VSWR around 9-10 GHz. To straighten it out, the superstrate was heated until it was formable, then bent in the opposite direction of the existing bend while cooling down. Afterwards, it was re-heated while being pressed between two plates, and left to cool down under pressure. With the superstrate straightened out, a new test was carried out, which gave the result seen in Fig. 5.3.

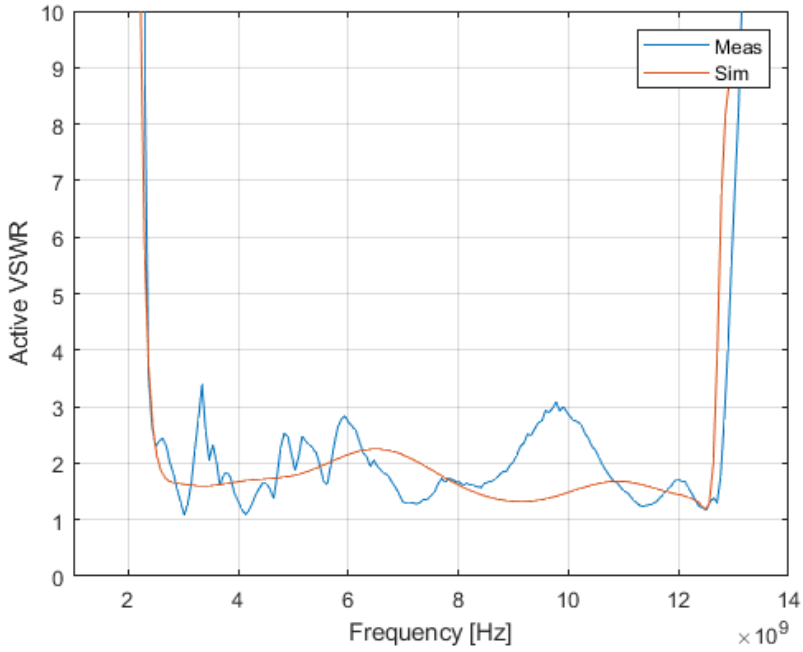

Figure 5.3: Active VSWR from second measurement with a straight superstrate. Plotted together with the result from the infinite simulation

It can be seen that fixing the superstrate has reduced the peak in VSWR at 9-10 GHz from 3.5 to 3. The passive reflection coefficient in this frequency band for the center elements was also found to be reduced compared to the previous measurement. This gives an indication that the superstrate is a part of the problem, however, according to the simulation of both an infinite array and the 8x8 array simulation from Section 3.6.2, the VSWR should be less than 2 in this area. This additional reflection could be caused by a number of things. For this prototype, unwanted resonant frequencies is a likely issue given that the structural components like screws and mounting brackets have not been simulated. The measurements show that, in this frequency band, both the imaginary part of the passive reflection coefficient of the element in question, and the imaginary part of the sum of coupling from all other elements to this element line up, making the active reflection coefficient large. In the infinite simulation, the imaginary part of the reflection coefficient does not line up with the measured coupling, which would have led to a lower active reflection coefficient. This is shown in Fig. 5.4.

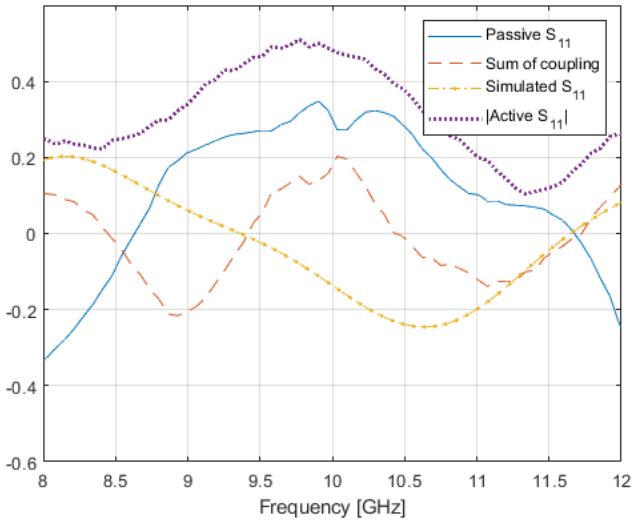

Figure 5.4: The imaginary parts of the measured passive and simulated reflection coefficient plotted against the imaginary part of the sum of all couplings to the element. The absolute value of the active reflection is added for reference

The solution to this problem would be finding a way either to reduce the imaginary parts of the passive element reflection or coupling, or shifting the peaks away from each other in frequency. In Section 3.1, small changes in the lengths of lines on the PCB would shift peaks in the input impedance. It is possible that the ground plane's height relative to the dipoles might have the same effect. In the assembly of the array, mounting the ground plane in exactly the right height proved difficult due to the aluminium plate flexing. This may be a part of the problem. Infinite array simulations with the ground plane height altered by ± 0.2 mm did not show this effect, but it is possible it may appear in a finite configuration. Interestingly, scanning to high angles in both the E-plane and H-plane seems to shift the peaks in the imaginary part of the coupling towards lower frequencies as seen in 5.5.

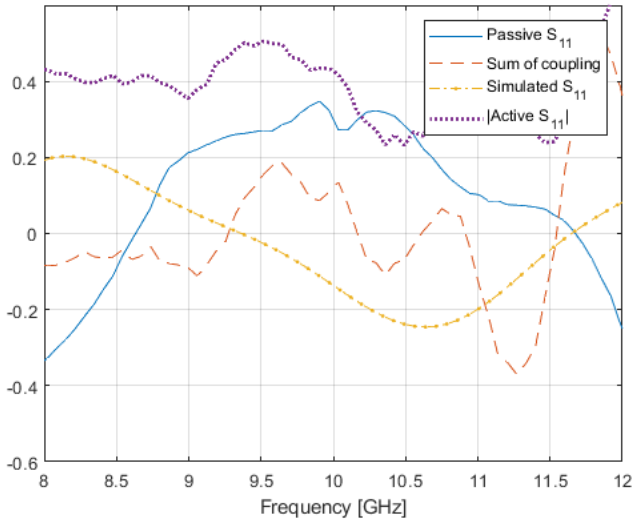

Figure 5.5: The imaginary parts of the measured passive and simulated reflection coefficient plotted against the imaginary part of the sum of all couplings to the element. The absolute value of the active reflection is added for reference. Array scanned to 60° in the H-plane

This result indicates that the peak is not very sensitive to scanning compared to other peaks within the bandwidth. This can be seen more clearly in Fig. 5.6. As time did not allow very much experimentation, other methods of reducing this peak in reflection were not attempted. This problem could be correctable through better manufacturing methods. Due to the low reaction to scanning and time limitations, efforts were spent trying to reduce the other peaks instead. The peaks seen in the lower frequencies were found to be greatly affected by scanning of the array. Especially in the H-plane as seen in Fig. 5.6, and were therefore considered next.

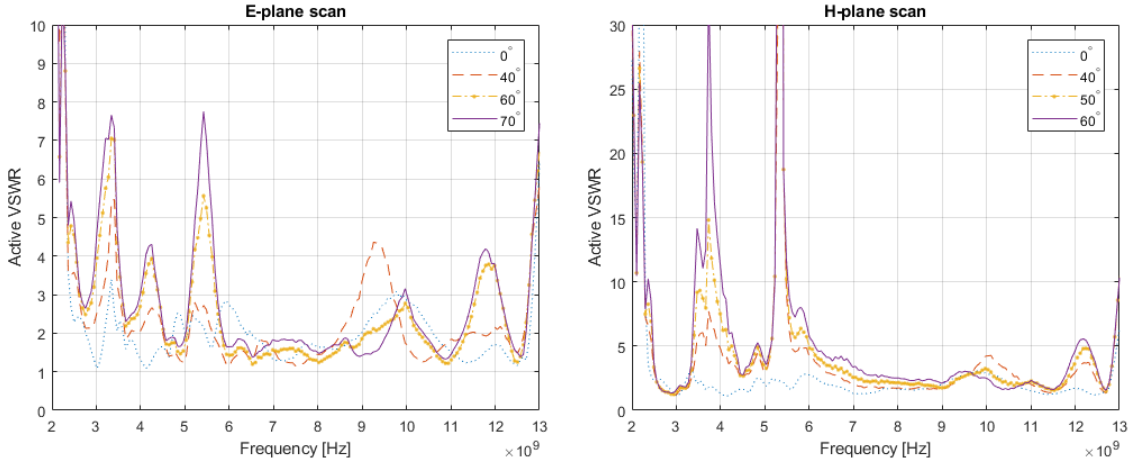

(a) (b)

Figure 5.6: Active VSWR from second measurement with the repaired superstrate for various scan angles in the E-plane (a) and the H-plane (b)

As seen, the peaks shoot up when scanning, making the reflection unacceptable. All these peaks are believed to be a symptom of the same problem, as they appear to act in the same manner when scanning. Therefore, the main focus was first put on investigating only one of the peaks, namely the peak at 3.34 GHz. From the measurements, it was found that at this frequency there was a large drop in the sum of the coupling from all other elements to the element in question (element 44) as can be seen in Fig. 5.7.

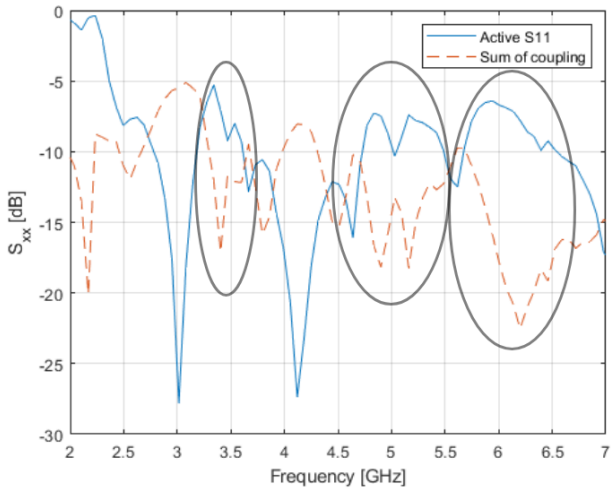

Figure 5.7: Active reflection coefficient of element 44 plotted together with the sum of the coupling to all other elements. Drops in coupling/peaks in reflection are marked with circles

The frequency 3.34 GHz has a wavelength in free space of approximately 89 mm, which coincides quite closely with many of the lengths in the structure of the array. The ground plane at the back of the PCBs is approximately 85 mm, the slots in the ground plane in which the PCBs are mounted are 93.7 mm and the slots for the screws holding the PCBs is 181.3 mm (approximately two wavelengths). One possible explanation of the drops in coupling could be that resonances within the slots lead to the waves being stopped on their way between the two elements under measurement, thereby reducing the coupling. To prevent any unnecessary resonant frequencies in the ground plane, all open slots were covered with aluminium tape. The unbraco screws used to fasten the PCBs were replaced by flat head screws and the heads taped over to prevent resonances between the screw heads, and the ground plane on the PCBs was taped to the aluminium ground plane using copper tape with a conducting adhesive. The fixes can be seen in Fig. 5.8.

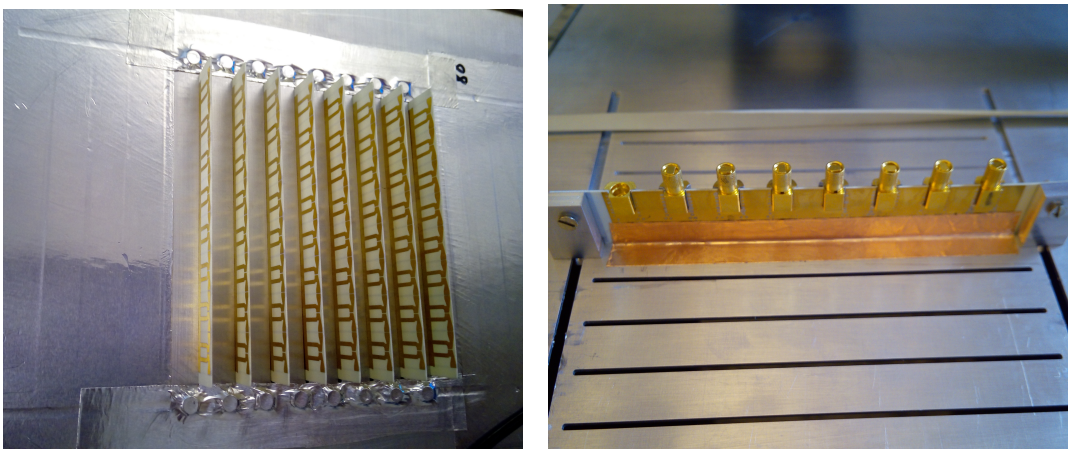

(a) (b)

Figure 5.8: Aluminium tape on the front side of the ground plane (a) and copper tape connecting the ground plane of the PCB to the aluminium ground plane (b)

The active reflection coefficient was measured again with the fixes seen in Fig. 5.8a both with and without the copper tape seen in Fig. 5.8b. The results in both cases can be seen in Fig. 5.9

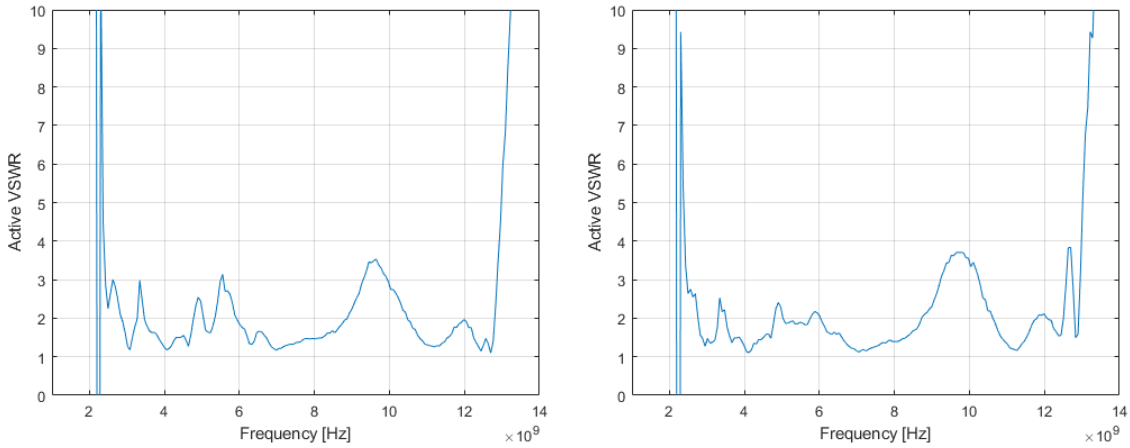

(a) (b)

Figure 5.9: Active VSWR from measurement without (a) and with (b) the copper tape seen in Fig. 5.8b

Fig. 5.9 shows that the problems can not be attributed to the slots in the ground plane directly. There is a slight reduction in VSWR at the peaks when adding the copper tape as seen in Fig. 5.8b which shows that the connection between the two ground planes is important. This is not seen in the simulations of an infinite array where separating the ground planes by 0.2 mm made only a negligible difference in the VSWR. Part of this improved result might also be attributed to the added rigidity of the array making measurements more accurate.

To further investigate the problem, measurements of the coupling was conducted using two of the PCBs removed from the array, as seen in Fig. 5.10

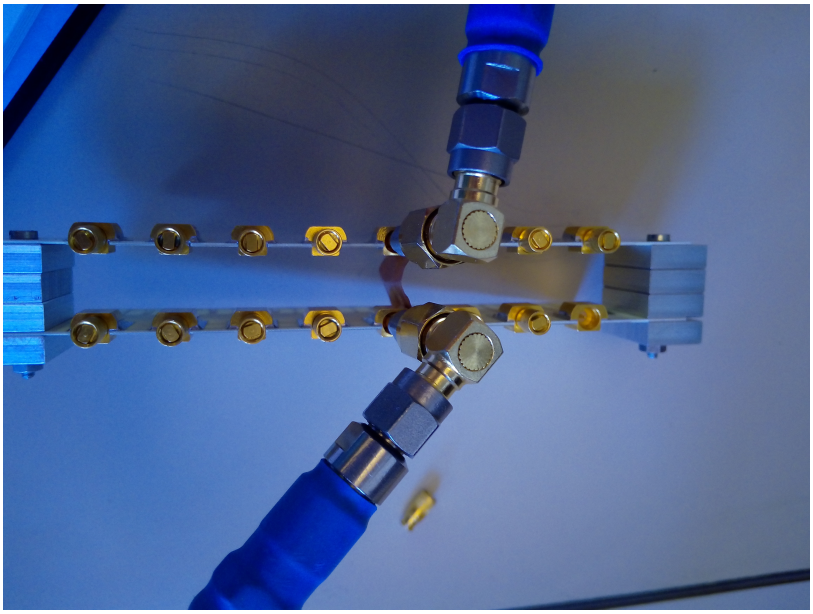

Figure 5.10: Measuring coupling on two PCBs removed from the array

The same drop in coupling as seen before was measured between element number 4 on each PCB, further supporting the conclusion above, that the ground plane alone is not to blame for the problem. Connecting the ground planes of the two PCBs using copper tape between the casing on the connectors as seen in Fig. 5.11 eliminated the drop in coupling.

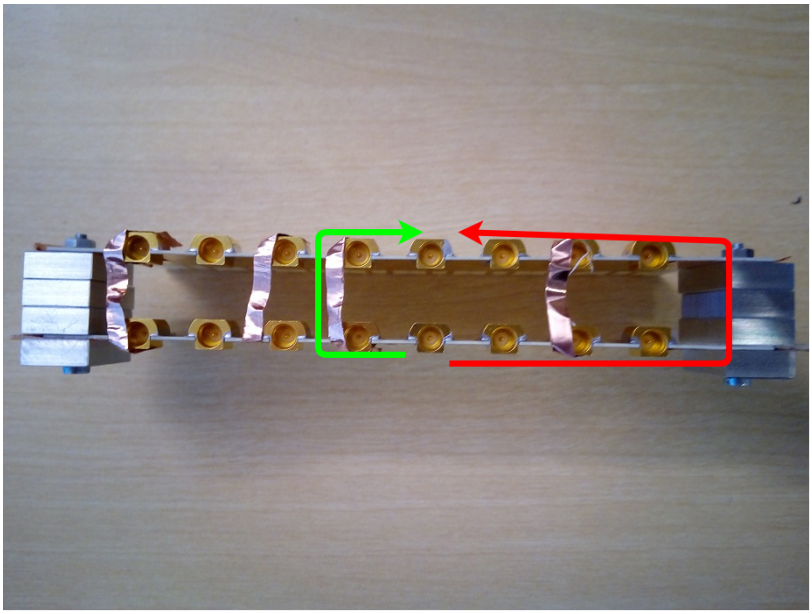

Figure 5.11: Copper tape added between connector casings

The tape possibly works as a short circuit for a ground current travelling along the ground plane of the PCB from port to port (long red arrow), allowing it to instead make a much shorter trip (short green arrow). In general the fix brings the PCB ground planes down to the same potential, eliminating ground currents. A reason why this problem does not show up in the infinite array simulation could be that the distance a wave would have to travel between the connectors on separate PCBs would be infinitely long. Since this fix worked in the two-PCB configuration, it was done with the entire array as well. This is depicted in Fig. 5.12.

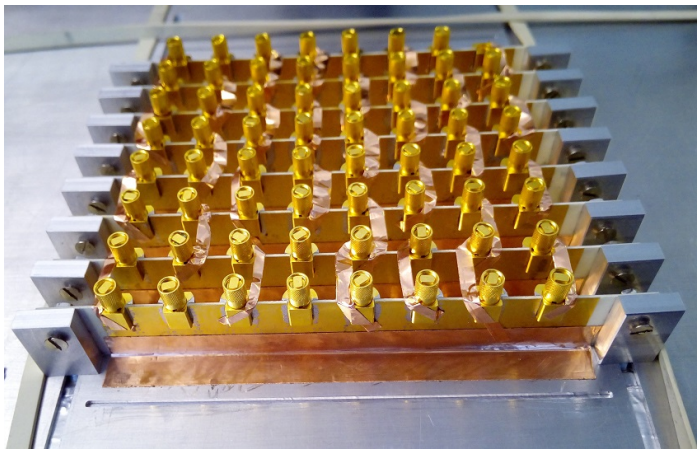

Figure 5.12: Copper tape added between connector casings

Doing this gave a significant change in the active VSWR in the lower frequencies. The result is plotted in fig 5.13 .

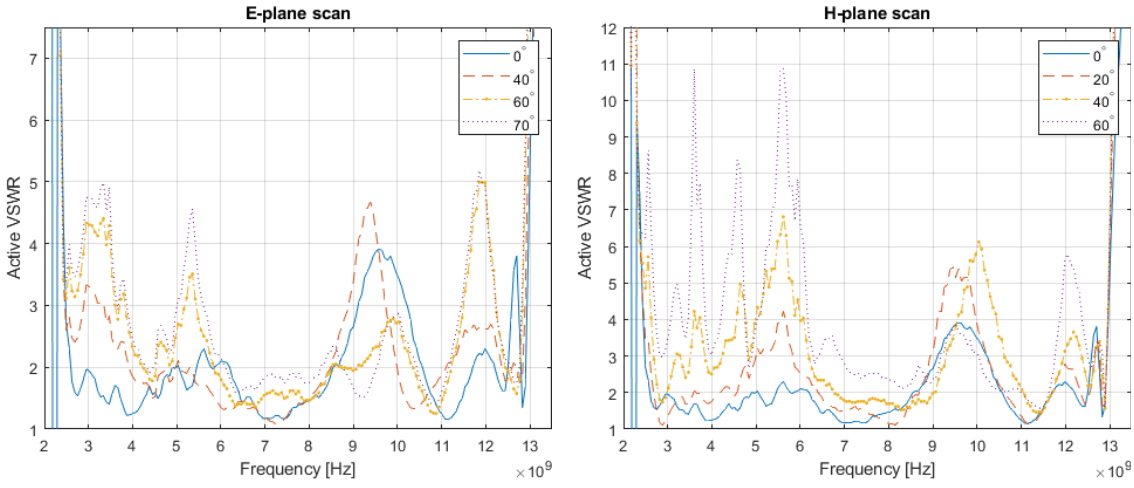

(a) (b)

Figure 5.13: Active VSWR from the final measurement with the added copper tape seen in Fig. 5.12 for various scan angles in the E-plane (a) and the H-plane (b)

As seen in Fig. 5.13, the VSWR is greatly reduced between 2.5-7 GHz compared to the result before adding the tape strips to the PBCs. At broadside, the VSWR is at worst 2.3 between 2.6 and 8.8 GHz and stays below 4 between 2.45 to 12.95 GHz (1:5.3). During scanning in the E-plane, the peaks in lower frequencies are still visible, but are significantly reduced. At 70°, the maximum VSWR is reduced from over 7.5 to approximately 5 in the lower frequencies. Unfortunately, the small peak at 12 GHz has increased, and is now problematic for scan angles above 40°. In the H-plane, scanning is very limited. The VSWR is over 5 for a scan of 20°. However, the peaks in VSWR at lower frequencies are reduced from over 30 to less than 11.

Figures 5.9 and Fig. 5.13 show that the peak around 9-10 GHz has increased between these measurements and the second measurement. A possible cause for this is that the aluminium plate of the ground plane has flexed slightly, making the height of the PCBs relative to each other different. This has led to the superstrate again being lifted from especially the 4th row of antenna elements. In addition, the superstrate itself has started bending slightly, elevating the center 0.3 mm above the edges. The problem can be seen in Fig. 5.14.

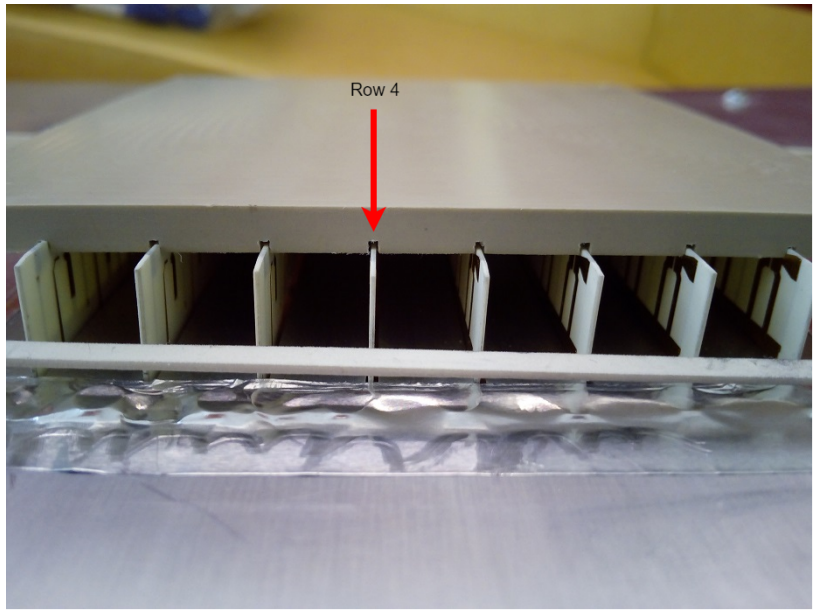

Figure 5.14: Height of superstrate above dipoles changed due to the ground plane bending

One can see that the 1st and 8th row of elements are covered as designed, while for the center rows, the superstrate is lifted clear off the dipoles. This quite closely resembles what happened when the superstrate was bent in the first measurement. Unfortunately there was no time to correct this issue and to do the test again.

In general the problems seen in the active reflection coefficient measurements seem to be correctable through better and more accurate production techniques. Seeing as the problems do not occur in the simulations, and that minor changes like adding short circuits between the ground planes of the PCBs greatly improves/alters performance. The results give a clear indication that the design is able to achieve great bandwidths if the production issues are mitigated.

5.1.2 Gain and radiation patterns

The gain was measured as described in section 4.1. Unfortunately, the 10 dBm output of the network analyzer seems to have been too low to take accurate measurements, especially at low frequencies. The elements naturally have a very low gain at these frequencies due to the small physical area of the unit cells, meaning that the signal to noise ratio received by the network analyzer from the antenna element is too low to create accurate data. Even though the gain is higher at the high frequencies, the increase in free space and cable losses is still limit the dynamics of the system, making the measurements inaccurate. The measurements can be used to show some general trends and approximate results.

Gain over frequency band

The gain in lower frequencies is expected to be low purely due to the physical area of the array. It should follow the directivity calculated from Eq. 2.38 quite closely for most of the bandwidth as the simulated radiation efficiency good. The measured gain is plotted in Fig. 5.15

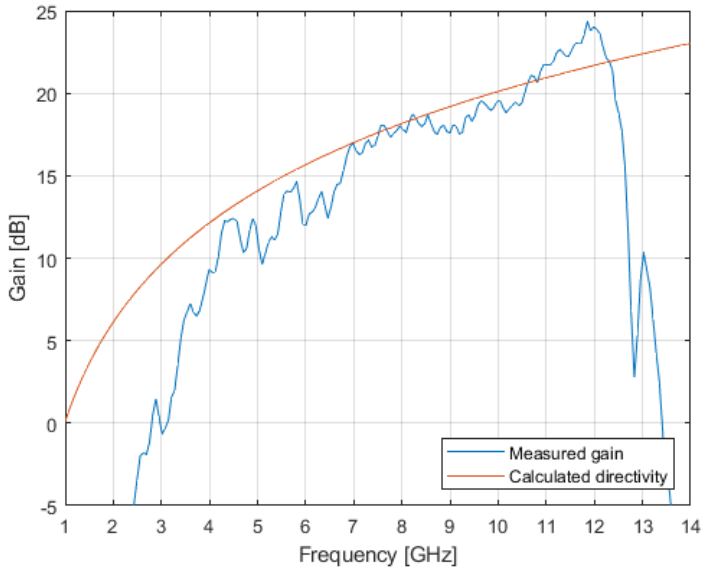

Figure 5.15: Measured co-polarized gain of the entire array at broadside versus the aperture limit, or the directivity calculated from Eq. 2.38

The measured gain is compared to the aperture limit, or the gain for an 100% efficient radiator with the same physical area as the array (also called the directivity). In general, the measured gain follows the aperture limit quite well. Low gain at lower frequencies is a general problem for small UWB arrays. However, at frequencies below 5.5 GHz, the gain of the prototype is a lot lower than expected. This is believed to be mostly due to the inaccuracy of the measurements as mentioned above. As the measured active reflection coefficient of the center element is not exceptionally high at broadside radiation in lower frequencies, there should be no large drops in gain here. However, it should be mentioned that other elements having high reflection coefficients could impact the total

realized gain. Some of this could also be attributed to the cross polarized gain being high is both ends of the frequency band which is discussed in the next section. At some points, the measured gain is higher than the calculated directivity. Again, this is probably due to the inaccuracy of the measurements. The measured gain stays above 0 dB from 3-13.42 GHz which almost covers the entire impedance bandwidth (for a VSWR < 4) seen in the previous section. Below 2.45 GHz and above 12 GHz, significant reduction in gain is seen. This is mainly caused by the high VSWR marking the ends of the bandwidth.

Cross polarization isolation

The cross polarization was only measured for one element of the array. It was measured according to Ludwig's third definition [36] which in practice means it follows the setup seen in Section 5.1.2 and the array is rotated 90° in the ϕ-direction between the co-polarized and cross-polarized measurements. A plot showing both the cross polarized gain and the co-polarized gain of this element is seen in Fig. 5.16

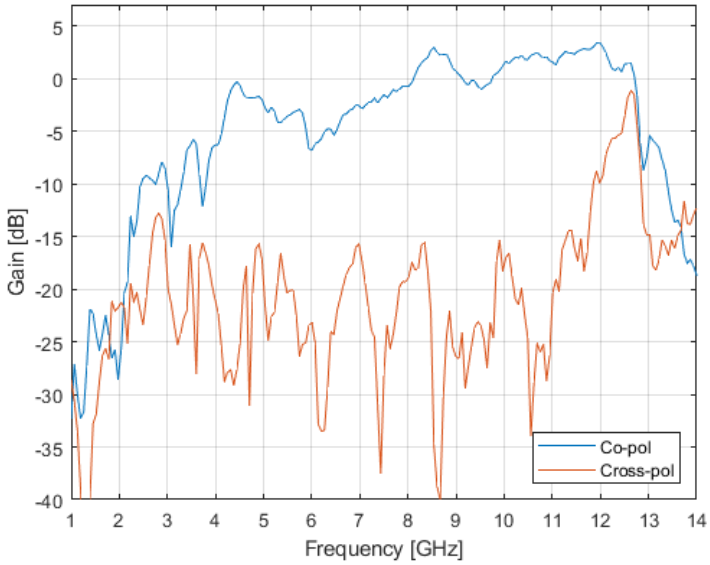

Figure 5.16: Measured co-polarized gain and cross-polarized gain of a single antenna element

Due to the ripple on the measurements it is hard to say exactly what the cross-polarization isolation is over the bandwidth. Generally, except in the low-and high end of the band, the isolation is around 10 dB. As expected from Section 3.6.1 , there is a large rise in the cross polarized gain when passing 12 GHz. A possible solution to this problem has been found: A simulation of the infinite array where the ground plane is short circuited from the front of the PCB to the back of it as seen in Fig. 5.17 shows that the cross polarization isolation in frequencies above 12 GHz can be greatly improved. This is easily done in practice by extending the ground plane to the front of the PCB using vias. This phenomenon is also discussed in [8].

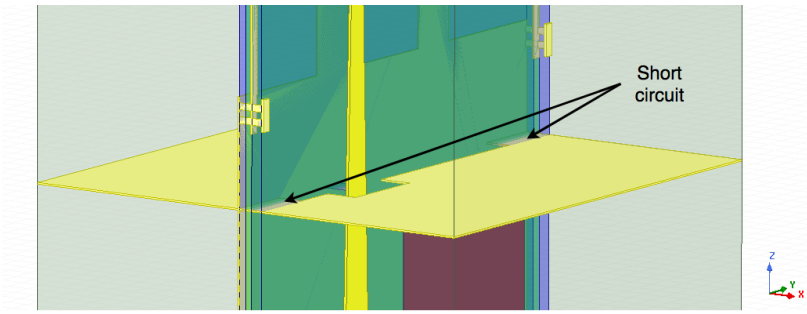

Figure 5.17: Model of infinite array used to simulate a short circuits in the ground plane

The result of the simulation can be seen in Fig. 5.18

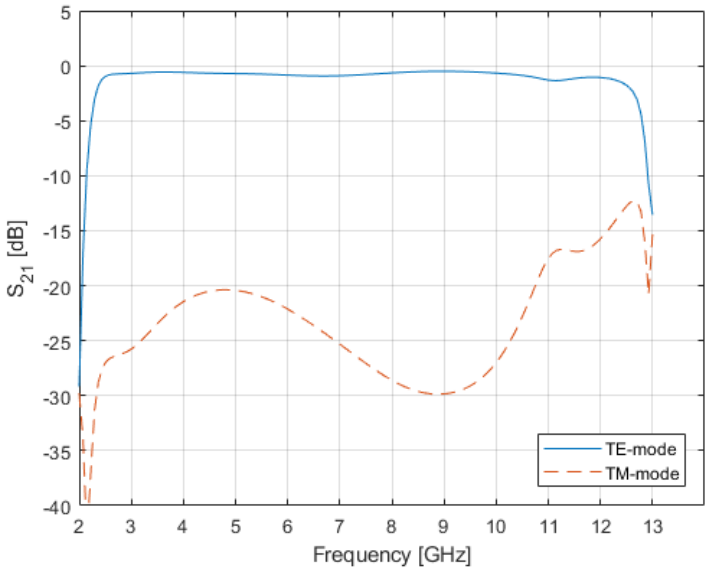

Figure 5.18: Transmission coefficients for the two main modes after short circuiting the ground plane

Instead of the TM-mode increasing towards the end of the band as seen in Fig. 3.26, it peaks at -12.3 dB at 12.63 GHz, making the ratio between the two modes 9.7 dB at worst. It is also believed that this fix would reduce some of the problems regarding the reflection coefficient discussed in Section 5.1.1 as it would do the same job as the copper tape seen in Fig. 5.12. The high cross-polarized gain in lower frequencies could possibly be a symptom of the same problem as discussed above. It does not show up in neither the infinite simulation nor the 8x8 array simulation, however it is possible that closing the ends of the slots in the ground plane causes problems here. This measurement was done before the extra slots were taped over using aluminium tape.

Radiation patterns

The measured radiation patterns for broadside radiation can be seen in fig 5.19 plotted against the simulated patterns from the 8x8 array simulation in Section 3.6.2.

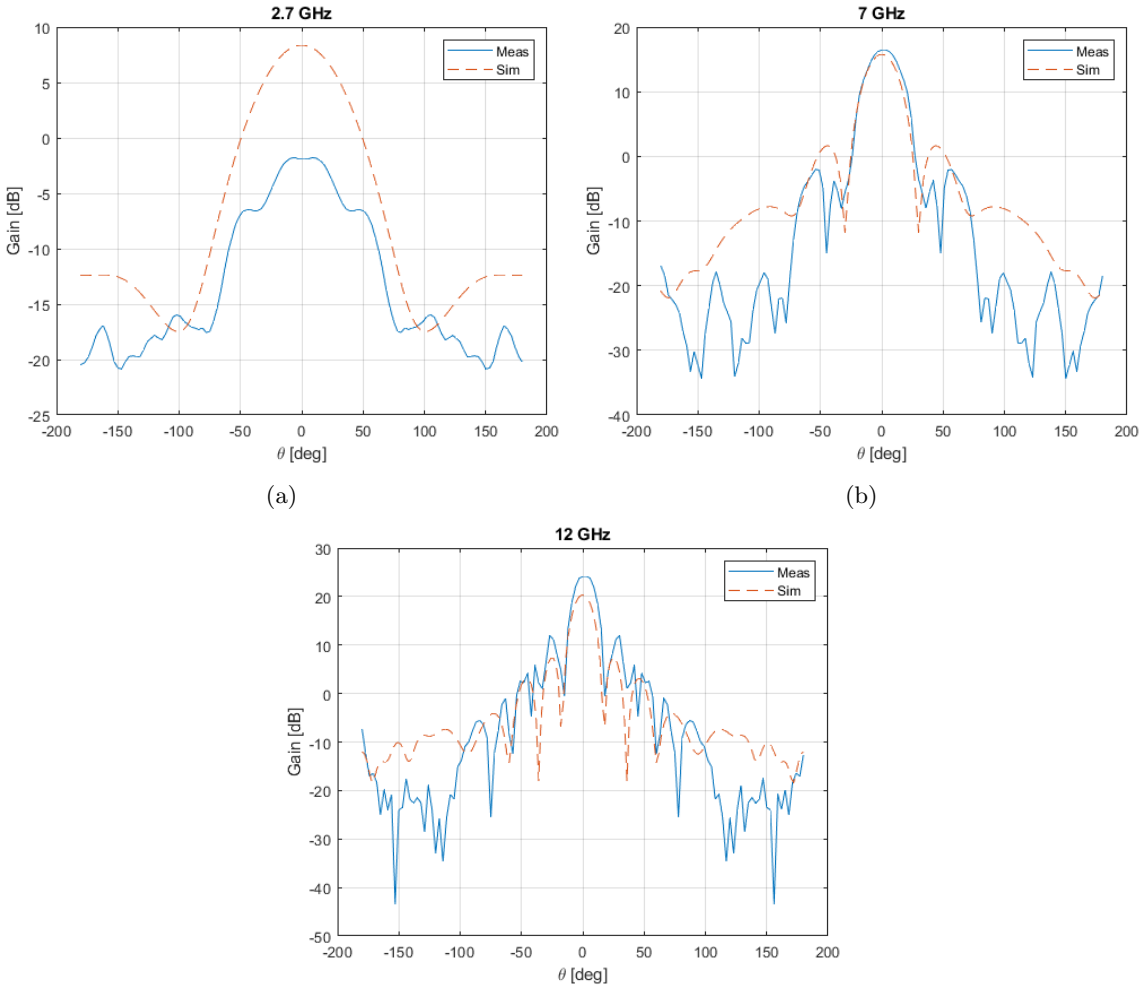

Figure 5.19: Measured E-plane radiation patterns versus simulated E-plane radiation patterns for frequencies 2.7, 7 and 12 GHz. Measured and simulated values are realized/total gain

While the simulated values lie very close (within 1.5 dB) to the calculated aperture limit from Eq. 2.38, the measured gain varies quite a bit. The values for $\theta = 0$ are summarized in table 5.1

Table 5.1: Comparison of aperture limit, simulated and measured gain

Frequency	Aperture limit	Simulated	Measured	Simulated - measured
2.7 GHz	8.7 dB	8.35 dB	-1.86 dB	10.21 dB
7 GHz	17 dB	15.8 dB	16.5 dB	-0.7 dB
12 GHZ	21.68	20.2 dB	24.16 dB	-3.96 dB

As expected, the gain is not accurately measured, however, the beamwidths and side lobe levels follow the simulated values reasonably well for 7 and 12 GHz.

When scanning the array, the shape of the main lobe is affected by the element radiation pattern as the total field is a multiplication of the element's radiation pattern and the array factor. The measured patterns for elements 14, 24, 34 and 44 can be seen in Fig. 5.20

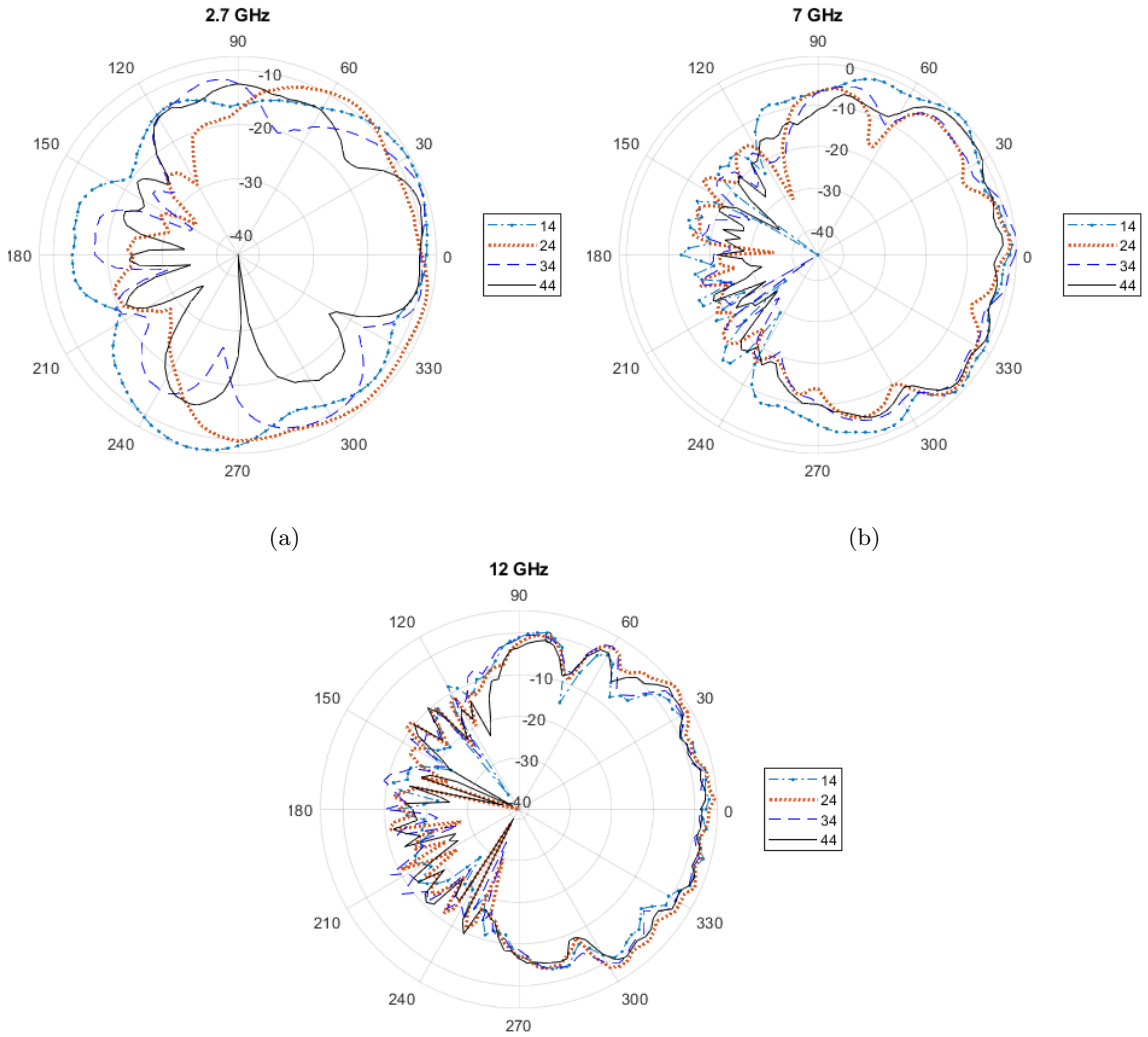

Figure 5.20: Measured radiation patterns for elements 14, 24, 34 and 44 at 2.7, 7 and 12 GHz

It can be seen that the patterns in 2.7 GHz vary greatly from element to element, meaning that it's hard to predict what the total pattern of the array will look like while scanning. For example, the pattern of element 44 has a zero at 280°. At 7 GHz, the patterns are less variant from element to element, and one can see that the array might perform worse at angles like 60° since the pattern has a dip here. At 12 GHz the array should perform reasonably well. In Fig. 5.21 the patterns for scan angles -60, -30, 0, 30 and 60° are plotted alongside the normalized array factor for the given angles.

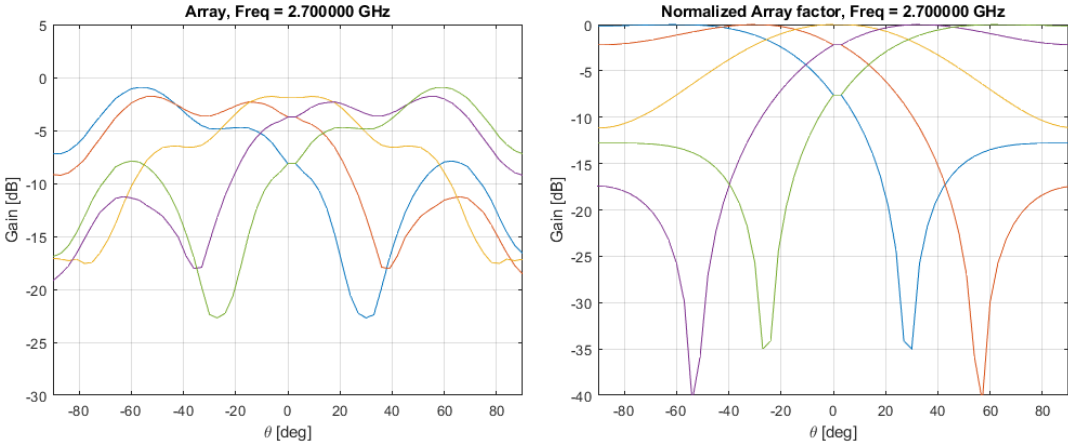

(a)

(b)

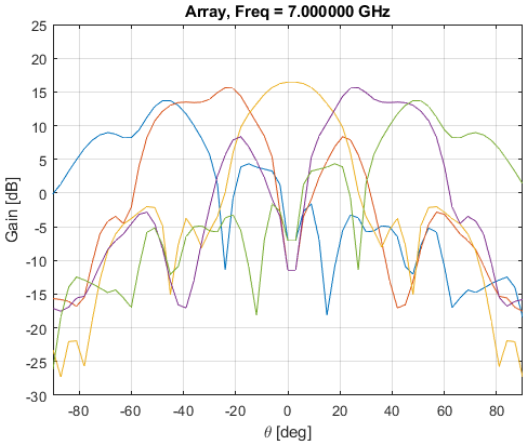

(c)

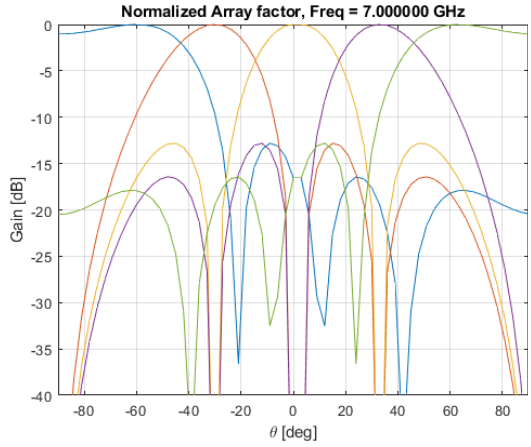

(d)

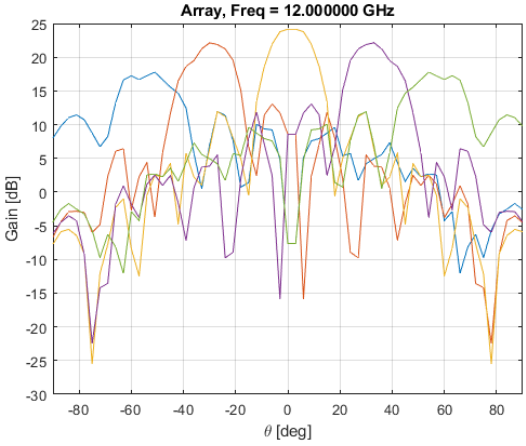

(e)

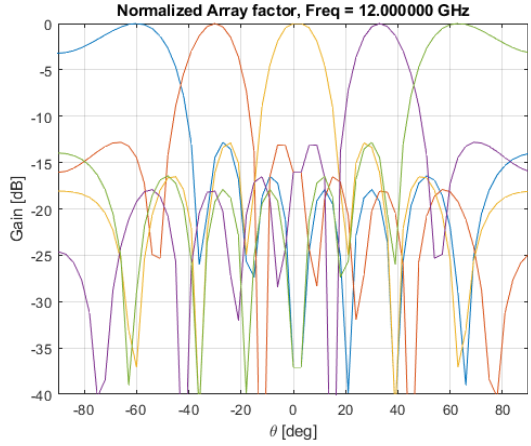

(f)

Figure 5.21: Radiation patterns in the E-plane for the array at various frequencies (a,c,e) and the corresponding Normalized array factor (b,d,f). The array factor scan angles are separated by colour: -60° (blue), -30° (orange), 0° (yellow), 30° (purple) and 60° (green)

As seen from Fig. 5.21, scanning at 2.7 GHz is futile. At 7 GHz, the lobes when scanning are, as expected, affected by the element's drops in gain at the given angles. The center of the lobes are in the right position, however, the maxima point in slightly different angles than those of the array factor. At 12 GHz, the lobes are widened by the element pattern, but less so than with the lower frequencies. It is expected that increasing the overall size of the array can make the elements more similar. In addition, this would increase the array factor, forcing the gain up in spite of dips in the element pattern.

In sum, the antenna element shows a performance significantly worse than the simulated performance and the theoretical limits at low frequencies. At frequencies above 7 GHz, the array performs as expected. It is believed that poor measurement accuracy is a major contributor to the low gain measured at lower frequencies. The array is very small, and is not expected to have significant gain here, but it should be better than what is measured. There might also be some problems regarding the cross-polarized gain at these frequencies which do not show up in the simulations. Increased gain in lower frequencies would improve the scan performance. It is possible that paying better attention to the radiation pattern when designing the antenna elements could help performance with respect to dips in the pattern.

5.2 Comparison with other designs

The problems with peaks in the VSWR in the results from the prototype make comparing it to other designs hard. It is believed that through better design and production of the structures surrounding the array (Ground plane, superstrate etc), the prototype could reach the simulated performance. Therefore, the simulated values from section 3.6.1 are used in the comparison. It should be noted that none of the reports used in the comparison contain accurately measured VSWR. The gain of similar designs normally follow the theoretical limit quite closely (within 3 dB of the theoretical limit). As the prototype is compared to the aperture limit in the previous section, and the results here are greatly affected by inaccurate measurements, the comparison between measured values and other designs is excluded from this section.

There are not a lot of array designs with integrated baluns made for frequencies above 7 GHz. The most notable design for these frequencies is the one seen in [8] which covers a slightly higher frequency band of 3.5-18.5 GHz (1:5.3) for a VSWR of < 2 at broadside. This is the design which is most similar to the design in this report as it uses a taper to feed the balun. The design uses the material Rogers RT/duroid5880 which was not available for the purposes of this project. Another design which uses a taper to feed the baluns is the design in [6]. This, however covers a much lower frequency band of 0.5-3.1 GHz (1:6.1) for a VSWR of < 3.2 and utilizes a FSS superstrate to increase scan performance. While this array achieves a very large bandwidth compared to the one in this report, it is also much larger. The unit cell is 40 mm wide, making it almost four times the size of the one in this report. This gives more space for the balun, which in turn increases the possibilities with regards to producing large ranges of impedances. The design which perhaps achieves the largest bandwidth without significant loss is the one seen in [26]. It achieves a bandwidth of 0.68-5 (1:7.35) GHz with a VSWR of < 2 at broadside. This design uses a Wilkinson power divider and split unit cell approach to feed its baluns, and the unit cell is 28x28 mm. The use of a Wilkinson power divider limits the scan capabilities of the array. This array is the only one in the comparison with a measured active reflection coefficient. It is, however measured through a 1:64 splitter, which may distort the measurements to some degree.

The designs with the most impressive bandwidths normally utilize resistive loss to achieve this. An example is the design in [5]. Which achieves a bandwidth of 0.26-3.9 GHz (1:13.5) for a VSWR of < 2.5 at broadside. This design uses a resistive FSS to kill destructive interference from the ground plane, and the baluns are fed by Wilkinson power dividers. In total, this causes significant loss, and the total efficiency drops below 60 % for a scan of 45° (both E and H-planes).

A comparison of the impedance bandwidth of the different designs can be seen in table 5.2.

Table 5.2: Impedance bandwidth, size and material comparison with other designs

Parameter	[8]	[6]	[26]	[5]	This work
Broadside					
Bandwidth ratio:	1:5.3	1:6.5	1:7.35	1:13.5	1:5.6
VSWR Condition:	< 2	< 3.2	< 2	< 2.5	< 2.5
40° E-plane					
Bandwidth ratio:	1:5.3	1:6.5	1:7.35	1:13.5	1:5.06
VSWR Condition:	< 2	< 3.2	< 2.65	< 2.5	< 2.5
40° H-plane					
Bandwidth ratio:	1:5.3	1:6.5	1:7.35	1:13.5	1:5.16
VSWR Condition:	< 2.6	< 3.2	< 2.65	< 3.1	< 2.5
60° E-plane					
Bandwidth ratio:	1:4.4	1:6.4	-	-	1:4.5
VSWR Condition:	< 2	< 3.2	-	-	< 2.5
60° H-plane					
Bandwidth ratio:	-	1:6.4	-	-	1:5.44
VSWR Condition:	-	< 3.2	-	-	< 3.5
70° E-plane					
Bandwidth ratio:	1:4.31	1:6.4	-	-	1:4.26
VSWR Condition:	< 2.2	< 3.2	-	-	< 2.5
Unit cell size:	7.5x7.5 mm	40x40 mm	28x28 mm	34x34 mm	10.7x10.7 mm
Main building material:	RT/duroid 5880	RT/duroid 5880	RO4350B	RO4003	RO4350B

Taking into consideration the physical size, radiation efficiency and available materials, the simulated antenna array element design in this report is on-par with existing designs. Compared to Novak's array in [8], the VSWR is higher at broadside and in an E-plane scan. However, the bandwidth is larger. In an H-plane scan, the array in this report performs reasonably well compared to the others, with a slightly better VSWR than [8] at 40° and a slightly worse VSWR than [6] at 60°.

Chapter 6

Conclusion

An UWB antenna element has been designed based on known methods. It has been produced and tested as part of an 8x8 array. It uses a Marchand balun to provide balanced signals to the dipoles, and a tapered line to bring the input impedance from 150 Ω at the dipole terminals down to 50 Ω at the SMP connector. In simulation, the element performs at approximately the same level as similar designs considering the materials used and size of the unit cell. It reaches a bandwidth of 5.35 for a VSWR of < 2.5 and a radiation efficiency of $> 80\%$ at broadside. When scanning in the E-plane, the bandwidth is reasonably good up to 70° with a bandwidth ratio of 1:4.26 for a VSWR of < 2.5 and a radiation efficiency of $> 80\%$. When scanning in the H-plane, the VSWR is increased in the mid band, but stays low at the start and end of the band. For a scan angle of 50°, VSWR of < 3 and a radiation efficiency of 80%, the bandwidth ratio is 1:5.25. All simulated values are well within the requirements specified by FFI. If, in the future this antenna is to be used as a radar, it is worth mentioning that the simulated radiation efficiency stays above 90% for most of the bandwidth.

The manufactured prototype unfortunately suffers from rises in the VSWR at certain frequencies, which is believed to be caused mainly by ground loops and poor manufacturing/production. Even with these peaks in VSWR, the impedance bandwidth is measured to be 1:5.3 for a VSWR of 4 at broadside or a VSWR of 2.5 if the largest peak is ignored. Indicating that the array might reach the simulated performance if the production imperfections are sorted out.

The radiation pattern and gain measurements were unfortunately very distorted due to the low transmit power delivered to the reference antenna. They are however used to observe general trends in the patterns. Perhaps the most important thing to note from this measurement is that the 8x8 array is too small to scan in lower frequencies, and that more care could be taken to ensure an even element radiation pattern during the design phase to prevent large drops in certain scan angles. Another point, seen both in the simulation and the measurements is that the cross polarization isolation is very low when nearing the end of the band. A fix for this is proposed in section 5.1.2.

In sum, the antenna element works as intended in an infinite simulation if the issues with cross polarization are fixed. The prototype, however still needs to be worked on to bring the VSWR down to the desired levels. The gain and antenna pattern measurements need to be re-done to properly verify the gain performance of the array.

6.1 Further work and recommendations

It is believed that through better construction, the performance of the prototype designed in the report can be significantly improved. The measurements show that adding copper tape between the ground planes of the PCBs has significant effect on the VSWR. Therefore, the first course of action would be to make a ground plane solution where this fix is done more rigidly. An example would be adding a second ground plane to the back of the array which is in contact with all the SMP connector casings. The next action would be implementing the fix proposed in section 5.1.2 to improve the cross polarization isolation.

Further work should include some methods not used in this design. If a very large impedance bandwidth is the most important aspect in the future, ways of implementing the resistive FSS in the very small space of the unit cells should be examined. A possible solution here is to look at implementing it on the same PCBs as the dipoles and balun. To make use of the added impedance bandwidth gained from implementing a resistive FSS, a more wideband balun also needs to be developed for the small unit cells. It is believed that the double-y balun can be worth experimenting with in this aspect. If a way is found to effectively suppress the common mode resonances in this balun, it can achieve very large bandwidths.

As accurately reproducing the purely dielectric superstrate from the simulations seemed difficult, it could be worth looking into the possibility of making this as a frequency selective surface as seen in [6]. This way, the production accuracy is brought up to the level of PCB production.

Bibliography

[1] C. Fulton, D. Thompson, J. Lake, and A. Mitchell, "Digital phased arrays: Challenges and opportunities," *Proceedings of the IEEE vol. 140*, 2016.

[2] I. I. Immoreev and D. V. Fedotov, "Ultra wideband radar systems: Advantages and disadvantages," *IEEE Conference on Ultra Wideband Systems and Technologies*, 2002.

[3] I. Tzanidis, J. P. Doane, K. Sertel, and J. L. Volakis, "Wheeler's current sheet concept and munk's wideband arrays," *Antennas and Propagation Society International Symposium. IEEE*, 2012.

[4] B. Munk, R. Taylor, T. Durharn, W. Croswell, B. Pigon, R. Boozer, S. Brown, M. Jones, J. Pryor, S. Ortiz, J. Rawnick, K. Krebs, M. Vanstrum, G. Gothard, and D. Wiebelt, "A low-profile broadband phased array antenna," in *IEEE Antennas and Propagation Society International Symposium. Digest. Held in conjunction with: USNC/CNC/URSI North American Radio Sci. Meeting (Cat. No.03CH37450)*, vol. 2, June 2003, pp. 448–451 vol.2.

[5] D. K. Papantonis and J. L. Volakis, "Dual-polarized tightly coupled array with substrate loading," *IEEE Antennas and Wireless Propagation Letters vol. 15*, 2016.

[6] E. Yetisir, N. Ghalichechian, and J. L. Volakis, "Ultrawideband array with 70° scanning using fss superstrate," *IEEE Transactions on Antennas and Propagation vol. 64*, 2016.

[7] A. Boryssenko and T. Goodwin, "Broadband antenna array aperture made of tightly couple printed dipoles," in *2016 IEEE International Symposium on Phased Array Systems and Technology (PAST)*, Oct 2016, pp. 1–6.

[8] M. H. Novak, J. L. Volakis, and F. A. Miranda, "Ultra-wideband phased array for small satellite communications," *IET Microwaves, Antennas and Propagation vol. 11*, 2017.

[9] D. K. Cheng, *Field and Wave Electromagnetics*, 2nd ed. Pearson education ltd., 2014.

[10] T. Timusk and P. L. Richards, "Near millimeter wave bandpass filters," *Optical Society of America, Applied Optics vol. 20*, 1981.

[11] D. M. Pozar, *Microwave Engineering*, 4th ed. John Wiley & Sons, 2011.

[12] A. J. Fenn and P. T. Hurst, *Ultrawideband Phased Array Antenna Technology for Sensing and Communications Systems*. MIT press, 2015.

[13] G. Ghione and C. Naldi, "Analytical formulas for coplanar lines in hybrid and monolithic mics," *Electronic Letters, vol.20*, 1984.

[14] R. N. Simons, *Coplanar Waveguide Circuits, Components, and Systems*, 1st ed. John Wiley & Sons, 2001.

[15] C. A. Balanis, *Antenna Theory, Analysis and Design*, 3rd ed. John Wiley & Sons, 2005.

[16] A. K. Bhattacharyya, *Phased Array Antennas, Floquet analysis, Synthesis, BFNs and Active Array Systems*, 1st ed. John Wiley & Sons, 2006.

[17] A. W. Oppenheim, S. R. W., and J. R. Buck, *Discrete Time Signal Processing*, 2nd ed. Prentice Hall, 1998.

[18] R. L. Haupt, *Antenna Arrays, A Computational Approach*, 1st ed. John Wiley & Sons, 2010.

[19] A. Rudge, K. Milne, A. Olver, P. Knight, R. Hansen, G. Borgiotti, D. Davies, J. Belrose, M. Radford, A. Burberry, and W. Blackband, *Handbook of Antenna Design vol. 2*, 1st ed. Peter Peregrinus Ltd., 1983.

[20] H. A. Wheeler, "Simple relations derived from a phased-array antenna made of an infinite current sheet," *IEEE Transactions on Antennas and Propagation vol. 13*, 1965.

[21] F. Gulbrandsen, A. Nysaeter, and Y. Paichard, "Design of a wide-angle scan, x-band, digital array radar antenna," in *2014 IEEE Radar Conference*, May 2014, pp. 1373–1377.

[22] D. M. Pozar and D. H. Schaubert, "Scan blindness in infinite phased arrays of printed dipoles," *IEEE Transactions on Antennas and Propagation vol. 32*, 1984.

[23] E. A. Alwan, K. Sertel, and J. L. Volakis, "A simple equivalent circuitmodel for ultrawideband coupled arrays," *IEEE Antennas and Wireless Propagation Letters, vol. 11*, 2012.

[24] J. P. Doane, K. Sertel, and J. L. Volakis, "Matching bandwidth limits for arrays backed by a conducting ground plane," *IEEE Transactions on Antennas and Propagation*, 2013.

[25] W. F. Moulder, K. Sertel, and J. L. Volakis, "Superstrate-enhanced ultrawideband tightly coupled array with resistive fss," *IEEE Transactions on Antennas and Propagation vol. 60*, 2012.

[26] J. P. Doane, K. Sertel, and J. L. Volakis, "A wideband, wide scanning tightly coupled dipole array with integrated balun (tcda-ib)," *IEEE Transactions on Antennas and Propagation, vol. 61*, 2013.

[27] B. A. Munk, *Frequency selective surfaces, Theory and design*, 1st ed. John Wiley & Sons, 2000.

[28] S. S. Holland, "Low-profile, modular, ultra-wideband phased arrays," *Open Access Dissertations, University of Massachusetts Amherst*, 2011.

[29] D. M. L. Bartholomew, "Optimum design for a broadband microstrip balun," *Electronic letters vol. 13*, 1977.

[30] J. B. Venkatesana and W. R. Scott, "Investigation of the double-y balun for feeding pulsed antennas," *Proceedings of the SPIE, Vol. 5089,*, 2003.

[31] V. Trifunovic and B. Jokanovic, "Four decade bandwidth uniplanar balun," *Electronic letters vol. 28*, 1992.

[32] B. Jokanovic, "Balance measurements in double-y baluns," *IEEE Proceedings - Microwaves Antennas and Propagation*, 2002.

[33] M. Commens and K. Zhao, "Finite antenna array analysis with a unit-cell domain decomposition method," in *2012 42nd European Microwave Conference*, Oct 2012, pp. 313–316.

[34] TEF, "PS-89675-3320 Product specification," *Molex*, 2005.

[35] J. P. Doane, K. Sertel, and J. L. Volakis, "A 6.3:1 bandwidth scanning tightly coupled dipole array with co-designed compact balun," in *Proceedings of the 2012 IEEE International Symposium on Antennas and Propagation*, July 2012, pp. 1–2.

[36] A. C. Ludwig, "The definition of cross polarization," *IEEE Transactions on Antennas and Propagation, vol. 21*, 1973.